

Marko Förstel

Investigation of non-local autoionization processes in rare gas clusters

**IPP 18/2
September, 2012**

Investigation of non-local autoionization processes in rare gas clusters

vorgelegt von
Dipl.-Phys. Marko Förstel
aus Zittau

Der Fakultät II – Mathematik und Naturwissenschaften
der Technischen Universität Berlin
zur Erlangung des akademischen Grades

Doktor der Naturwissenschaften
– Dr. rer. nat. –

genehmigte Dissertation

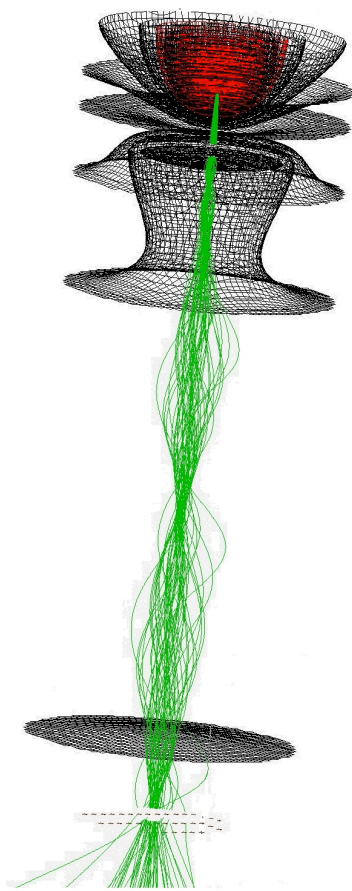
Promotionsausschuss:

Vorsitzender: Prof. Dr. Mario Dähne
1. Gutachter: Prof. Dr. Thomas Möller
2. Gutachter: PD Dr. Uwe Hergenrohn

Tag der wissenschaftlichen Aussprache: 17. August 2012

Berlin 2012

D83



Kurzfassung

Gegenstand dieser Arbeit ist die Untersuchung von nichtlokalen Autoionisationsprozessen in gemischten Edelgasclustern nach der Photoionisation mit Synchrotronstrahlung. Insbesondere ist das Ziel der Arbeit der experimentelle Nachweis von ETMD(3) (electron transfer mediated decay). Nach der Photoionisation der Cluster wurden die Flugzeiten der resultierenden Photoelektronen und der Sekundärelektronen mit Hilfe eines magnetischen Flasche Elektronenflugzeitspektrometers in Koinzidenz gemessen.

Nach der Anregung von Ar-Kr Clustern mit Synchrotronstrahlung mit einer Energie von 32 eV konnten zwei Signale im Koinzidenzspektrum identifiziert werden. Das erste Signal tritt nur in Koinzidenz mit der Ar $3s$ Clusterlinie auf und ist das gesuchte ETMD(3) Signal. Ein Spektrum der kinetischen Energieverteilung des ETMD(3) Elektrons wird gezeigt. Das zweite Signal stammt von Elektron-Elektron Stößen im Cluster.

In Ar-Xe Clustern sind sowohl ETMD(3) als auch ICD (interatomic coulombic decay) energetisch erlaubt. Mit Hilfe einer detaillierten Analyse der Valenzspektren von Ar-Xe Clustern, konnten die Struktur und die Zusammensetzung der Cluster bestimmt werden. Das Spektrum der Sekundärelektronen, die in Koinzidenz zu dem Ar $3s$ Band aufgenommen wurden, zeigt Beiträge von ICD und von ETMD. Die Intensität dieser Beiträge ist abhängig von der Zusammensetzung und Größe der untersuchten Cluster.

Weiterhin wurden Struktur und Form der Photoelektronenspektren der Außenvalenzen homogener Argon und Krypton Cluster mit unterschiedlichen Größen untersucht. Beide Spezies zeigen in einem kleinen Bereich von Anregungsenergien ein dispergierendes Feature, was dem Außenvalenzband überlagert ist. Dieses Feature tritt ab Clustergrößen von ca. 230 Atomen bei Argon und unter ca. 270 Atomen bei Krypton auf. Es wird gezeigt, dass es auf Dispersion des Valenzbandes aufgrund der Kristallstruktur der untersuchten Cluster zurückzuführen ist. Es ist somit ein Indikator für die Entstehung von Festkörpereigenschaften.

Abstract

The main topic of this thesis is the investigation of non-local autoionization processes in mixed rare gas clusters after photoionization using synchrotron radiation. In particular, the aim of the work is the experimental detection of ETMD(3) (electron transfer mediated decay). After photoionization and subsequent autoionization of the clusters, the flight times of the resulting photo-electrons and secondary electrons were measured in coincidence using a magnetic bottle electron time-of-flight spectrometer.

After excitation of Ar-Kr clusters using synchrotron radiation with an energy of 32 eV, two signals are identified in the coincidence spectrum. The first signal occurs only in coincidence with the Ar $3s$ derived cluster band and is the ETMD(3) signal. A spectrum of the kinetic energy distribution of the ETMD(3) electron is shown. The second signal comes from electron-electron collisions in the cluster.

In Ar-Xe clusters, both ETMD(3) and ICD (interatomic coulombic decay) are energetically allowed. It was possible to determine the structure and the composition of the Ar-Xe clusters through detailed analysis of their valence spectra. The spectrum of secondary electrons, recorded in coincidence with the Ar $3s$ derived cluster band, shows contributions from ICD and ETMD(3). The intensity of these contributions depends on the composition and size of the clusters under study.

Furthermore, the structure and shape of the outer valence spectra of homogeneous argon and krypton clusters of different sizes were examined. Both species show a dispersing feature in a small range of excitation energies, which is superimposed on the outer valence cluster band. This feature is observed at cluster sizes starting at about 230 atoms, in the case of argon, and about 270 atoms, in the case of krypton. This results from dispersion of the valence band due to the crystal structure of the clusters investigated. It is therefore an indicator of the development of bulk-like properties of the clusters.

Contents

1	Introduction	1
1.1	Structure of the thesis	3
2	Methods and concepts	5
2.1	Preparation and physical properties of rare gas clusters	5
2.1.1	Production of rare gas clusters	6
2.1.2	Size determination of rare gas clusters	8
2.1.3	Structure and composition of rare gas clusters	10
2.2	Photoionization	14
2.2.1	Photoionization of isolated systems	14
2.2.2	Photoionization of extended systems	17
2.2.3	Photoionization of crystalline systems	21
2.3	Autoionization	22
2.3.1	Autoionization of isolated systems	22
2.3.2	Autoionization of extended systems	24
2.3.3	ICD	24
2.3.4	ETMD	26
3	Experimental overview	31
3.1	The light source	31
3.1.1	Dipole radiation	31
3.2	Experimental setup	34
3.2.1	Experimental chamber	34
3.2.2	Vacuum generation	35
3.3	The cluster source	37
3.4	The magnetic bottle electron spectrometer	38
3.4.1	Layout	39
3.4.2	Energy resolution and transmission	40
3.4.3	Simulations	41
3.4.4	Kinematic broadening	45
3.5	Data recording and processing	46
3.5.1	Data recording	46

3.5.2	Signal processing	47
4	Near-threshold outer-valence spectra of argon and krypton	53
4.1	Electronic band dispersion in argon clusters.	54
4.2	Electronic band dispersion in krypton clusters.	60
4.3	Discussion and conclusions	64
5	Electron transfer mediated decay in mixed Ar-Kr clusters	67
5.1	Outer valence spectra of mixed Ar-Kr clusters	67
5.2	Inner valence spectra of mixed Ar-Kr clusters	70
5.3	Electron-electron coincidence spectra of Ar-Kr clusters	73
5.4	Conclusions	81
6	ICD and ETMD in mixed Ar-Xe clusters	83
6.1	Outer valence spectra of mixed Ar-Xe clusters	84
6.2	Inner valence spectra of mixed Ar-Xe clusters	86
6.3	Electron-electron coincidence spectra of Ar-Xe clusters	89
6.4	Conclusions	94
7	Summary and Outlook	95
	Bibliography	99
	Acknowledgments	115

1 Introduction

Over 2300 years ago, Aristotle had already found that the whole is greater than the sum of its parts [1]. New properties emerge in systems due to interactions between its components. A number of people becomes a complex society and a number of water molecules becomes a liquid. It is precisely these transitions, from the part to the sum, which are examined in cluster physics. A single gold atom has no golden color, has no temperature and cannot conduct electricity. The properties of the bulk emerge only as more constituents are added.

The study of the formation of these solid-state properties is an important issue in cluster physics. How large must a cluster be in order to exhibit bulk properties? How do these properties evolve with increasing cluster size? Also of great interest is determining the clusters' intrinsic properties and how these properties can be used.

This work deals with a new class of decay channels of electronically excited rare gas clusters, decay channels which are only accessible because the chemical environment in a cluster is different from that of an isolated atom, and are dependent on the clusters' composition and structure. These decay mechanisms became known as Interatomic Coulombic Decay (ICD) and Electron Transfer Mediated Decay (ETMD) [2, 3]. Assuming, for example, an inner valence vacancy in a given system with an energy above the double ionization threshold of the system. This vacancy might then decay such that the system is doubly ionized in the final state. The final vacancies are found on different sites of the system which repel each other. In small systems, this may lead to a Coulombic explosion of the system.

So far, much theoretical and experimental work has been done on ICD [4, 5], and references therein. It is known to be a general decay process, occurring in van-der-Waals bound systems, such as neon clusters, and hydrogen bridge bound systems, such as water clusters. ICD has similarities to the Auger decay. Both processes are autoionization processes. However, in an Auger decay, inner shell vacancies participate and the chemical environment is not as influential as in ICD and ETMD [2, 6]. Also, for ICD to occur, it is crucial that at least two atoms (or molecules) participate in the decay. This is not the case for Auger decay [2]. Even though research on ICD is fairly new, implications and applications are already apparent: two examples are the use of ICD to elucidate the structure of mixed clusters [7] and its possible relevances in the research on radiation damage [8].

ETMD, on the other hand, has not received as much attention as ICD. The reason is that ICD is very effective and fast, compared to ETMD. If both processes are energetically possible, ICD is several orders of magnitude more likely than ETMD [3]. This means that even though ETMD may be just as common a decay process as ICD, in many systems, its influences on the decay of a vacancy are negligible.

However, what happens if ETMD is energetically possible and ICD is not? In systems in which this is the case, ETMD(3) is a very interesting decay to study because it requires the participation of three atoms. It is therefore called *ETMD(3)*. For ETMD(2) and ETMD(3) to occur, there are strict requirements for the positions of the decay partners relative to each other. An investigation of ETMD may lead to insights into the structure of the whole system which shows ETMD. Until now, ETMD(3) had only been predicted theoretically [3, 9]. The main focus of this thesis is the experimental identification of this decay process.

In this work, I will introduce two systems which have been predicted to decay via ETMD(3) after inner valence ionization [6, 10]. These two systems are mixed clusters of argon and krypton and mixed clusters of argon and xenon. It was predicted that Kr-Ar-Kr trimers, after Ar $3s$ ionization, can only decay via ETMD(3), because ICD is not energetically possible. I will use mixed, Ar-Kr clusters produced via supersonic co-expansion to demonstrate this effect and discuss how the clusters' structure and composition influences the ETMD spectra.

Another system in which ETMD was predicted to occur are Ar-Xe clusters. Here, however, ICD between atoms which are not nearest neighbors may also be energetically possible. The decay width of ICD strongly decreases with increasing distances between the decay partners. ETMD is only possible between nearest neighbors. A system of co-expanded Ar-Xe clusters, which have been shown to exhibit a sharp segregation of the argon and xenon atoms, is therefore a very interesting object of study.

Understanding the outer valence spectra of the homogeneous species can provide a useful tool for interpreting the spectra of the mixed species. Valence band widths and binding energies allow conclusions to be drawn about the cluster size. Comparisons of the spectra from the mixed and homogeneous clusters can be very helpful, especially because there are no scaling laws for determining the size of the mixed clusters. In addition, the outer valence spectra of argon and krypton clusters exhibit a very interesting feature of their own. In a narrow range of excitation energies close to the threshold, they show a feature of strongly enhanced intensity. The binding energy of this feature shows a dependence on the excitation energy. I will discuss this feature in terms of dispersion of the valence band in a crystalline system. As such, it is a clear indication of bulk-like properties of clusters and so, although it is not directly related to my main topic of autoionization, it is worthwhile discussing it in an own chapter. To determine the sizes of the clusters at which bulk-like behavior begins, I will present

excitation energy dependent outer valence spectra of homogeneous clusters of different sizes.

In the interest of thematic focus and brevity, this dissertation presents only selected results of my doctoral research. Other work included the design, assembly and characterization of a new water cluster source (partly documented in reference [11]). Electron TOF spectroscopy with an optical laser on a fast ion beam with a magnetic bottle (partly documented in references [12, 13]). Electron TOF spectroscopy on a fast ion beam using a free electron laser (FLASH) including planning and assembly of a new SUHV-chamber and ion beam line [14]). Electron-ion coincidence spectroscopy of water clusters [15] as well as several contributions to experiments and beamtimes of colleagues: [8, 12, 13, 16–21].

1.1 Structure of the thesis

This work is structured as follows. Chapter 2 will discuss the methods and concepts relevant to the understanding of this thesis. It is divided into two parts. The first part addresses the production, structure, composition and investigation of homogeneous and inhomogeneous rare gas clusters. Particular emphasis is given to co-expanded, mixed Ar-Kr and Ar-Xe clusters. The second part of the chapter gives a short introduction to photoionization and autoionization processes. ICD, ETMD and the co-occurrence of ICD and ETMD are discussed.

Chapter 3 gives an overview of the experimental details. Here, the goal is to cover all relevant and unique aspects of the experiments in sufficient detail for the experiment to be repeated easily.

In chapters 4 to 6, the experimental results are presented and discussed. First, the valence spectra of homogeneous argon and krypton clusters are presented in chapter 4. The excitation energy dependence of the outer valence spectra of clusters of different sizes is analyzed. Chapter 5 discusses ETMD(3) of Ar-Kr in more detail. Outer and inner valence spectra of the mixed and homogeneous species are discussed in order to draw conclusions about the structure and composition of the mixed clusters. Electron-electron coincidence spectroscopy is used to identify the signal from ETMD(3) electrons. An ETMD(3) spectrum is presented. Chapter 6 discusses the co-occurrence of ICD and ETMD(3) in mixed Ar-Xe clusters in more detail. Again, outer and inner valence spectra will be used to discuss the structure and composition of the mixed clusters. A systematic variation of cluster size and composition will be used to identify both the ICD and the ETMD(3) contributions to the kinetic energy spectrum of the secondary electrons.

Finally, in chapter 7, I will give a short summary and outlook.

2 Methods and concepts

In this chapter I will introduce the main concepts and theoretical aspects necessary for discussion of the experimental results.

The first section deals with rare gas clusters. Aspects of the production of homogeneous and heterogeneous clusters using supersonic expansion are discussed. I will also discuss aspects of the cluster size determination, cluster composition and cluster structure. Because it is relevant for the discussion of ICD and ETMD, I will discuss the structure and composition of mixed, co-expanded Ar-Xe and Ar-Kr clusters in particular.

In the second section I will discuss basic concepts of some photoionization processes. This section is divided into three main parts. The first one deals with the direct photoionization process of isolated atomic systems. The second one with the photoionization of clusters. Here, initial and final state effects which influence the photoelectron spectra are discussed. The third part deals with the photoionization of crystals. Here, the influence of the crystal lattice on the photoelectron spectrum is discussed.

The third section of this chapter describes autoionization processes. A brief description of the Auger-decay in isolated systems is given. Extended systems, like rare gas clusters, exhibit additional autoionization channels. The main interest of this thesis lies in the investigation of one such autoionization channel, termed electron transfer mediated decay (ETMD). Usually, if ICD is possible, ETMD is not a relevant decay channel. I will discuss under which circumstances ETMD can become the dominant decay channel.

2.1 Preparation and physical properties of rare gas clusters

The systems in which the non-local autoionization processes described in this thesis occur are free, heterogeneous and neutral rare gas clusters. Therefore it is worthwhile to elaborate on the production, composition and structure of rare gas clusters. A cluster is an aggregation of 2 – 50000 atoms or molecules [22]. With a high ratio of surface to bulk constituents (compare figure 2.1), clusters represent a transitional state between the isolated atomic or molecular species and the solid or liquid state of matter. The clusters' constituents can be almost any type of atom or molecule. Metal clusters are held together by delocalized electrons and have mean binding energies per atom in the

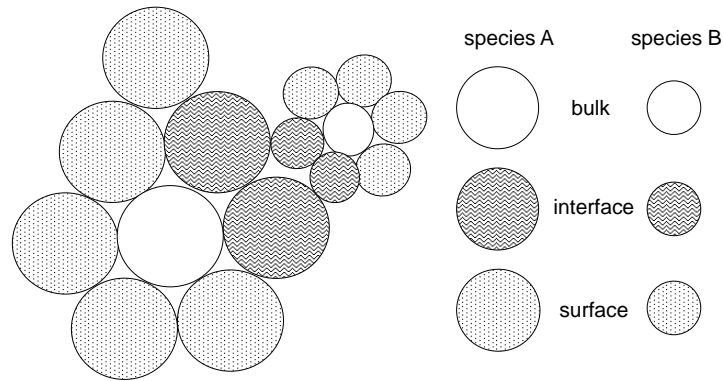


Figure 2.1: Two dimensional cross-section of a hypothetical cluster consisting of two different atomic species, A and B. Different sites in the cluster are termed according to the number and kind of their nearest neighbors.

range of 0.5 - 3 eV [23]. Clusters which are formed via hydrogen bonds, such as water clusters, have mean binding energies per atom in the range of 0.15 - 0.5 eV [23]. Rare gas atoms have closed electronic shells. Clusters made of these species are thus held together only by van der Waals forces and have mean binding energies per atom in the range of 0.001 - 0.3 eV [23]. Mixed clusters consist of more than one atomic or molecular species. Combination possibilities and thus binding mechanisms are manifold.

Besides the type of bonding, a distinction is made according to size. In microclusters, defined as having $N = 2$ to 12 constituents, all atoms are part of the clusters' surface. Small clusters have $N = 13$ to 100 constituents. Their physical properties are strongly dependent on the exact number of atoms. Big clusters have $N = 101$ to 1000 constituents. Their physical properties gradually approach those of the solids or liquids. Clusters with more than 1000 constituents are called small particles or nanocrystals. In this work I will describe experiments on small to big homogeneous and heterogeneous, free and neutral rare gas clusters.

2.1.1 Production of rare gas clusters

Rare gas clusters can be produced using a supersonic expansion. This section summarizes the basic principles of the formation of rare gas clusters as described in more detail in the PhD theses of Funk and Barth [24, 25] and in [26]. The formation of

stable clusters requires temperatures such that $k_B T$ is smaller than the binding energy of the cluster. These low temperatures can be achieved by supersonic expansion. A gas is expanded through an orifice. If the mean free path λ is greater than the diameter of the orifice d , the flow into the vacuum system is molecular. If λ is much smaller than d , the flow is viscous. The latter case goes along with a much greater density and thus mass flow into the vacuum. Additionally, the shape and temperature of the jet changes. Due to many collisions within the jet, the velocities of the individual molecules approach that of the group velocity [27]. Thus, the width of the velocity distribution along the expansion direction, that is the lateral velocity, decreases. The width of the velocity distribution is directly proportional to the temperature of the system, which therefore means that the lateral temperature decreases. Due to energy conservation, then the group velocity increases [27]. The local speed of sound is directly proportional to the square root of the translational temperature. When the ratio of flow velocity to the speed of sound, which is the Mach number M , is greater than one, the beam becomes supersonic. The cooling effect and the directionality of the beam are lost when the background pressure behind the orifice is too high, because this causes too many collisions with residual gas molecules.

The conductance of a nozzle with a diameter d is roughly [27]:

$$C = 15 \frac{d^2 V}{t}, \quad (2.1)$$

with the diameter d in centimeters, the volume V in liter and the time t in seconds.

Therefore, with a nozzle diameter of 0.008 cm and a source pressure of 2 bar, the flow into the expansion chamber is about 1.92 mbar liter/sec. In order to obtain a free mean path of some tens of centimeters, a pressure of about 1×10^{-3} mbar is required. This means, to achieve this pressure in this example, a pumping speed of at least 1940 liter/s has to be installed.

The initial step of cluster growth within the jet is the formation of dimers. Due to momentum conservation, the formation of a dimer requires a three body collision. A trimer can then be formed directly by a collision of the dimer and a monomer. The residual momentum leads to vibration within the trimer. This process continues as long as the mean free path within the jet is much smaller than the orifice diameter. This already shows that the length of the orifice can influence the degree of condensation, defined as the ratio of single atoms to atoms in clusters. It was found empirically that conical nozzles are advantageous if high condensation grades are required.

The number of three body collisions is proportional to the product of pressure squared and nozzle diameter. The molecular flow through the nozzle into the expansion chamber is proportional to the product of pressure and the square of the diameter of

the nozzle. An increase in expansion pressure to achieve a higher condensation grade thus always increases the flow into the chamber. Again, the pumping speed installed at the expansion chamber limits the available expansion pressure.

Supersonic expansion also allows the production of clusters which consist of more than one atomic or molecular species. Generally, two approaches are used here. In the so-called *pick-up* or *doping* method, a homoatomic cluster beam is directed through a volume which holds a high concentration of a second species. Upon collision, the cluster picks up or adsorbs atoms of this second species on its surface. There are a variety of possible binding sites for the adsorbed species. It can form a layer around the parent cluster [28, 29], form a so-called 'guest-cluster' on the parent cluster's surface (compare figure 2.1 and [30]), diffuse into the bulk of the parent cluster [28, 29, 31, 32] or sits on high-coordination sites on the surface of the guest cluster [33].

The second method is called *co-expansion*. Here, a gaseous mixture of two species is expanded through a nozzle into a vacuum. The cluster formation principles are similar to those described for homogeneous clusters. A dimer forms within the jet due to three-body collisions. This dimer then serves as a condensation nucleus for further cluster growth. The species with the higher cohesive energy is more likely to form the dimer [34, 35]. The mixed clusters used for the experiments described in this thesis were produced exclusively via the co-expansion method. The structure and size of clusters produced in this way will be described in the following sections.

2.1.2 Size determination of rare gas clusters

The more accurately the size and structure of the clusters are known, the more precise conclusions can be drawn from the experimental data. A first important quantity is the cluster size. The mean cluster size $\langle N \rangle$ within a cluster jet has a distribution which can be described using a log-normal function [36, 37]. The width of this distribution depends on the expansion parameters. It is, however, generally assumed to be approximately as large as $\langle N \rangle$ itself [28, 37, 38]. This means that, in particular for clusters with a small $\langle N \rangle$, the most prevalent species are not clusters with the size N . Characteristic distributions for two different mean cluster sizes $\langle N \rangle$ measured by Karnbach *et al.* [37] are shown in figure 2.2.

In the case of homogeneous clusters, the mean cluster size $\langle N \rangle$ can be calculated empirically based on the nozzle geometry and temperature, the expansion pressure and the type of expanding gas [39]. In order to compare different cluster sources, Hagena *et al.* combined these parameters into a scaling parameter Γ^* [40, 41]:

$$\Gamma^* = \frac{p_0 d_{eq}^q}{T_0^{5/2-q/4}} K_{ch} \quad (2.2)$$

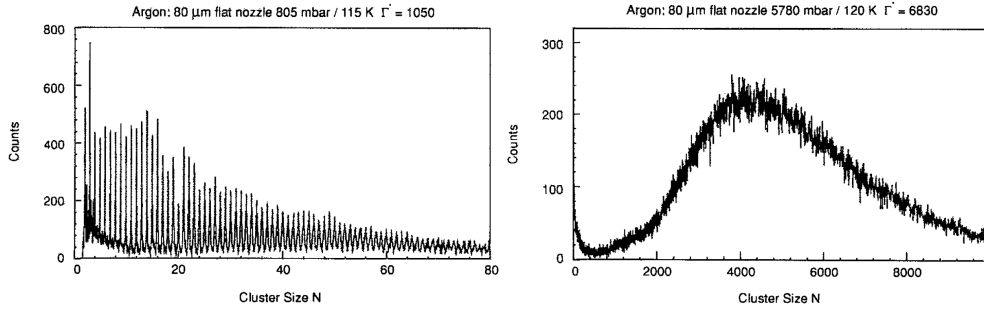


Figure 2.2: Typical mass spectra of argon clusters measured with a time of flight spectrometer. The left panel corresponds to a mean cluster size of $\langle N \rangle = 37$, the right to $\langle N \rangle = 3000$. Reprinted with permission from [37]. Copyright 1993, American Institute of Physics.

Here d_{eq} is the equivalent nozzle diameter for conical nozzles:

$$d_{eq} = \frac{0.736 d}{\tan \alpha} \quad (2.3)$$

with α being half the opening angle of the nozzle and d the smallest diameter of the nozzle. Furthermore, T_0 is the temperature of the nozzle and p_0 the expansion pressure. K_{ch} is a material-dependent constant and can be calculated as explained in reference [41]. Values of K_{ch} used in this work are: $K_{ch}(\text{neon}) = 185$, $K_{ch}(\text{argon}) = 1646$, $K_{ch}(\text{krypton}) = 2980$ and $K_{ch}(\text{xenon}) = 5554$. The scaling parameter q must be determined experimentally. Here, it is set to $q = 0.85$ according to reference [40]. The mean cluster size can now be calculated as:

$$\langle N \rangle = 33 \left(\frac{\Gamma^*}{1000} \right)^{2.35}. \quad (2.4)$$

Other scaling laws exist and Buck *et al.* even introduced scaling laws for different ranges of Γ^* [38]. The value of $\langle N \rangle$ can only be an estimate it is sufficient in this thesis to use formula 2.4 for any given $\langle N \rangle$.

There are, to my knowledge, no scaling laws available for heterogeneous clusters produced via the co-expansion method. Pietrowski *et al.* describe experiments on mixed clusters which are assumed to contain only one atom of one species embedded in a cluster of a different species [28]. In this case, the use of scaling laws is justified. The mixed clusters produced in the experiments presented here do not fulfill this requirement.

Using photoelectron spectroscopy, we have a different way to determine the mean size of the clusters in the ensemble produced via supersonic expansion. The ratio of the

contributions of the bulk and the surface atoms in the photoelectron spectrum (compare section 2.2.2) in combination with a model for the structure of the cluster (compare next section), allows us to draw conclusions about the mean size of the clusters in the beam.

2.1.3 Structure and composition of rare gas clusters

Rare gas clusters show a spherical form. Bonds between rare gas atoms are formed by instantaneous dipole-induced dipole forces, also called *London dispersion forces*. They are a class of *van der Waals forces*. London used second-order perturbative theory to obtain an expression for the attractive interaction between two atoms [42]. He found that the binding energy is proportional to $-1/R^6$, with R as the interatomic distance. At the same time, the *Pauli exclusion principle*, which states that two identical fermions cannot have the same quantum state, provides a repulsive force between two atoms which scales by $1/R^{12}$. Combined, this leads to the so-called *Lennard-Jones-potential* [43, 44]:

$$V = \varepsilon \left\{ \left(\frac{\sigma}{R} \right)^{12} - 2 \left(\frac{\sigma}{R} \right)^6 \right\} \quad (2.5)$$

with R being the internuclear distance and ε the minimum of V with $V(\sigma) = \varepsilon$.

Typical potentials are shown in figure 2.3, it can be seen that different atomic species have different bond strengths. This is due to their differing polarizability. As a consequence, the cohesive energies differ for different species. The cohesive energy reflects the maximum of the binding energy of a single atom in the bulk. To minimize the total energy of the system, the total binding energy is maximized. The more nearest neighbors an atom has, the higher its binding energy is. This means that in a cluster, all atoms should take positions within the cluster with a maximum possible number of nearest neighbors. This should automatically lead to close density packing of the single atoms in the shape of a sphere because the ratio of volume to surface is highest in a sphere. This model allows us to establish an important rule of thumb in cluster

Table 2.1: Cohesive energies, melting temperatures and cluster temperatures of solid rare gas species at 1 atm. After [35, 45]. The cluster temperatures of coexpanded rare gas clusters are taken from Lundwall *et al.* [35] and references therein.

	Argon	Krypton	Xenon
Cohesive energy / (eV/Atom)	0.08	0.116	0.16
Melting temperature / K	83.8	115.8	161.4
Cluster temperature / K	37 ± 5	53 ± 6	79 ± 8

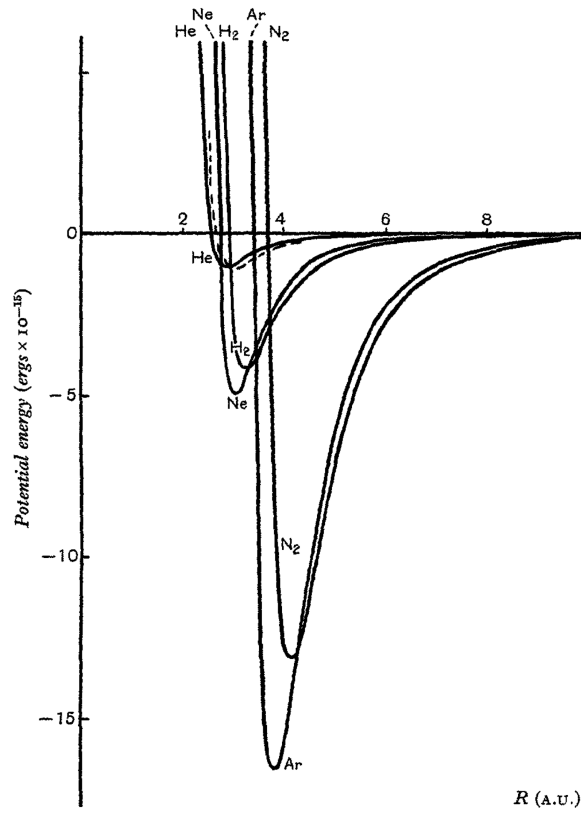


Figure 2.3: “The potential energy of pairs of inert gas atoms as a function of their distance apart in Å.” Reprinted with permission from [44]. Copyright 1931, Institute of Physics.

physics: The ratio of the atoms on the cluster’s surface to the atoms in the cluster’s bulk is proportional to $1/N^{2/3}$, where N is the total number of atoms in the cluster. Any given physical property A of a cluster approaches a value $A(0)$, the value of A measured in the bulk, according to $A \propto N^{-1/3}$. In reality, the cluster structure is more complex and changes, among others, depending on the cluster size, temperature and type of atomic species. Argon clusters formed via supersonic expansion are known to have a polyicosahedral structure if $N < 50$ [46]. The same authors find for argon clusters with $50 < N < 750$ a multilayer icosahedral structure [47]. With increasing cluster size it is expected to depict a *fcc* structure, because this is the structure of bulk argon. Whether, how and at which N this transition occurs is debated [48, 49].

Assuming an icosahedral structure, one can calculate the number of atoms which are

included in a fully formed icosahedron with $n \in \mathbb{N} > 0$ shells as:

$$N_{closed}(n) = \frac{1}{3}(10n^3 - 15n^2 + 11n - 3). \quad (2.6)$$

The number of surface atoms N_s in this system can then be calculated as:

$$N_s(n > 1) = 10n^2 - 20n + 12. \quad (2.7)$$

The binding energy of a cluster should have local minima when $N = N_{closed}$. That is, clusters with $N = N_{closed}$ are more stable than their neighbors with $N = N_{closed} \pm 1$. In experiments, it was found that these clusters are indeed more abundant in mass spectra of cluster jets. These numbers $N = N_{closed}$ are called *magic numbers*. They can directly influence the physical properties of clusters, e.g., melting temperature [50].

The structure of co-expanded heterogeneous clusters has been studied intensively in theory [29, 32, 51] and experiment [28, 52–55]. Clarke *et al.* used the two parameters ε and σ to derive a phase diagram for the morphology of clusters of two species A and B [51]. Values for α and β are given in table 2.2. For the explanation of ε and σ compare figure 2.3 and equation 2.5.

Using:

$$\alpha = \varepsilon_{AB}/\varepsilon_{AA}, \quad (2.8)$$

$$\beta = \varepsilon_{BB}/\varepsilon_{AA}, \quad (2.9)$$

$$\Gamma = \sigma_{AB}/\sigma_{AA} \quad (2.10)$$

and

$$\Delta = \sigma_{BB}/\sigma_{AA} \quad (2.11)$$

they obtain the following results for $\Gamma = \Delta = 1$ and different values of α and β :

Table 2.2: Potential wells ε and interatomic distances σ of the rare gas dimers of interest in this thesis. Data from: [51, 52, 56]. α , β , Γ and Δ are calculated according to [51].

	ε/meV	$\sigma/\text{\AA}$	α	β	Γ	Δ
Ar - Ar	12.4	3.404				
Kr - Kr	17.4	3.63				
Xe - Xe	23.1	3.961				
Ar - Kr	14.4	3.52	0.83	0.71	0.972	0.937
Ar - Xe	16.9	3.72	0.73	0.51	0.94	0.86

1. $\alpha \cong \beta \cong 1$: In this case all interactions are identical. For entropy reasons the clusters must be mixed.
2. $\beta \approx 1$: The intraspecies interactions (AA) are almost identical. With decreasing α , the interspecies interactions (AB) become weaker. The clusters "take an elongated shape with one half of the cluster predominately A and the other predominately B " [51]. With α increasing further, two fused subclusters consisting of A and B , respectively, are expected.
3. $\beta \approx 1$ and $\alpha = 0$: The cluster fragments into two subclusters consisting of species A and B .
4. $\alpha \lesssim 1$: The interactions between AA and AB are nearly equal. With decreasing β the AA interactions become stronger than then the BB interactions. A spherical core of A , coated by particles of species B is expected.
5. $\alpha < 1$ and $\beta < 1$: Neither α nor β are close to 1. A core of species A forms. Species B is expected to partially coat this core.
6. $\beta \approx 0$: For $\alpha \approx 1$, it is expected that species B evaporates and leaves a cluster core of species A behind.

They also determine the effect, that different sizes of species A and B have on the cluster structure. For $\alpha = \beta = 1$ they find that the clusters separate and the larger species lies on the outside of a sphere of the smaller species. They conclude that an Ar-Kr cluster can exist and that the argon atoms form a shell around a krypton core (compare to case 4). They do not explicitly discuss the case of Ar-Xe clusters, but according to their discussion, the formation of Ar-Xe clusters can be expected to follow cases 4 and 5.

Experiments performed by Lundwall *et al.* [54, 55] on Ar-Kr clusters produced via co-expansion confirmed these predictions. They find evidence for radially segregated clusters, in which the krypton atoms form a core surrounded by argon atoms on the surface. However, they find there is no sharp boundary between the layers and conclude that "the cluster has a structure with a radial surface segregation: mainly argon on the surface and dominatingly krypton in the bulk" [54]. Additionally, it was found that krypton atoms found on the clusters' surface occupy high coordination sites [55].

Experiments on Ar-Xe clusters [52, 53, 57] come to similar conclusions as in the Ar-Kr case. The xenon atoms form a core surrounded by an argon shell. Tchapyguine *et al.* found evidence for an interface layer. In other words, the argon and xenon atoms were found to be clearly separated. Both Lengen *et al.* and Tchapyguine *et al.* report

that they found more than one layer of argon, depending on the initial gas mixture and expansion parameters.

In both systems, Ar-Kr and Ar-Xe clusters, the formation of the mixed clusters are also dependent on the mixing ratio of the initial gas. When the amount of the species with the higher value of ε increases above a certain threshold, only this species will be observed in the final clusters [52]. In the experiments on Ar-Kr, mixing ratios which lead to the formation of mixed clusters were in the range of 0.6 to 9 % krypton [54, 55]. Reported mixing ratios for Ar-Xe clusters were in the range of 0.03 to 9 % xenon [30, 53, 57].

2.2 Photoionization

The process by which an atom emits an electron after interaction with a photon is called photoionization or, when a metal is ionized, the photoelectric effect. The emitted electron is called the photoelectron. The photoelectric effect was first described by Hertz [58]. He produced two electric sparks between four electrodes and observed that the occurrence of the first spark influences the electrode-distance dependency of the second spark. He concluded "...dass bis zum Beweise des Gegentheils das Licht des activen Funkens als die nächste Ursache der von ihm ausgehenden Wirkung betrachtet werden müsse"¹. Further experimental work by Lenard [59] led to the conclusion that the effect, is independent of the light intensity and depends solely on the wavelength of the light. Shortly after this Einstein was able to explain this effect theoretically [60]. The principles he describes lead to a simple but fundamental rule: the binding energy of a photoelectron in an atom or molecule can be determined using the difference between the energy of the ionizing photon and the kinetic energy of the free photoelectron. In other words, the measured kinetic energy of the electron is directly related to its binding energy via:

$$E_{bind} = h\nu - E_{kin}. \quad (2.12)$$

According to Koopmans' theorem, these energies are linked to the energy eigenvalues of the Hartree-Fock-orbitals describing the electronic structure of atoms [61].

2.2.1 Photoionization of isolated systems

To look at the ionization process of an isolated atom in more detail, one can start with Fermi's golden rule [62]. For a transition from an initial atomic state $|i\rangle$ to a final atomic

¹ "...that until proven otherwise, the light of the active spark has to be assumed to be the cause of the effect the first spark creates."

state $|f\rangle$, the transition rate w can be calculated as [63]:

$$w = \rho(E) |\langle f | H_{int} | i \rangle|^2 \frac{2\pi}{\hbar} \delta(E_f - E_i) \quad (2.13)$$

with the time independent interaction:

$$H_{int} = \frac{e_0 \hbar}{2m_0} A_0 \sum_j e^{i\mathbf{k}\mathbf{r}_j} \mathbf{P} \cdot \nabla_j. \quad (2.14)$$

Here $|i\rangle$ and $|f\rangle$ are eigenfunctions of the atomic Hamiltonian. ρ is the density of final states. The incident light is described by a plane wave as $\mathbf{A} = \mathbf{A}_0 e^{i\mathbf{k}\mathbf{r}_j}$, with the wave vector \mathbf{k} . \mathbf{P} is the polarization vector derived from $\mathbf{A}_0 = -iA_0\mathbf{P}$, where the vector potential \mathbf{A}_0 contains the field intensity and polarization (for details, see [63]). The expression

$$\langle f | \sum_j e^{i\mathbf{k}\mathbf{r}_j} \mathbf{P} \cdot \nabla_j | i \rangle \quad (2.15)$$

is also called *matrix element*. Using the so-called *dipole approximation*, $e^{i\mathbf{k}\mathbf{r}}$ becomes ≈ 1 . This is valid as long as the photon wavelength is much longer than the dimensions of the irradiated atom. In other words, the variation of the electromagnetic field within the atom is small. In the experiments described here this is the case, because the shortest wavelength used is approximately 12.5 nm. Using commutator relations, the matrix element can also be expressed in the so called *length form* which uses the position operator \mathbf{r} .

From that length form is possible to derive the differential cross section as [63, 64]:

$$\frac{d\sigma}{d\Omega} = 4\pi^2 \alpha \hbar \nu |\langle f | \sum_j \mathbf{r}_j | i \rangle|^2 \quad (2.16)$$

with a_0 being the Bohr radius and α , the fine structure constant, and \mathbf{r}_j , the position operator of the j 'th electron. $\frac{d\sigma}{d\Omega}$ describes the cross section of electron emission into an area element with the solid angle $d\Omega$.

For the photoionization of a non-polarized target with fully linearly polarized light, a different expression for the differential cross section, which includes the so-called *anisotropy* or β -*parameter*, can be derived by insertion of angular dependent spherical harmonics in 2.16:

$$\frac{d\sigma}{d\Omega} = \frac{\sigma}{4\pi} \left[1 + \frac{\beta}{2} (3 \cos^2 \Theta - 1) \right]. \quad (2.17)$$

Θ is the angle between the polarization axis and the direction of the electron emission. The parameter β in formula 2.17 describes the angular momentum exchange of photon

and electron. It is defined in the range: $\beta \in [-1, 2]$. For a value of $\beta = -1$, for example, the emission probability of electrons in the direction of the polarization vector of the incident light is zero. A $\beta = 0$ results in an isotropic emission probability. Usually, β is > 0 and the number of electrons emitted along the polarization vector increases with increasing β .

More possible photoionization or photoexcitation processes exist. The processes can, for example, be distinguished by the numbers of electrons created. Interactions between photon and atom without the emission of a free electron include elastic and inelastic scattering or excitation followed by relaxation via the emission of a photon or via dissociation, as can occur in some molecules. Figure 2.4 shows a schematic of two possible excitation processes; direct photoionization and excitation into a bound Rydberg state.

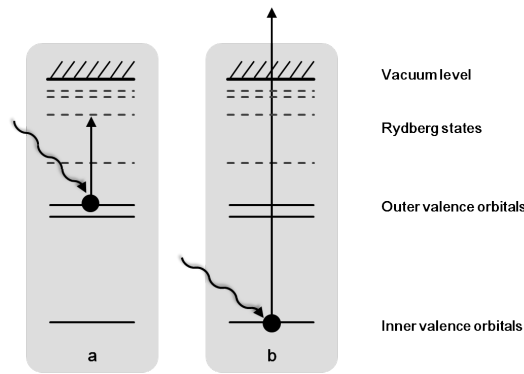


Figure 2.4: Some possible excitation processes in an atom interacting with a photon. a) excitation and b) ionization. (After [65])

Another variant of a photoionization processes is the so called *shake-up* process. Here, the ion is left in an excited state. The difference between excited and ground state energy of the ion is subtracted from the kinetic energy of the emitted electron. The contributions of these processes in the photoelectron spectra are called *satellites*. The excited ion is said to be in a *satellite state*. The satellite states are discrete and element specific; equation 2.12 for the kinetic energy of the photoelectron becomes approximately:

$$E_{kin}(e_1) = h\nu - E_{bind}(e_1) - (E_{bind}(e_2^*) - E_{bind}(e_2)), \quad (2.18)$$

where e_1 is the emitted electron and e_2 the excited electron.

The emission of two electrons from a single atom within one and the same photoionization event requires that the energy of the photon be higher than the double ionization potential (DIP) of the atom or molecule. (Processes where more than one

photon is absorbed do not play a role in the experiments described here.) A distinction is made between a sequential and a direct double ionization. The so-called *shake-off* effect describes a direct photo double ionization. The free electrons are called *shake-off electrons*. The kinetic energies of sequential and direct double ionization processes are related as follows:

$$E_{kin}(e_1) + E_{kin}(e_2) = h\nu - DIP. \quad (2.19)$$

The kinetic energy distribution of the electrons is not homogeneous but shows "a U-shaped profile" [66, 67]. The energy difference between the two electrons tends to increase with increasing excitation energies.

The ionization or excitation processes described may leave the atom in an excited state (compare figure: 2.4) which will eventually decay. Again there are different mechanisms allowed. Autoionization processes are described in section 2.3.1

2.2.2 Photoionization of extended systems

Continuing on from the isolated systems described above, we will now consider extended systems. A partial photoelectron spectrum of argon clusters with a mean size of $\langle N \rangle = 195^1$ stemming from a supersonic expansion source is shown in figure 2.5. Both monomer and cluster contributions can be seen. The monomer contributions are labeled with their atomic quantum numbers. The linewidth of the monomer contributions reflects the energy resolution of the recording instrument. Contributions in the spectrum stemming from clusters are labeled accordingly. They appear at lower binding energies than their respective monomer contributions. In the case of the argon 3s line, the cluster contribution consists of two distinguishable features. The origin of these so called *cluster bands* will be described in this section. Björneholm *et al.* show that the shift in core level electron binding energy can be explained solely using a polarization-screening model [68]. They write that "the surrounding of the core ionized site will be polarized. This polarization screens the ionic final state" and thus lowers the binding energy of the core electron. Considering that polarization effects have a very short range, it is clear that the direct environment of the ionized site has the highest influence on the binding energy. That is, the number of nearest neighbors is the most important factor. Thus the cluster contribution of the argon 3s spectrum (right side of figure 2.5) can be explained easily. The green feature stems from argon atoms sitting on the surface of the argon cluster. The red feature stems from atoms in the clusters' bulk. The width of the features reflects the broad size distribution of the clusters. The

¹ for an explanation of $\langle N \rangle$ compare section 2.1.2

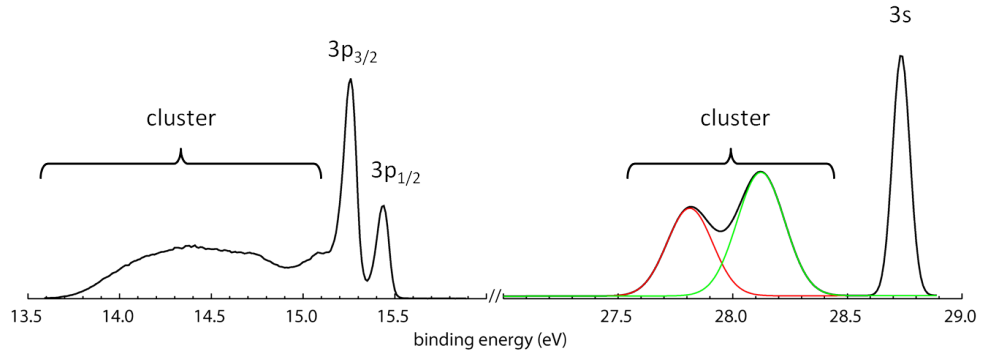


Figure 2.5: Partial photoelectron spectrum of argon clusters with a mean size of $\langle N \rangle = 195$. The black lines show the measured spectrum, the colored lines show fits. The left side, showing the argon $3p$ binding energy region, was recorded with an excitation energy of $h\nu = 77.1$ eV. The right hand showing the argon $3s$ binding energy region was recorded at $h\nu = 90.1$ eV. Parts of the shown spectrum were published earlier in [52].

ratio of the area of the bulk and the surface feature reflect the ratio of surface and bulk atoms in the cluster beam. A schematic explanation is shown in figure 2.6.

The broad unstructured feature on the right side of figure 2.5 in the binding energy range of 13.5 to 15.2 eV stems from outer valence electrons. These highest occupied orbitals overlap and thus form a band. This overlap is an initial state effect, in contrast to polarization screening of inner valence holes. The width of this band in solid argon is approximately 1.7 eV [69]. The delocalization does not allow a sharp differentiation between bulk and surface contributions. Hergenhausen *et al.* come to the conclusion that the spectral shape is influenced by spin orbit effects as well as crystal field effects, while the latter have a stronger contribution [70]. Final state effects also play a role in

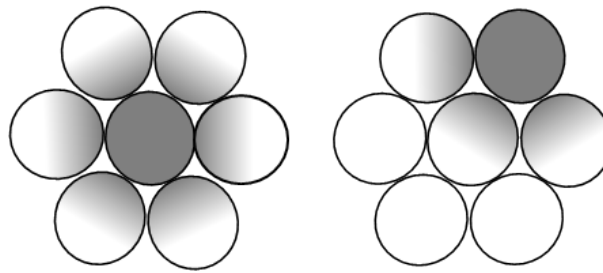


Figure 2.6: Schematic to illustrate the effect of polarization screening in clusters. The completely filled circle represents the ion. The effective screening (gray area) is smaller in the ionization of a surface site, than in the ionization of a bulk site.

the photoelectron spectra of these outer valence bands. Carnovale *et al.* for example, describe the formation of ionic cores in argon clusters [71]. However, both spectral features allow an estimation of the mean size of the measured cluster ensemble. This is explained in more detail in section 2.1.2.

Double ionization potential of extended systems

Another important property of extended systems is that the energy required to remove two electrons from the system is usually smaller than the energy required to remove two electrons from the monomer. This means that the DIP of the monomer is larger than the DIP of the cluster. In the limit of an infinitely large cluster, the DIP should approach twice the single ionization potential of the solid. Two different ionized sites in the cluster are separated so far that the Coulombic forces between them reach zero. In the case of argon, the DIP of the monomer is 43.4 eV [72]; of the dimer, 34.5 eV [6] and for the solid 27.6 eV, as estimated by doubling the single ionization potential of solid argon (13.8 eV [69]).

This lowering of the DIP is necessary for the non-local autoionization processes described in this thesis. A simple relationship expresses the possibility of autoionization in extended systems. The ionization potential of the initial vacancy must be greater than the sum of the ionization potentials of the final vacancies plus the Coulombic energy between these two vacancies. This also means that the kinetic energy of the resulting, i.e. the autoionized electron, can be estimated as:

$$E_{kin(e2)} = IP_i - IP_{f1} - IP_{f2} - E_{c(f1,f2)} \quad (2.20)$$

Here, IP stands for ionization potential, the Coulombic energy can be calculated after:

$$E_{c(f1,f2)} = \frac{1}{4\pi\epsilon_0} \frac{e^2}{r_{f1,f2}} \quad (2.21)$$

where e is the unit charge, $r_{f1,f2}$ is the distance between the final vacancies and ϵ_0 is the permittivity of the vacuum.

Electron scattering in extended systems

The electron produced via photoionization in an extended system may also scatter within this system. If this scattering is elastic, it does not influence the kinetic energy of the electron. However, it may influence the β parameter as described by Rolles *et al.* [73]. If the outgoing electron undergoes inelastic scattering, energy is exchanged. Two relevant inelastic scattering processes are the creation of excitons and the ionization of

a second site within the system, or *secondary ionization*. Excitons are "metastable but delocalized electron-hole pairs" [74]. The distinction can be made between bulk and surface excitons [75] which again differ in their binding energy.

The study by Hergenhausen *et al.* shows that the exciton is created due to inelastic scattering as opposed to the "creation of a quasi-particle at the site of the original ionization" [74]. In small neon clusters they observed an *energy loss* feature with an energy loss of 17.6 eV compared to the neon $2p$ main line. Thus, to create an exciton, one must excite the neon clusters with an energy of at least 17.6 eV above the $2p$ binding energy. The first excitonic satellite peak of argon clusters was found to have an energy loss of 12.2 eV compared to the argon $3p$ main line [74].

Secondary ionization results in the creation of two free electrons. To be energetically allowed, the outgoing electron has to have sufficient kinetic energy to ionize the cluster. This means that $h\nu \geq DIP$. The kinetic energies of the two outgoing electrons follow equation 2.19. Pairs of electrons with maximum energy difference occur more frequently. The scattering probability of an electron within a cluster can be described using the *escape depth* or *attenuation length* λ . λ is generally dependent on the kinetic energy of the electron. Using photoelectron spectroscopy on thin films of rare gases, Schwentner *et al.* [69, 76] show that λ changes from 1000 Å at the threshold for inelastic scattering to only 5 Å for electrons with a kinetic energy of 10 eV above threshold. Tchapyguine *et al.* [77] later show how these effects influence the size estimation of rare gas cluster using photoelectron spectroscopy and the comparison of bulk and surface contributions.

Single and double ionization potentials for the rare gases relevant in this thesis are summarized in table 2.3. This table also includes the values for the onset of electron scattering in the bulk and the DIPs of the rare gas dimers.

Table 2.3: Single (*IP*) and double (*DIP*) ionization potentials of neon, argon, krypton and xenon in the form of monomers (*mono*), dimers (*dim*) and bulk (*bulk*). $E_{sc(bulk)}$ is the onset of electron scattering in the bulk material. Entries marked with *calc.* are calculated values, * is calculated as twice the band-gap energy E_G . All values are in eV.

	IP_{mono}	IP_{Bulk} [76]	$E_{sc(bulk)}$ [76]	DIP_{mono}	DIP_{bulk} [78]	DIP_{dim}
Ne	21.56 ^[79]	20.3		61 ^{[80], calc.}	43.4 ^{[69], *}	46 ^{[80], calc.}
Ar	15.76 ^[81]	13.8	24.5	43.4 ^[72]	28.6	34.85 ^[82]
Kr	14.00 ^[79]	11.9	20.5	38.4 ^[83]	25.0	31.15 ^[82]
Xe	12.13 ^[79]	9.8	17.0	33.3 ^[84]	20.9	27.1 ^[82]

2.2.3 Photoionization of crystalline systems

Farges *et al.* interpreted their electron diffraction data of small to large argon clusters in terms of an icosahedral structure [46, 47]. Later, Kakar *et al.* found that argon clusters with sizes above approximately $\langle N \rangle \geq 200$ show “structural effects with *fcc* imprints dominating” the data [49]. This means that a transition to an *fcc*-structure occurs at cluster sizes of approximately $\langle N \rangle \geq 200$. Other studies found that clusters at that size show *fcc* as well as *hcp* structures [85]. The rare gas solids are known to exhibit an *fcc* structure [86].

In a crystal, the atomic cores are periodically arranged. Therefore, an electron in a crystal is subject to a periodic potential. The electron in such a periodic potential can be described as a so-called *Bloch wave*: $\psi_{n\mathbf{k}}(\mathbf{r}) = \exp^{i\mathbf{k}\mathbf{r}} u_{n\mathbf{k}}(\mathbf{r})$. Here, \mathbf{k} is the wavevector. The so-called *dispersion relation* describes the dependence of \mathbf{k} to the energy of the electron. For free electrons this is: $E(\mathbf{k}) = (\hbar\mathbf{k})^2/2m$. The solutions of the Schrödinger equation with a periodic potential have to have the same periodicity as the potential itself. In a crystal with a period length a , the possible electron energies split at the Brillouin-zone boundaries (defined by $k = \pm\pi/a$). This is because the electrons have probability densities between the ionic cores and at the sites of the ionic cores. This separation in potential energy of the probability densities is the so-called *band-gap*.

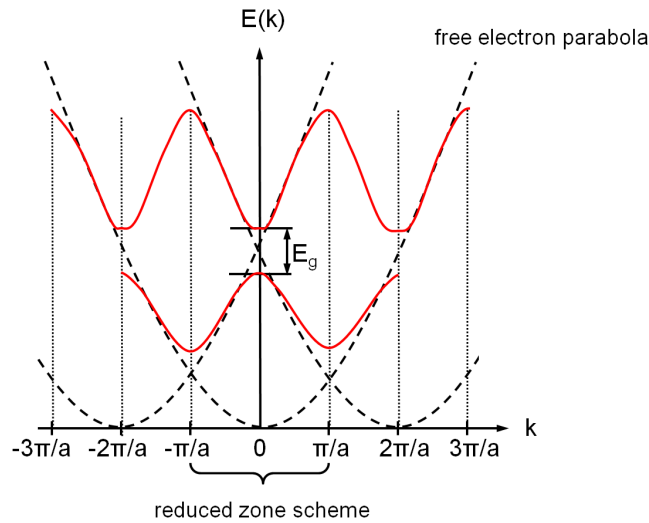


Figure 2.7: Schematic of the energy of electrons in a one dimensional periodical potential with period length a derived from the free electron parabolas (dashed lines). After [87].

Figure 2.7 shows the energy relation of an electron in a periodical potential in the so-called *zone scheme*. The *reduced zone scheme* is limited to the boundaries of the

first Brillouin zone. The figure represents a band structure of an isotropic crystal. It depends on the relative position of the bands towards each other and on the degree to which they are filled by electrons, whether a material is considered an insulator, a semiconductor or a conductor. Rare gas solids have completely filled valence bands, empty conduction bands and a large band gap. This means they are insulators.

The band structure of realistic crystals show strong deviations from that shown in figure 2.7. The reason is that both the period length as well as the amplitude of the potential are dependent on the direction within the crystal. Therefore, $E(\mathbf{k})$ is usually given in selected crystal directions of high symmetry. Especially in the case of rare gas solids, with strongly bound valence electrons and a large bandgap, a free electron parabola cannot be considered a good estimate.

In order to measure the band structure of a crystal, photoemission spectroscopy can be used [87, 88]. A crystal is ionized by monochromatic light with an energy higher than the working function of the material. An electron analyzer measures the resulting electron energy distribution curve (*i.e.* the photoelectron spectrum) under a fixed angle. In the ionization process both the momentum and the energy of the photoelectron must be conserved. The energy is provided by the ionizing radiation, the momentum by the crystal lattice. This momentum is quantized and equals a multiple of the reciprocal lattice vector (\mathbf{k}) [89]. Therefore, by selecting the emission angle of the electrons it is possible to select a k direction of the crystal, provided the orientation of the crystal is known (using low energy electron diffraction (LEED), for example). By changing the excitation energy at this fixed position of crystal and analyzer it is now possible to measure the dispersion along the selected crystal direction (see for example [90]).

2.3 Autoionization

The process by which an excited system emits an electron is called autoionization. The word *auto* here implies, that the ionization process is independent from the process which led to the initial excitation.

2.3.1 Autoionization of isolated systems

An electronically excited atom or molecule can relax by filling the core hole vacancy with an electron from a higher lying orbital if a possibility to remove the excess energy from the system exists. This can occur via the emission of a photon (fluorescence) or the emission of an electron. If the electronically excited atom is ionic, the autoionization process is called *Auger decay* (compare figure 2.8). Generally, in an Auger decay, a core hole is filled by an electron from an energetically higher lying orbital of the

same ion. The excess energy is used to remove another electron from the same ion. The Auger process is usually assumed to be independent from the initial ionization process, in particular if the difference of the kinetic energies of the photoelectron and the Auger-electron is large. This means that the Auger process can be described in a two-step model. Two-step here means that the matrix element can be separated in a component describing the dipole-atom interaction and a component describing the coulomb interaction of the ion and the outgoing Auger electron.

It is important to mention that the Auger decay is a local process. The orbitals participating in the decay have to possess components localized at the nucleus. The reason is that “the normal Auger electron is fast and its wavefunction oscillates rapidly” [2].

Because the energy levels in an atom are discrete, the resulting energy spectrum of the Auger electron is discrete and characteristic for each element. For elements with Z below 30 the Auger decay is the dominant decay process. Elements with higher Z values are more likely to decay via the emission of a photon. The two processes are shown schematically in figure 2.8.

Other possibilities for autoionization exist, including, for example, participator resonant Auger decay and spectator resonant Auger decay. After the excitation of a core level electron into a bound Rydberg state the excited but uncharged atom decays via emission of an electron. If the initially excited electron participates in this decay, the process is called *participator decay*. If not, it is called *spectator decay*.

The processes described so far are local processes. This means that the environments of the excited species are not considered. The next two sections will describe the influence the environment will have on the described effects and how new decay

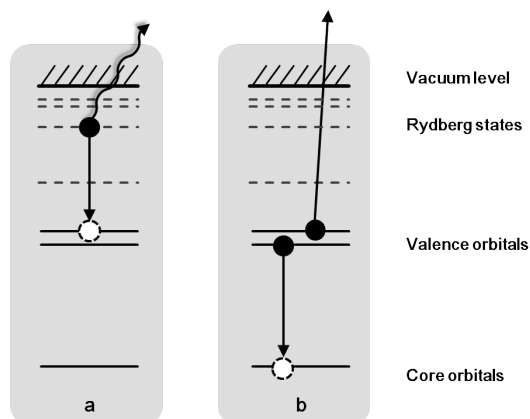


Figure 2.8: A schematic of two possible decay channels of an excited atom or ion. a) fluorescence and b) Auger decay.

channels open due to new possibilities to remove excess energy.

2.3.2 Autoionization of extended systems

2.3.3 ICD

According to table 2.3, a neon $2s$ vacancy cannot decay via autoionization. To reach a doubly charged state of the neon atom, at least 61 eV are required. A decay of the neon $2s$ vacancy in the dimer, with a DIP of 46 eV, into a doubly charged state, is energetically possible if the charge after the decay is located at the two different atomic sites of the dimer. This process, however, would require a transfer of energy or of charge to the neutral atom of the dimer.

A process of this sort was not known until Cederbaum *et al.* predicted the so-called Interatomic Coulombic Decay ICD^1 [2]. The matrix element which describes this process is:

$$\left| \int k^*(\mathbf{r}) v_i^*(\mathbf{r}') \frac{1}{|\mathbf{r} - \mathbf{r}'|} v_f(\mathbf{r}) v_f'(\mathbf{r}') d\mathbf{r} d\mathbf{r}' \right|^2 \quad (2.22)$$

Here “ $v_i(\mathbf{r})$ is the orbital of the initial inner-valence vacancy, $k(\mathbf{r})$ is the scattering wave function of the ejected electron, and $v_f(\mathbf{r})$, $v_f'(\mathbf{r})$ are the orbitals of the two resulting vacancies” [2]. In ICD, as opposed to Auger decay, only $v_i(\mathbf{r})$ and $v_f'(\mathbf{r})$ have to overlap, i.e. they have to be situated on the same monomer. Due to the relatively low kinetic energy of the outgoing ICD electron, $v_f(\mathbf{r})$ can be at a neighboring monomer. The theoretical aspects are covered in more detail in references: [91–94]. Hergenhahn gives a summary of the most important findings of Santra, Cederbaum and Averbukh as follows [4]:

1. Equation 2.22 can be expressed using a direct term and an exchange term. The decay mechanism described is shown schematically in figure 2.9. The direct decay channel is the dominant one and only if it is hindered, the exchange term may become relevant. Jahnke *et al.* [95] showed that this is the case in the ICD of neon $2p$ shake-up states.
2. If no overlap between $v_f(\mathbf{r})$ and $v_f'(\mathbf{r})$ exists, the ICD rate is proportional to R^{-6} . With a van der Waals radius of 1.54 Å [96] and a internuclear distance of 3.1 Å [56] this should be the case in the neon dimer. If the orbitals overlap more extensively, the decay rate towards smaller R increases much faster than R^{-6} . It was suggested by Thomas *et al.* [97] that an expression found by Matthew and

¹ if the entities participating in the decay process are molecules ICD stands for Intermolecular Coulombic Decay

Komninos [98] for the width of the interatomic Auger decay rate could be used to estimate the decay rate for ICD:

$$\Gamma = \frac{3\hbar}{4\pi} \left(\frac{c}{\omega}\right)^4 \frac{\tau_i^{-1} \sigma_f}{R^6}. \quad (2.23)$$

Here τ_i^{-1} is the inverse radiative lifetime of the initial vacancy and σ_f is the total photoionization cross section of the final vacancy. ω is the frequency of the virtual photon. Averbukh *et al.* [93] later found that this expression indeed gives an appropriate estimate for very large interatomic distances. Note that the lifetime is inversely proportional to the decay width: $\tau = \hbar/\Gamma$.

3. Another known energy transfer decay in which the decay rate depends on the distance $\propto R^{-6}$, is the so called *Förster resonant energy transfer* [99]. Here, a virtual photon is resonantly exchanged between two discrete electronic states. This requires nuclear motion and the decay thus falls within time scales in the range of picoseconds. No nuclear motion is required in ICD, because it involves the transition into a continuum state. ICD is therefore an ultrafast decay process in the range of femtoseconds.
4. The decay rate is strongly influenced by the number of nearest neighbors of the initially excited entity. This means that with an increasing number of neighbors, the decay width decreases.

The first experimental proof of the existence of ICD was given by Marburger *et al.* [100]. They showed that ICD occurs in neon clusters after the creation of a $2s$ vacancy. Shortly after Jahnke *et al.* measured ICD on the neon dimer [101]. Since then, as predicted by Cederbaum [2], ICD was found to occur in many more variants and systems including ICD of hydrogen bonded systems [8, 102] and mixed noble gas clusters [19, 103], ICD of satellite states [82, 95, 104], ICD after Auger decay [105, 106] and resonant ICD [107, 108]. Additionally ICD is predicted to occur in endohedral fullerenes [109] and in xenon fluorides [110]. A review of these experiments and concepts was made by Hergenhahn [4].

The aforementioned resonant ICD process can be seen as analogous to the resonant Auger processes. The initial site is not ionized, rather an electron from an inner vacancy is excited into a bound state. An electron is emitted from a neighboring atom by either recombination of the excited electron with the vacancy (participator resonant ICD) or by the recombination of another outer valence electron with the vacancy (spectator resonant ICD).

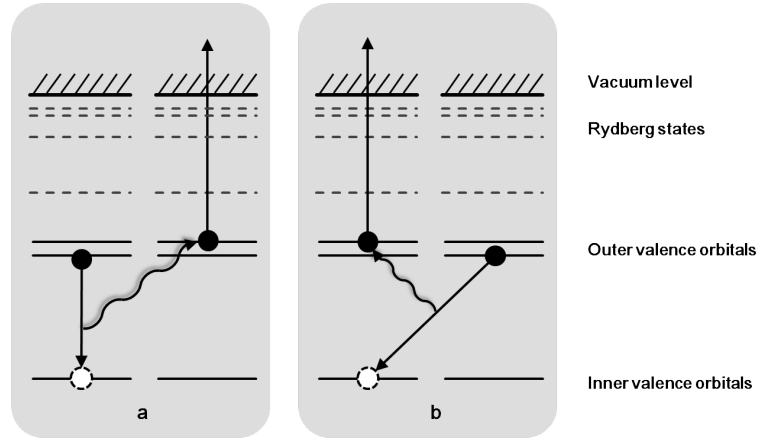
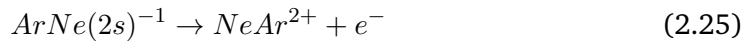
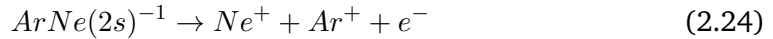


Figure 2.9: Schematic of the ICD mechanism (adapted from [92]). The energy transfer mechanism (a) is associated with the direct term of the coupling matrix element. The electron transfer mechanism (b) is associated with the exchange term. The latter is "of minor importance" [92] and becomes relevant only if the dipole transition is hindered, as, for example, in the decay of Ne $2p$ shake-up states [95].

2.3.4 ETMD

In contrast to ICD, which involves an efficient energy transfer between the participants, another decay process which is based on an electron transfer was predicted [3]. It was termed *Electron Transfer Mediated Decay* (ETMD). Zobeley *et al.* described this process the first time as a competing process to ICD in a neon argon dimer. I will use their first description to introduce the effect here. Energetically, after the creation of a neon $2s$ vacancy in a neon-argon dimer, these two decay channels may be possible:



Decay 2.24 requires an energy transfer and is the previously described ICD. Decay 2.25 clearly requires the exchange of an electron. In their paper, Zobeley *et al.* elaborate on the competition between the two processes and come to the following conclusions [3]:

1. Both processes contribute to the decay width of the initial vacancy. This is somewhat analogous to the competing exchange and direct matrix elements in ICD. At an equilibrium ground state distance of the neon argon dimer, the ICD process is about four orders of magnitude more efficient.
2. With decreasing internuclear distance, the contribution of the ETMD to the elec-

tronic decay width becomes considerably larger. At small internuclear distances, ICD is only one order of magnitude more efficient. This reflects the strong dependence of the ETMD on the distance between the participating entities. While the decay rate of ICD shows an R^{-6} dependency (and an exponential dependency if an orbital overlap is given), "an ETMD process crucially depends on the orbital overlap" [6].

3. The lifetime of the vacancy is 30 fs at equilibrium ground state distance. It decreases strongly with decreasing distances. The ETMD decay width decreases faster than the ICD decay width with decreasing distances. The individual contributions of both decays therefore depend sensitively on the geometry of the system.
4. Due to the weak and undirected coupling in the neon argon dimer, the electron transfer is unfavorable. However, ETMD is "expected to be enhanced in any system comprising subunits with more directional and stronger interactions."
5. A variant of ETMD, requiring the participation of three atoms has been suggested. The initial vacancy can decay via ETMD, ionizing two neighboring argon atoms, thus creating a situation where the final energy is lowered even further due to the separation of the final charges. Due to the participation of three atoms, this variant is termed *ETMD(3)*.

Schematics of ETMD(2) and ETMD(3) are shown in figure 2.10. Both processes

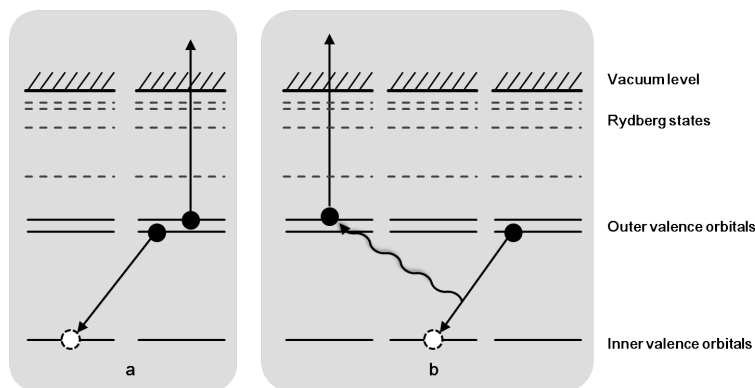
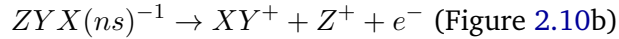
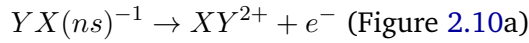
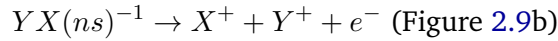
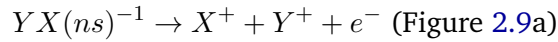


Figure 2.10: Schematic of two different ETMD decays. An inner valence vacancy is filled via electron transfer from an outer valence level of a neighboring atom. Simultaneously the same neighboring atom emits an electron, case (a) or another neighboring atom emits an electron, case (b). These decays are termed *ETMD(2)* and *ETMD(3)*, respectively.

require a charge transfer. In the case of ETMD(2), an electron is transferred to a

neighboring vacancy and the excess energy is used to autoionize the atom from which the transferred electron stems. The result is that the initially excited atom is now neutral and the neighboring decay partner is doubly charged. In ETMD(3), a vacancy is also filled via electron transfer from a neighboring atom. The excess energy, however, is in this case used to ionize a third decay partner. After the decay, the site with the initial vacancy again is neutral and two singly charged neighbors are present.

This means that in contrast to the ICD processes shown in figure 2.9, a distinction between ICD and ETMD can be made regarding the final state. From:



it can be seen that the site of the initial vacancy is neutral after ETMD and ionized after ICD. This simple distinction fails, however, if the aforementioned resonant ICD mechanisms are considered.

Stoychev *et al.* showed that ETMD is a decay channel just as general as ICD [111] and that in many cases both processes are energetically possible. Due to the spatial separation of the final vacancies, ETMD(3) may even be energetically favored to ICD. However, as long as ICD is possible, ICD is usually the dominant channel.

Later theoretical work by Müller *et al.* [9] and Pernpointner *et al.* [6] showed that, if energetically allowed, ETMD may, in fact, become the dominant decay process in weakly bound systems. In principle, this is the case if ICD is not possible or at least very unlikely. There are several scenarios where this is the case. Assuming that ETMD is energetically possible, then it might be observable if:

1. ICD is energetically not possible. This was predicted to be the case in the decay of an Ar $3s$ vacancy in an Kr–Ar–Kr trimer [6].
2. no electron is available at the initially excited site. For example, this is the case in solvated lithium ions as described by Müller *et al.* [9]. Solvated lithium ions have only two electrons. If one $1s$ electron of the solvated lithium is removed, then an electron transfer from a neighboring water molecule can take place. The excess energy can either be removed from the same water molecule (ETMD(2)) or a neighboring water molecule (ETMD(3)) if at least two water molecules are present. They calculate the lifetime of ETMD(2) to be approximately 100 fs if one water molecule is present. The lifetime of the decay decreases with increasing number of water molecules in the cluster and reaches values of approximately

20 fs if five water molecules are present. They do not give decay rates for ETMD(3) other than: “We estimate that ETMD(3) contributes less than 50 % to the decay rate of $\text{H}_2\text{O}_4\text{Li}^+$ and, of course, much less to that of the smaller clusters.”

3. ICD is not allowed due to selection rules. This is analogous to the aforementioned ICD of Neon $2p$ shake-up states [95].

Parts of this thesis will present the first experimental observation of ETMD in heterogeneous clusters consisting of argon and krypton. Another part of this thesis will discuss the co-occurrence of ICD and ETMD in heterogeneous clusters of argon and xenon. More detailed discussion regarding the respective ICD and ETMD processes can be found in these chapters.

3 Experimental overview

3.1 The light source

The experiments described in this thesis were made at the electron storage ring BESSY II in Berlin which is a source for *Synchrotron radiation* (SR). BESSY provides monochromatized radiation in the terahertz region up to hard X-rays.

Accelerated charges emit electromagnetic radiation. SR is the emission of light by relativistic charges on circular orbits. SR was first observed in 1946 by Elder *et al.* [112]. The following properties of SR are important for researchers (adapted from [113]):

1. SR has a very broad spectrum. With appropriate monochromators, one can select the appropriate wavelength for a particular scientific problem.
2. SR has a high photon flux.
3. SR has a high brilliance. This means that a strongly collimated beam is generated with a small divergence and a small source size.
4. The last two points are also true for new generation Free Electron Lasers, however, many mature experimental techniques to address material science problems are already well established for SR, which is not yet the case for FEL radiation.
5. SR has a high spatial stability in the range of micrometers.
6. SR can be produced in any polarization, from linear to circular.
7. SR has a pulsed time structure with pulse lengths as short as approximately ten picoseconds.

The next sections describe the principles and techniques for the production of SR in more detail.

3.1.1 Dipole radiation

The directional energy flux density of an accelerated dipole, also called *Poynting vector*, is proportional to $\cos \phi^2$:

$$\mathbf{S} = \mathbf{E} \times \mathbf{H} \propto \cos^2 \phi \quad (3.1)$$

where ϕ is the elevation angle with respect to the direction of the acceleration. This means that the maximum flux of a dipole is in the direction perpendicular to the acceleration. It is symmetrical with respect to the azimuth θ . The accelerated charges in synchrotrons travel at velocities close to the speed of light: $\beta = v/c \approx 1$. This means that equation 3.1, which is only valid in the electrons resting frame of references, has to be transformed into the laboratory frame of reference and now becomes:

$$\mathbf{S} \propto \beta^4 \frac{1 - \beta \cos \theta^2 - (1 - \beta^2) \sin^2 \theta \cos^2 \phi}{(1 - \beta \cos \theta)^5} \quad (3.2)$$

This means that a relativistic electron (or positron) traveling through a magnetic field emits radiation into a very small opening angle. At BESSY, with a kinetic energy of the electrons of about 1.7 GeV, this is approximately $300 \mu\text{rad}$. The size of the electron bunches defines the source size of the radiation and is in the order of tenths of a millimeter. As mentioned before, the energy distribution of the radiation is broad. However, the number of photons emitted per energy interval follows a characteristic curve with a maximum at the so called *critical energy*, ε_c . For photon energies smaller than ε_c the number of emitted photons is proportional to $N(\varepsilon) \propto \varepsilon^{1/3}$ beyond ε_c the number of emitted photons drops very fast: $N(\varepsilon) \propto \varepsilon^{1/2} * e^{-\varepsilon}$. ε_c can be calculated depending on the radius r and the kinetic energy E of the electrons to [114]:

$$\varepsilon_c = \frac{3\hbar c}{2r} \frac{E^3}{(mc^2)^3}. \quad (3.3)$$

The timing structure of the radiation depends on the so-called *filling pattern* of the synchrotron. The more electron bunches are fitted into the storage ring, the higher the total photon flux will be. Some experiments, like the ones described in this thesis, measure the time difference between the light pulse and the detection of a resulting particle. These measurements require a fixed time difference between the light bunches in the order of the time of flight of the particles which will have to be detected. The number of electron bunches in the storage ring can be reduced for these experiments. The maximum available time difference between two subsequent bunches is dependent only on the velocity of the electrons c and the circumference of the storage ring. The mode of operation with only one electron bunch in the storage ring is called *single bunch mode*. At BESSY, with a circumference of 240 m, the time between two light pulses in single bunch mode is 800 ns. A quantity which includes the aforementioned parameters is the so-called *brilliance* or *luminosity*, L . It is defined as the number of photons divided by illuminated area, solid angle, time and 0.1 % spectral bandwidth.

To increase the photon flux, so-called *wigglers* were invented. In principle, this device consists of a number N of bending magnets in close repetition, in which the direction of the magnetic field alternates. The electrons are accelerated in each segment and the flux of photons is thus N times the flux that a single bending magnet could produce. The radiation characteristics are otherwise comparable to that of a single bending magnet.

A further refinement of the wiggler is the *undulator*. It also consists of a series of bending magnets with alternating direction of the magnetic field. The sinusoidal path of the electrons through the undulator is set such that constructive interference leads to a sharp increase in brilliance. A schematic of an undulator is shown in figure 3.1(a) along with a diagram illustrating the formation of the interference:

$$d = \frac{\lambda_0}{\bar{\beta}_z} - \lambda_0 \cos \theta = n\lambda. \quad (3.4)$$

With:

$$\bar{\beta}_z = 1 - \frac{1}{2\gamma^2} \left(1 + \frac{K^2}{2} \right) \quad (3.5)$$

and the so called *undulator parameter*:

$$K = \frac{eB_0\lambda_0}{2\pi mc}, \quad (3.6)$$

equation 3.4 becomes:

$$\lambda_n = \frac{\lambda_0}{2\gamma^2 n} \left(1 + \frac{K^2}{2} + \gamma^2 \theta^2 \right). \quad (3.7)$$

This is the so-called *undulator equation*. The emitted radiation now shows a sharp distribution around λ_n . By changing the undulator gap, and thus K , one can tune the undulator to the required photon energy. In contrast to the wiggler, in the undulator, the number of emitted photons is proportional to the square of the number of undulator segments.

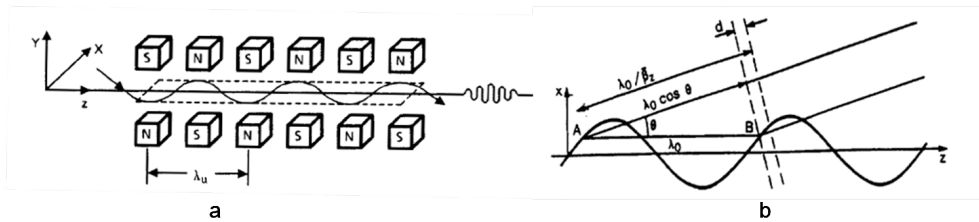


Figure 3.1: Schematic of an undulator (a) and schematic of the principle of constructive interference of the undulator beam (b). From [115], available under Creative-Commons Attribution 2.5 Generic license.

Light produced by the previously described devices is polarized linearly in the plane of the synchrotron ring. Using more complicated magnet arrangements, it is also possible to produce light of any other polarization. In principle, the electrons in undulators of this type follow a helical path.

All experiments described here were made using linearly polarized light. The experiments were made at the beamlines TGM-4 and UE112-PGM-2a. TGM4 is a simple bending magnet, UE112 is an undulator of the APPLE2 type with 32 periods, a period length of $\lambda_0 = 112\text{mm}$ and a minimum bandgap of 22.2 mm. The energy resolution of UE112-PGM-2a is given as $< 1\text{meV}$ for $E < 100\text{eV}$ [116]. The resolution of TGM-4 is given as $\Delta E = 156\text{meV}$ at 72.7 eV [117].

3.2 Experimental setup

The experiments described in this thesis were made in a vacuum chamber. Some reasons for doing this are the high absorption cross section of the x-rays in air, the use of a micro channel plate (MCP), the operation of a cold cluster source and the purity of the targets. This section describes the technical aspects of the experimental chamber used. The magnetic bottle electron analyzer and the cluster source are part of the vacuum setup. Due to their importance in the experiment, sections 3.3 and 3.4 will be devoted to describing them in detail.

3.2.1 Experimental chamber

The experimental chamber is a vacuum chamber held in a movable aluminum frame. We can define three perpendicular axes, which meet in the interaction region. The light propagation axis and the clusters path span a horizontal plane. The electron detectors' symmetry axis is perpendicular to that plane.

Along the light propagation axis are the differential pumping section, the interaction region and a beam dump; a piece of copper pipe that was bent and pinched on one side. Connected to this copper dump is an Ampere meter for monitoring the light intensity. Along the clusters' path is the movable cluster source, a conical skimmer¹ with a 1 mm hole, the interaction region and a cryogenic pump. The electron detector consists of an 800 mm long drift tube and an MCP above the interaction region and a movable magnetic tip below the interaction region. Electrons generated by ionization of the cluster beam are bent upwards into the drift tube and detected by the MCP. A schematic of the setup without the mount can be seen in figure 3.2. To ensure that all three

¹ Beam Dynamics, Inc., 13749 Shelter Cove Drive, Jacksonville, FL 32225 USA

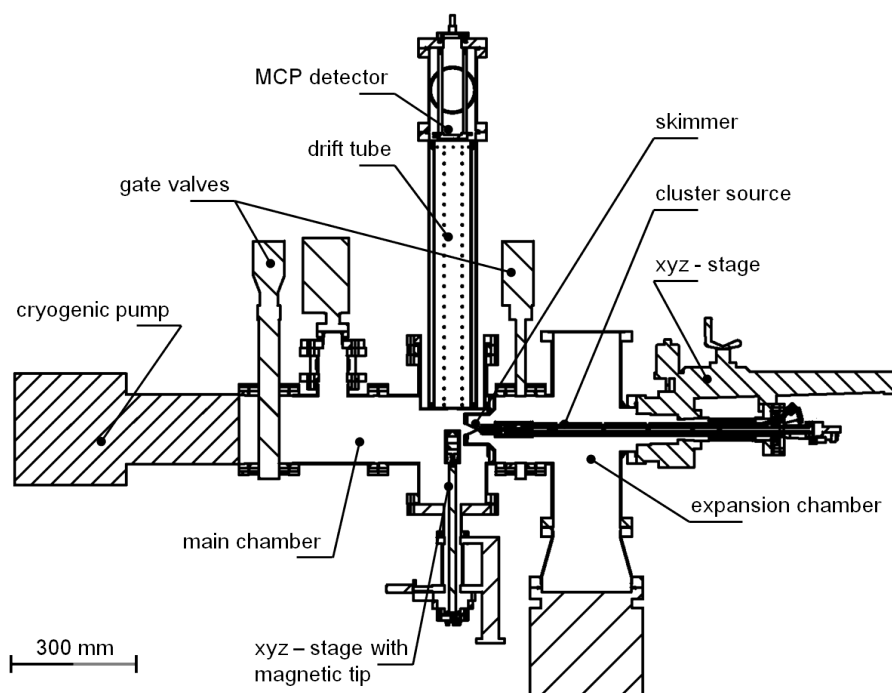


Figure 3.2: Schematic of the experimental setup used. The synchrotron radiation axis is perpendicular to the plane of the diagram.

axes described meet at the same point, the chamber must be aligned. The chamber stands on three air-cushioned feet which can be moved on a glass plate using three fixed micrometer screws. This way, it is possible to move the approximately 300 kg chamber with ease, high precision and high reproducibility. The overlap of a small optical laser beam shot through the cluster source and the skimmer with the zero'th order synchrotron radiation is used to align the height and position of the chamber along the cluster path axis. A plumb-line along the electron detectors' symmetry axis facilitates alignment along the light path. After this geometrical alignment, it is sometimes necessary to align the spectrometer again during operation to improve parameters such as countrate, background signal and resolution.

3.2.2 Vacuum generation

The experiment requires controlling of the pressure in three areas of the experimental chamber: the interaction region with the electron detector (main chamber), the differential pumping section and the expansion chamber. A schematic of the vacuum

setup is shown in figure 3.3. The pressure in the beamline should not rise above a certain threshold to avoid excessive adsorption of atoms or molecules on the surfaces of the optical components of the beamline. The exact threshold is dependent on the composition of the residual gas, but should not exceed 5×10^{-9} mbar.

The pressure in the main chamber can reach up to 5×10^{-6} mbar during an experiment. Therefore it is necessary to install a differential pumping section between the main chamber and the beamline. This differential pumping section consists of two volumes which are separately pumped by turbomolecular pumps¹ with a total pumping power of 600 l/s. The volumes are separated from each other and from the beamline by capillaries to reduce the molecular flow towards the beamline.

The main chamber is directly pumped by a 510 l/s turbomolecular pump² and can additionally be pumped by a cryogenic pump³ with a pumping power of 900 l/s. This cryogenic pump is separated from the main chamber by a gate valve to allow for regeneration after each shift.

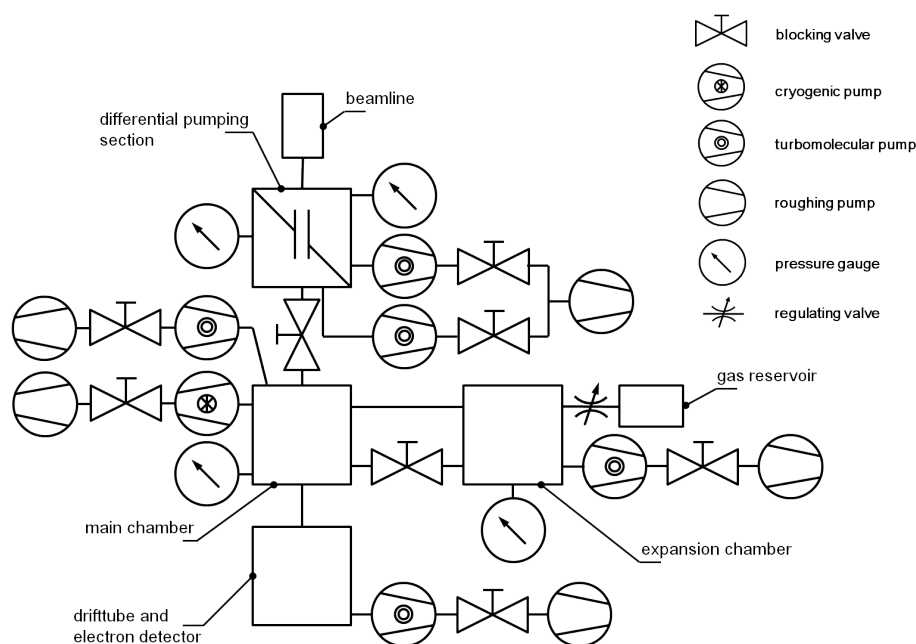


Figure 3.3: Schematic of the vacuum setup used.

¹ Varian V300HT and Varian Turbo-V 301, Agilent Technologies, Alsfelder Straße 6, 64289 Darmstadt, Germany

² Pfeiffer TMU521YP, Pfeiffer Vacuum GmbH, Berliner Straße 43, 35614 Asslar, Germany

³ Leybold RPK 900 Kryo, Oerlikon Vacuum Germany, Industriestraße 10b, 12099 Berlin, Germany

The expansion chamber contains the cluster source and is separated from the main chamber by a conical skimmer with a diameter of 1 mm. It is pumped by a 1000 l/s turbomolecular pump¹. The pumping speed of this pump drops rapidly when the inlet pressure exceeds approximately 5×10^{-3} mbar. This limits the maximum flow through the gas inlet and thus the maximum available cluster size.

3.3 The cluster source

The cluster source used here was built by Simon Marburger and is described in great detail in his thesis: [118]. In principle, it is a system which allows a gas mixture to be injected into the expansion chamber. The most important working parameters are:

1. The nozzle temperature: by controlling the flow of liquid nitrogen or helium and using a regulated heater², the temperature of the nozzle can be kept in the range of 30 to 300 K with an uncertainty of the temperature measurement of about $\pm 1 K$. The temperature of the nozzle might drift and the flow of the cooling liquid has to be kept under constant surveillance. This drift increases the uncertainty of the nozzle temperature to about $\pm 2 K$ for measurements longer than twenty minutes.
2. The expansion pressure: the expansion pressure is measured using a piezo-resistive manometer³ with an uncertainty smaller than 0.01 bar at room temperature.
3. The cluster source is mounted on an xyz-stage. Before measurements, the position of the source was adjusted. A first step was to maximize the countrate of photoelectrons. In a second step, the position was changed such that the ratio of cluster to monomer signals (compare 2.5) was maximized at constant expansion parameters.
4. The nozzle geometry: all experiments described here used a conical nozzle with opening diameter of $d = 80 \mu m$, half opening angle $\alpha = 15^\circ$ and cone length $t = 275 \mu m$. A sketch of the nozzle is shown in figure 3.4.

For homogeneous cluster production, a high-pressure gas bottle was connected to the cluster source via a leak valve. For inhomogeneous clusters, a gas mixture was prepared by filling two separated volumes of about 1 l each with the desired partial pressures of

¹ Varian V1000 HT, Agilent Technologies, Alsfelder Straße 6, 64289 Darmstadt, Germany

² SI 9500, Scientific instruments, Inc. 4400 West Tiffany Drive, West Palm Beach, FL 33407, USA

³ PAA-33X, Keller Ges. für Druckmesstechnik mbH, 79798 Jestetten, Germany

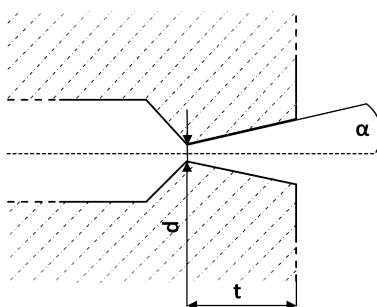


Figure 3.4: Sketch of the nozzle used in the experiments.

the gaseous components. To produce a 5 % mixture of Ar-Xe clusters, for example, the first volume was filled with argon gas at a pressure of 15 bar and the second volume with xenon gas at a pressure of 0.75 bar. After the filling, both volumes were connected and the resulting gas mixture was fed into the cluster source via a leak valve.

This method results in a well-defined mixing ratio at the beginning of the measurement. However, the condensation properties of the gases may differ and, in time, the mixing ratio will shift towards the gas with a lower condensation probability. To determine the mixing ratio in the resulting cluster, one must measure it. In some cases, mass spectrometry may be a suitable tool if fragmentation effects do not play a role or are understood completely. Another approach might be suitable in the near future: using single-shot single-particle x-ray diffraction at light sources like FLASH, a diffraction pattern of a single, but large cluster could be made [119]. To be able to draw conclusions about the mixing ratio of the clusters, we must examine the photoelectron spectra. Effects from surface, interface and bulk sites can be taken into consideration along the partial cross sections of the respective species. When applicable, the composition of heterogeneous clusters will be discussed in the respective chapters.

3.4 The magnetic bottle electron spectrometer

A magnetic bottle type electron spectrometer was first introduced by Kruit and Read [120]. In principle, it is a time-of-flight (TOF) spectrometer with an increased acceptance angle of up to 4π . The high acceptance angle is achieved by guiding electrons, initially emitted according to equation 2.17, into one specific direction. This is achieved using magnetic fields: a strong inhomogeneous field B_i in the interaction region, and a weaker, homogeneous field, the so called *guiding field* B_g , along the drifttube. While Kruit and Read used a strong electromagnet to produce B_i , it was later shown that a strong permanent magnet is also sufficient [121].

The working principle of a magnetic bottle is outlined theoretically in references [120] and [121]. Electrons which move in a magnetic field in such a way that the strength of the magnetic field is much greater than the change of magnetic field strength during one full spiral motion of the electron are called *adiabatic electrons*. For adiabatic electrons, both the torsional moment L and the total kinetic energy E are conserved quantities. In a magnetic field the electron kinetic energy can be divided into an axial part along the magnetic field lines and a cyclotron energy: $E = E_z + E_c$. The angular momentum thus is: $L = 2m_e E_c / qB$. Electrons traveling in a diverging part of the magnetic field thus transform E_c into E_z and are parallelized. Thus, Kruit and Read termed their apparatus "Magnetic field parallelizer."

3.4.1 Layout

The mechanical construction of the magnetic bottle electron spectrometer used in this work is described in the PhD thesis of Melanie Mucke [11], in which detailed drawings can be found. In short, it consists of a strong permanent-magnetic tip which is movable using an xyz-stage. The tip itself is a frustum of a cone made of soft-iron¹ sitting on a stack of three permanent magnets², each with a diameter of 10 mm and a height of 10 mm. The smaller surface of the truncated cone has a diameter of 3.1 mm. The magnetic field strength in the spectrometer's symmetry axis was measured as $B_{iz} = 0.189 \text{ T}$ at a distance of 2 mm from the cone's surface. The guiding field was generated using a coil of copper wire wound around the drift tube on the air-side of the vacuum system. The coil has a length of 600 mm and approximately 270 windings. This results in a field strength of about 0.5 mT at an applied current of 1 A. To shield the drifttube region from external magnetic fields, two layers of μ -metal were wrapped around the coil.

The drift tube has a length of 600 mm and is terminated by a copper mesh on the MCP-detector side and by an aperture of 25 mm on the side facing the interaction region. The interaction region is 55 mm away from the aperture. A schematic of the bottle is shown in figure 3.5. A static electric potential can be applied independently to the drifttube, the aperture or the magnetic tip. The detector itself is a Chevron-type [122] MCP double stack with a phosphor screen (P43)³ with an effective area diameter of 42 mm and an opening area ratio of 60 %. During operation, voltages of approximately 2200 V and 200 V were applied to the back and the front sides of the detector, respectively.

¹ Vacoflux50, Vacuumschmelze GmbH, Grüner Weg 37, 63450 Hanau, Germany

² $\text{Sm}_2\text{Co}_{17}$, IBS Magnet, Kurfürstenstraße 92, 12105 Berlin, Germany

³ F2225-21P, Hamamatsu Photonics Deutschland GmbH, Arzbergerstraße 10, 82211 Herrsching, Germany

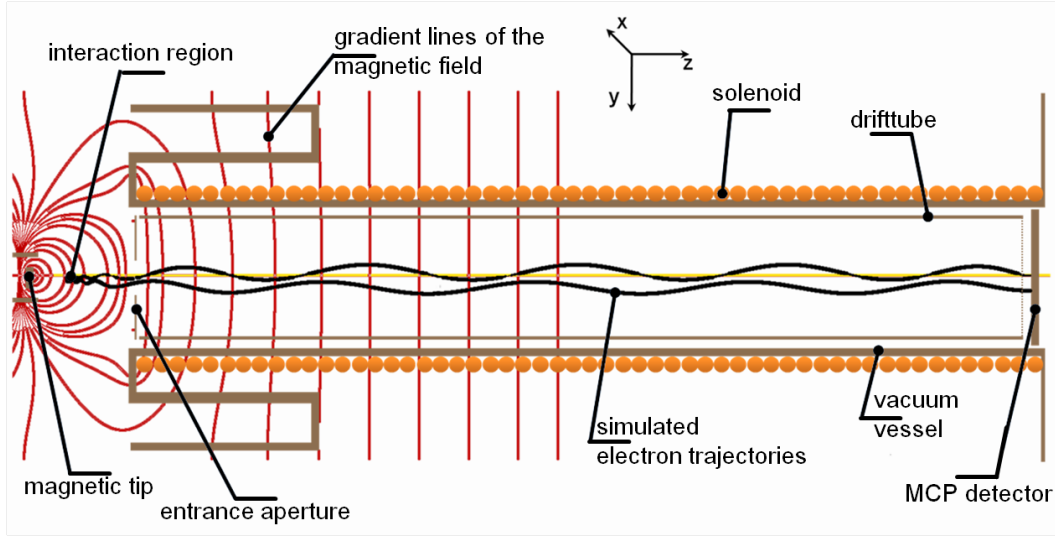


Figure 3.5: Schematic of the electron time-of-flight spectrometer including some equipotential lines of the magnetic field and two simulated electron trajectories. The distance between the interaction region and the MCP-detector is 655 mm.

The anode (i.e. the phosphor screen) behind the MCP stack was kept at a potential of approximately 3000 V during normal operation. For calibration purposes, this voltage was increased to values of approximately 3800 V.

3.4.2 Energy resolution and transmission

The key features of the magnetic bottle spectrometer are its high transmission at a wide range of electron energies, its good energy resolution and its ability to collect electrons in a solid angle of almost 4π . Figure 3.6 shows the experimentally determined energy resolution of the spectrometer in a range from 0 to 12 eV. The plot shows peakwidths of the He $1s$ and the Ar $3p_{3/2}$ lines (circles) determined using Gaussian fits. The observed widths result from a combination of the analyzer resolution and the monochromator broadening. Both values are *a priori* unknown. However, they can be determined by measuring a series of linewidths at equal kinetic energies but differing excitation energies: the total broadening can be assumed as $w = \sqrt{w_m^2 + w_a^2}$, with $w_{m,a}$ the broadening of the monochromator and the analyzer, respectively. If one further assumes that $h\nu/w_m(h\nu) = \text{const.}$ and that w_a is constant at every fixed kinetic energy, the constant and thus $w_m(h\nu)$ can be determined [17]. The resulting monochromator broadening was thus calculated as $h\nu/w_m(h\nu) \approx 240$ [17]. The data points were corrected for this energy-dependent monochromator broadening and are

included in figure 3.6 using crosses and stars. A dashed line in the figure shows a theoretical curve expected from a spectrometer with a resolving power of $E/\Delta E = 30$. It can be seen that the energy resolution is a constant of approximately $E/\Delta E = 28$ and is limited at very low kinetic energies by the monochromator broadening.

An increase in resolving power can be achieved by retardation of the electrons. However, the experiments described here rely on the detection of electrons with kinetic energies close to zero. A retardation is, therefore, not suitable and its effects will not be discussed here.

Of great importance, however, are the transmission properties of the spectrometer. Figure 3.7 shows a measurement of peak areas of the Ar $3p_{3/2}$ and Ar $3p_{1/2}$ lines, each normalized for its ionization cross section, the photon flux and the ring current. The relative transmission measured is almost constant over the energy range from about 0.9 eV to 5 eV. A slight increase is seen for energies below 0.9 eV. A measurement of the absolute transmission function of the spectrometer would require qualitative knowledge of the amount of electrons created per photon pulse. However, the amount of particles in the interaction region can only be estimated roughly. Another way to estimate the total detection efficiency is by analyzing coincident photoelectron-Auger electron spectra. By dividing the number of measured coincidences by the number of measured photoelectrons of xenon NOO Auger spectra, the total detection efficiency was estimated to be between 24 % and 50 % [17]. The total detection efficiency includes the detection efficiency of the MCPs, which depends on the open area of the MCP and the applied voltage, and can be up to 80 % at high voltages [123].

3.4.3 Simulations

To better understand the electron spectra produced with the magnetic bottle, the computer program *SIMION* [124] was used to simulate the electron trajectories and TOFs within a magnetic bottle. *SIMION* models electrostatic fields "as boundary value problem solutions of an elliptical partial differential equation called the Laplace equation" [125]. A three dimensional model of the magnetic bottle was made using its cylindrical symmetry. The potential arrays which serve as electrodes are the drift tube, the aperture, the magnet and the detector. Additionally, to simulate the magnetic field, four magnetic poles were introduced in such a way that the resulting magnetic field reflects the actual measured magnetic field. We measured deviations from a cylindrical symmetry in the real field but, for simplicity's sake, these were not taken into consideration in the simulations. Surfaces of equal magnetic field strength are shown in the figure on the first page of this thesis and in figure 3.5. The magnetic field lines can be drawn perpendicularly to these surfaces. Electrostatic potentials and magnetic field strengths can be applied to these electrode and magnetic arrays. *SIMION* can then calculate charged particle

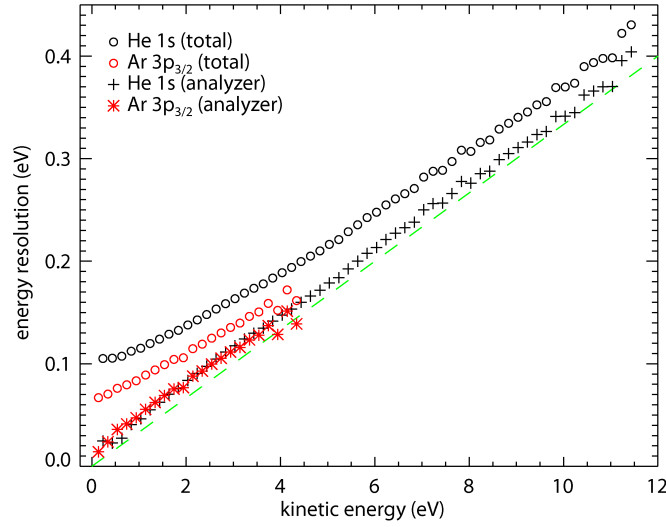


Figure 3.6: Energy resolution (FWHM) of the magnetic bottle spectrometer as a function of kinetic energy. Measurements of the atomic He $1s$ and Ar $3p_{3/2}$ photoelectron lines were analyzed. Points represented by circles show the apparatus broadening. The *plus* and *star* symbols show values after subtraction of an approximate monochromator broadening (see text for details). For comparison, the dashed line shows the broadening for a spectrometer with a resolving power of $E_{kin}/\Delta E_{kin} = 30$. Reprinted with permission from [17]. Copyright 2012, American Institute of Physics.

trajectories in the resulting electromagnetic field. In addition to the electromagnetic field, it is important to simulate the starting conditions of the electrons as realistically as possible. To obtain information on the transmission and energy resolution of the spectrometer, we must consider the size and shape of the interaction region, the energy resolution of the electrons and the angle resolved cross section.

The kinetic energy distribution follows a Gaussian distribution with a FWHM of the monochromator broadening. The start position was chosen as a 3-dim Gaussian distribution around the interaction region with a FWHM based on the overlap of the synchrotron beam and the cluster beam.

The probability of emission into a solid angle element is given by equation 2.17 and is dependent on the β parameter and the angle between the polarization axis and the direction of the electron emission θ . All measurements and simulations described here were made using linearly polarized light with the polarization vector perpendicular to the symmetry axis of the spectrometer (z-axis as defined in figure 3.5). The starting direction distribution can be expressed by the number of electrons emitted into a spherical segment. For each elevation angle Θ a number of starting electrons per

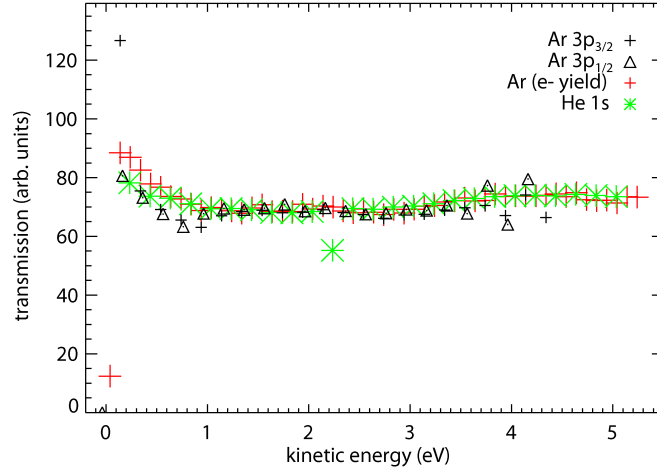


Figure 3.7: Intensity of the Ar $3p_{3/2}$ and $3p_{1/2}$ photoelectron lines normalized to the ionization cross section, ring current and the flux curve of the beamline. Resulting values reflect the kinetic energy dependence of the spectrometer transmission function on an arbitrary scale. The lowest Ar $3p_{3/2}$ data point ($E_{kin} = 0.12\text{eV}$) is probably influenced by autoionization of Ar $3p_{3/2}^{-1}nl$ Rydberg states. For comparison, values from a total electron yield measurement of Ar and from measuring the He $1s$ photoelectron line are shown. The latter two data sets were arbitrarily scaled to the average value of the Ar $3p_{3/2}$ data. Reprinted with permission from [17]. Copyright 2012, American Institute of Physics.

azimuthal angle Φ was calculated according to equation 3.8:

$$N(\Theta) = 1 + \left(0.5 - \frac{\beta}{4} + \left(\frac{3\beta}{4}\right) \cos^2(\Theta)\right) |\sin(\Theta)| * Z \quad (3.8)$$

Here, Z is a number which scales the total amount of traces. It was chosen such that each simulation included approximately 100000 electron traces. The N calculated according to equation 3.8 is thus the number of electrons starting into the sphere segment defined by $0^\circ \dots \Phi \dots 359^\circ$ and Θ . The term $|\sin(\Theta)|$ corrects for the area per angle element expressed in polar coordinates.

Figure 3.8 compares a He $1s$ spectrum, measured at 29.6 eV with an acceleration voltage of 1.1 V, to simulated spectra. The beta parameter for He $1s$ photoemission is two. The energy broadening in the simulation was set to a FWHM of 25 meV. The 3-dim Gaussian FWHM of the interaction region was set to $(0.2, 3, 0.2)\text{mm}$ in the x, y and z directions, respectively (dashed line), and to a point-like interaction region (dash-dotted line). For each simulated spectrum, 100,000 electron trajectories were calculated. Additionally, a simulation was made in which electrons were only emitted into the solid angle 2π facing the aperture, a situation described by Kruit and Read

[120].

As can be seen from figure 3.8, the simulations are in agreement with the measured spectrum. The total time of flight, the energy resolution and the spectral shape can be simulated. The simulations clearly show that the parallelization of the electrons is not instantaneous, but rather the main factor broadening their time-of-flight. The spectrum simulated by assuming a point-like interaction region shows no significant improvement with regards to the TOF broadening. When electron emission is only allowed within the hemisphere facing the spectrometer, the TOF broadening is halved.

Several simulations were made to find out more about the effect that the guiding field and the electron kinetic energy have on the transmission function of the spectrometer. With very small guiding fields (lower than 0.2 mT), the cyclotron radius for electrons with kinetic energies of, for example, 1 eV, is as large as the radius of the aperture of the magnetic bottle. This may lead to oscillations in the transmission vs. kinetic energy curve as reported in [11].

Another factor influencing the transmission is the size of the interaction region. A magnetic bottle has magnifying properties and electrons stemming from a non point-like source are projected onto the detector with a magnification defined by the ratio of the magnetic field strengths, $M = B_i/B_g$. This means that only electrons from an interaction region with a radius smaller than the radius of the aperture divided by M can reach the detector. This effect is also advantageous as it shields the detector from electrons stemming from outside that region.

Electrons emitted in the direction of the magnetic tip travel a certain distance before they are turned around. The velocity of an emitted electron can be separated into two parts: a component pointing directly from the point of electron creation towards the magnetic tip $v_{||}$ and a component perpendicular to the first one, v_{\perp} . The higher the ratio $v_{||}/v_{\perp}$ is, the further the electrons travel towards the tip. At a certain ratio, the electrons hit the tip and cannot be turned around anymore. This threshold ratio defines a solid angle under which electrons are not detectable. It is dependent on the ratio of the magnetic fields in the interaction region to the highest magnetic field reachable by the electrons. An analytical expression for this relationship is given in [126]:

$$\frac{|v_{||}|}{|v_{\perp}|} < (B_{max}/B_i)^{1/2} \quad (3.9)$$

Measured field strengths of $B_i = 190$ mT in the interaction region and $B_{max} = 0.38$ mT close to the magnetic tip result in a loss cone with a half opening angle of 45° . This causes the β parameter to have an influence on the transmission: with a β of -1 , 19.0 % of all emitted electrons are emitted into the loss cone, a β of 0 results in a loss of 14.6 % and a β of 2 results in a loss of 5.9 %.

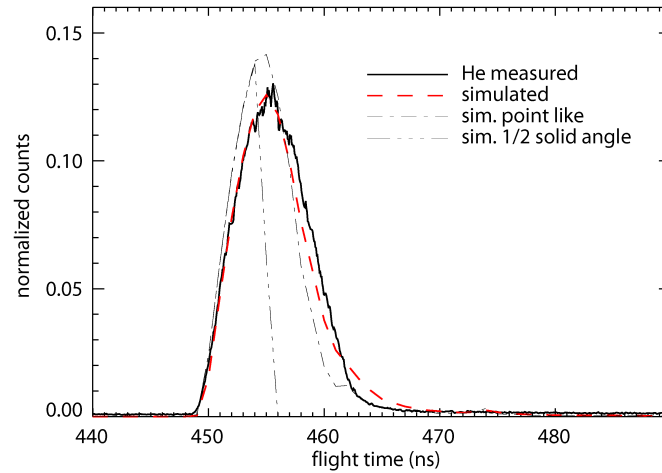


Figure 3.8: Comparison of a measured He $1s$ photoelectron spectrum and charged particle trajectory calculations. The kinetic energy was set at 5 eV and the acceleration voltage at 1.1 V. The solid black line and the dashed line are the measured and simulated spectra, respectively. The simulation includes the effect of a finite size of the interaction region, with 3 mm extension along a line perpendicular to the spectrometer's central axis and 0.2 mm diameter in the remaining two dimensions. The other two traces were simulated with the assumption of a point-like interaction region (dash-dotted line), and with the additional restriction of admitting electron emission only in the half sphere on the spectrometer side (dash-dot-dot-dot line). See the text for more details on the simulation.

3.4.4 Kinematic broadening

A spectrum of electrons stemming from a moving target is kinematically broadened. This broadening is in the range of a few meV for atoms at room temperature. For fast-moving electron sources, this broadening can become larger than the instrumental energy resolution. The kinetic energy of an atom at room temperature is approximately 0.04 eV. The velocity of the atom then depends on its mass. If, at room temperature, a moving argon atom with a mass of 40 amu emits an electron, this results in a kinematic broadening of approximately 0.001 eV. If the argon atom is traveling with a kinetic energy of 500 eV this broadening is approximately 1 eV. This means an electron emitted in the moving direction will be observed with a kinetic energy of 1 eV higher than an electron emitted in the opposite direction.

This effect is generally considered to be disadvantageous. Domesle *et al.* however showed that this effect can be used to directly determine the β -parameter of the emission of photoelectrons by comparing the shape of broadened spectra to simulations [12, 13]. The electron detachment process was measured on anions in a beam with a kinetic energy of 4000 eV using the same magnetic bottle as described here.

3.5 Data recording and processing

The actual quantity recorded in the experiments described here is the time difference between a trigger signal, called *bunchmarker*, delivered by BESSY and the arrival of an electron at the MCP-stack. The time difference between the bunchmarker and the arrival time of the photon bunch in the interaction region is fixed. Thus, it is possible to calculate the time required for an electron to travel, after its production, from the interaction region to the detector. Using a combination of data fitting routines and calibration points, this time of flight can be converted to the kinetic energy or to the binding energy of the electron. Some important details about the data collection and treatment will be outlined in the next sections.

3.5.1 Data recording

An electron which hits the MCP results in a cascade of electrons leaving the MCP stack. These electrons are then accelerated onto an anode with a high potential. The small resulting change in voltage on both the anode and the MCP stack can be decoupled using a capacitor. This variation is then amplified¹ and discriminated by a constant fraction discriminator (CFD)². It is then transferred to a time-to-digital converter (TDC)³. The TDC is multi-hit capable and has a bin width of 60 ps. The TDC measures the time between a start signal and the electron signal from the CFD. Here, multi-hit means that more than one electron arrival time can be measured between two start signals. Every second bunchmarker signal is used as a start signal. If one or more electrons are detected, their arrival times are stored in a unique group.

For clarification, the following terms will be used to describe the experiments and data analyses. A *hit* is a signal from the MCP. An *event* is the time-span between two consecutive start signals, whether it includes one hit, or many hits. A *coincidence* is the measurement of more than one hit within one event. Two or more hits are called *coincident* if they are recorded within one event. Coincidences can be divided into *true* and *random* coincidences. True coincidences stem from a physical process which leads to the emission of more than one electron. Random coincidences stem from different physical processes which may occur at the same time but are independent from each other.

¹ HVA-500M-20-B Voltage Amplifier, FEMTO Messtechnik GmbH, Paul-Lincke-Ufer 34, 10999 Berlin, Germany

² CF4000 quad, EG G Ortec: AMTEK GmbH, Rudolf Diesel Straße 16, 40670 Meerbusch, Germany

³ GPTA mbH, Dülmener Pfad 5, 13507 Berlin, Germany

Hits with a time difference of less than 25 ns cannot be distinguished from one another due to the pulse pair resolution limit of the CFD. This means that a coincidence cannot be measured between two electrons arriving within a time interval of 25 ns. For example, two electrons with a kinetic energy of 1.0 eV and 1.14 eV, or of 10 eV and 11.88 eV, have a time of flight difference of approximately 25 ns (assuming an acceleration voltage of 1 V).

3.5.2 Signal processing

The recorded data can be assessed and visualized in different ways. For example, a simple time-of-flight spectrum shows the histogrammed TOFs of all hits in all selected events. A TOF spectrum of two electron coincidences, for example, can show the histogrammed TOFs of all hits from only those events which have exactly two hits.

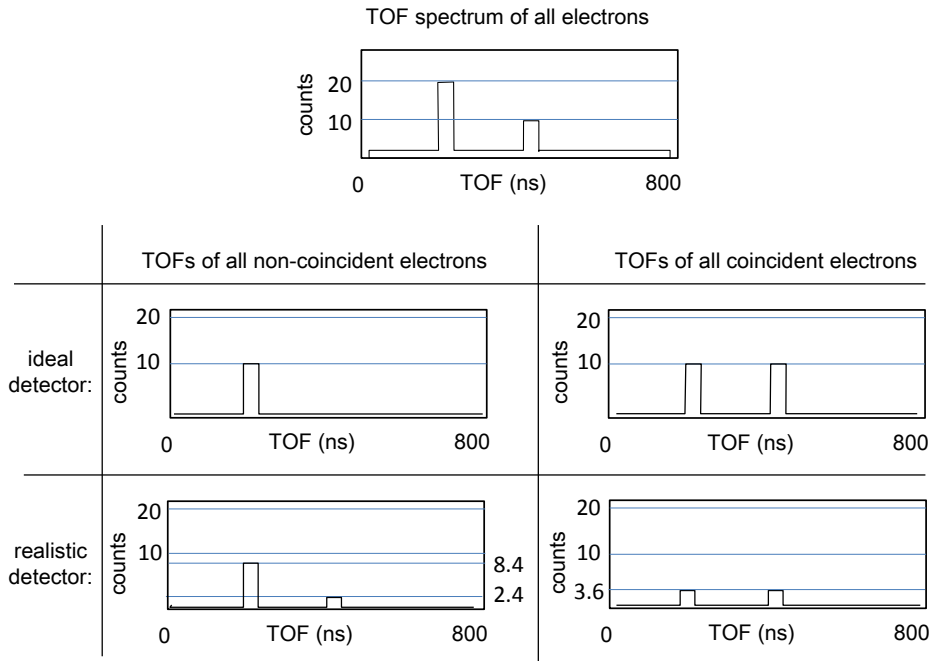


Figure 3.9: Sketches of one dimensional TOF spectra to illustrate the coincidence analysis of the recorded data. Details are explained in the text.

Figure 3.9 shows a sketch of a TOF spectrum which is separated into a part where only events with one hit are shown and a part where only events with two hits are shown. The TOF spectrum of all electrons has two features. A strong feature with 20 counts and a weak feature with 10 counts. Let us assume that direct photoionization

leads to the strong feature and that the created vacancy autoionizes in 50 % of the cases giving rise to the weak feature. The other 50 % decay via the emission of a photon, which cannot be detected. Let us further assume that the TOF recorder has a constant transmission function for all TOFs and a detection efficiency of 100 % (ideal detector). A selection of all hits with only one event then gives rise to the TOF spectrum of all non-coincident electrons. A selection of all hits with exactly two events gives rise to the TOF spectrum of all coincident electrons. This shows that a selection between events with one and with two electrons allows conclusions about the participating decay channels. In reality a detection efficiency of 100 % cannot be achieved. If we assume a detection efficiency of, for example, 60 %, the spectra change. This is shown in figure 3.9 in the *realistic detector* row. The total number of all recorded electrons is now reduced by a factor of 0.6. Intensity is seen in the non-coincident spectra even from secondary electrons. This is because their partner is not detected and thus they are categorized as non-coincident. The intensities of both contributions in the coincident spectrum are still equal. However, they are reduced by a factor of $0.6 * 0.6$ compared to the coincident spectrum of the ideal detector.

In this work I will present coincident data also in the form of coincident maps. In these maps, the distribution function of the times-of-flight (or energies) of electron one vs. those of electron two are drawn as a color-coded event histogram. If the electron TOF spectrum is complicated and includes many contributions, such a map helps to identify regions in the TOF spectrum which stem from coincident electrons. A coincident map of the situation described in figure 3.9 is sketched in figure 3.10.

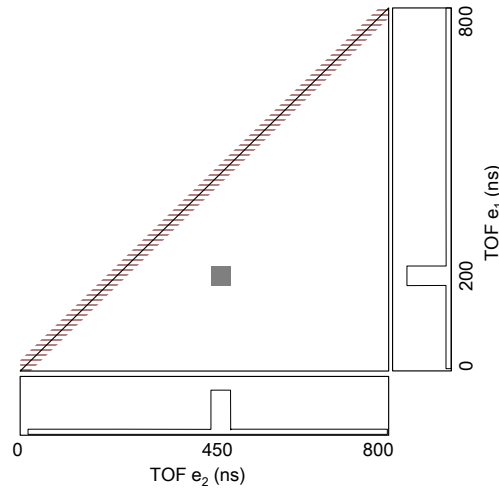


Figure 3.10: A sketch of a coincidence map. It is intended to illustrate the analysis and the display of coincident data. Details are explained in the text.

The shown coincident map is again an idealized case, assuming a 100 % detection efficiency and no random coincidences from background signals. The axis of the shown map represent TOFs of electrons. A histogram is made of the TOFs of all coincidences. Each pair of electrons pertains to one count in the respective TOF*TOF interval of the coincidence map. The result can, for example, be drawn in a color-coded map. Different colors represent a different number of counts in the respective TOF*TOF interval. In our case, the resulting coincidence signal is drawn in gray. A summation along one of the TOF axis of the map leads to the spectra shown on the right hand side and below the coincidence map. The sum of these two spectra equals the spectra shown in figure 3.9 (ideal detector, all coincident electrons). This is very interesting, because it illustrates how the use of coincidences can easily disentangle the spectrum of all electrons into the TOF spectra of the underlying processes. The striped area shows the part of the coincidence map which is not accessible, because the TOF difference of the electron pairs which are found in that area is smaller than the double pulse resolution of the CFD.

As mentioned before, the measured quantity in the experiments is the electrons TOF. To present the data in the energy domain, it has to be converted. In principle, this works by measuring the TOFs of set of spectra with known kinetic energies. The resulting time to energy relation can then be used to transform spectra of unknown kinetic energy. Such a time to energy relation was made for each used parameter set of the magnetic bottle.

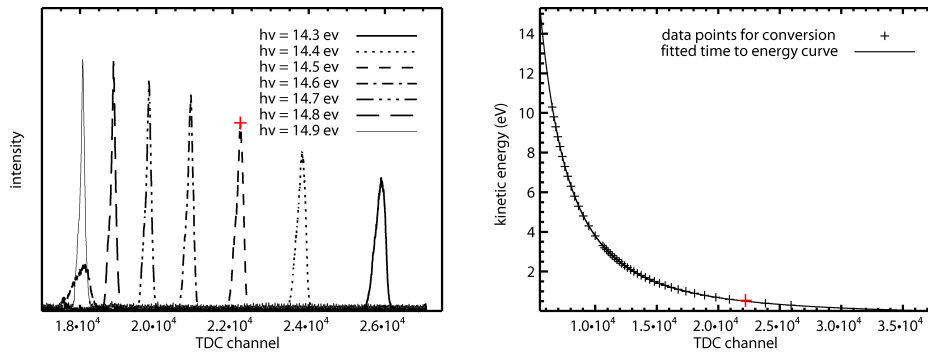


Figure 3.11: TOF spectra of krypton excited at different energies (left panel) and a resulting channel to energy conversion table (right panel).

Figures 3.11 and 3.12 illustrate the conversion procedure. Here a set of Kr 4d spectra with known kinetic energies was measured. The left panel in figure 3.11 shows a small section of the measured spectra. The ionization potential of the Kr 4d_{3/2} line is 14.0 eV. The peak marked with a red plus sign thus pertains to a kinetic energy of 0.5 eV at the

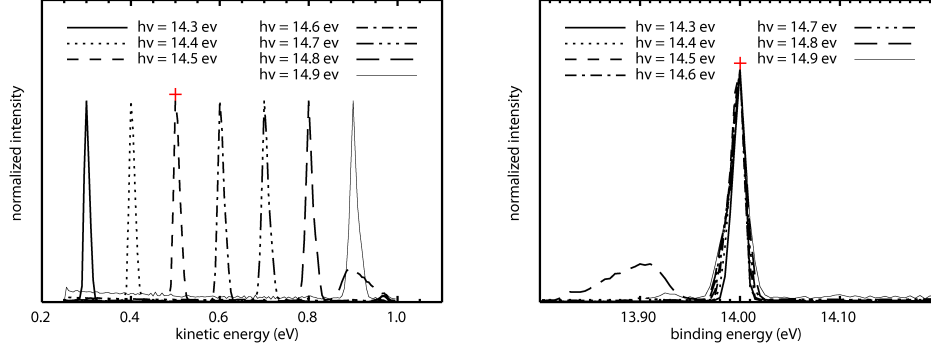


Figure 3.12: Resulting time to energy converted spectra plotted over electron kinetic energy (left panel) and binding energy (right panel). As the same spectra are shown which have been used to obtain the time to energy relation, no new information is included here. The figures are shown merely to illustrate the conversion and the presentation of data in means of binding energy or kinetic energy.

channel with the number 22201. The right panel shows a plot of all measured channel to kinetic energy points. The solid line is a fit of this data. The fitting routine is based on the geometry and the applied potentials of the magnetic bottle:

$$t(E_{kin}) = t_0 + \frac{s_1}{\sqrt{\frac{2(E_{kin}-qU_1)}{m_e}}} + \frac{s_2}{\sqrt{\frac{2(E_{kin}-qU_2)}{m_e}}} \quad (3.10)$$

Here, the resulting fit parameters are t_0 , which corresponds to the time zero position of the spectrum and U_1 and U_2 , the potentials which are applied at the two different sections of the drifttube. The lengths of these sections are given by s_1 and s_1 . q is the electron charge and m_e the electron mass. For all n pairs of time (t_k) and energy ($E_{kin,k}$), found by measuring electron spectra of known energy, the parameters are determined such that the sum of all n pairs of $(t(E_{kin,k}) - t_k)^2$ is minimal. This procedure results in a time to energy table which can be extrapolated to kinetic energy values for which no supporting points exist. Both the time zero position and the potentials at the different sections of the drifttube are usually known. A fit of these parameters is nevertheless necessary due to inhomogeneities in the actual electrostatic field. The result of this fit is a table which connects the channel number (time) to the corresponding kinetic energy of the electrons. Spectra can now be drawn in the energy domain using this table. Figure 3.12 shows the resulting spectra plotted over kinetic energy and over binding energy. Both, spectra in the kinetic energy domain and in the binding energy domain are shown in this thesis. Figure 3.12 contains no

new information about the shown spectra but merely illustrates the conversion. The coincidence maps shown in this work are converted in a similar way. A histogram is made of electron pairs in kinetic energy intervals ($E_{kin}(e_1) * E_{kin}(e_2)$). Such a converted map is shown in figure 3.13. All coincidence maps in this work are drawn

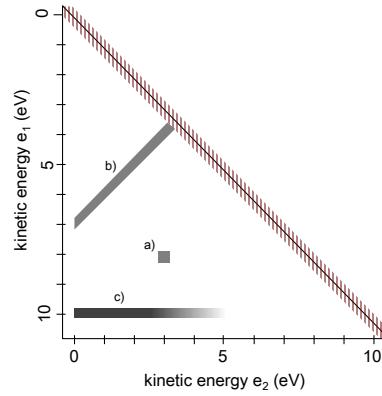


Figure 3.13: Schematic of a time-to-energy converted coincident map. Three different features are included to illustrate different physical process. Note that the electron energy axis are drawn differently from those shown in aforementioned maps. Details are explained in the text.

in this way. I have included three different exemplary features. Feature a) shows a coincidence of two electrons, where the first one has a kinetic energy of 8.2 eV and the second a kinetic energy of 3 eV. A signal like this could be caused by recording the NOO Auger decay of xenon at an excitation energy of approximately 72.5 eV [127]. Here, e_1 then corresponds to one of the Auger lines and e_2 to the photoelectron. Case b) stems from a physical process, where the sum of the kinetic energies of the first and the second electron is a constant. Such a process is, for example, electron-electron scattering. Signal c) stems from a process where the energy of the first electron is at a fixed value while the kinetic energy of the second electrons shows a broad distribution. ICD of water clusters could be such a process [8]. The first electron is the photoelectron from an inner valence orbital of a water molecule in a water cluster. Its kinetic energy depends on the excitation energy. The second electron stems from autoionization of an outer valence orbital which is broadened in the cluster. These examples show how different processes can be differentiated using a coincidence map.

The ionization potentials for argon and krypton used for the time-to-energy calibration are given in table 2.3, the ionization potential of helium is 24.59 eV[79]. The uncertainty of the conversion depends mainly on the uncertainty of the excitation energy as given in section 3.1.

4 Near-threshold outer-valence spectra of argon and krypton

In this chapter, I will present near-threshold outer-valence spectra of argon and krypton clusters of various mean sizes. One reason why these spectra are important in the context of this thesis is that understanding and interpreting them provides a tool for the interpretation of the valence spectra of mixed rare gas clusters. Both the widths and the positions of the valence bands will later be compared to those of mixed clusters.

Another reason is that they show unique and interesting properties of their own when measured close to the photoionization threshold.

One of the most interesting questions in cluster physics is, at which size do the clusters become bulk-like? In other words, how large must a cluster be in order to develop characteristics that are observed in the bulk material.

The dispersion of an energy band is an important signature of bulk electronic properties. Dispersion occurs when a system shows sufficient long-range order. It can be observed as an excitation energy dependent or emission angle dependent shift in the photo-emission peak and is caused by crystal-momentum conserving optical transitions.

The spectra presented here show a pronounced feature whose binding energy shifts with the excitation energy. This feature is superimposed on the broad, well-known Ar $3p$ derived band and the Kr $4p$ derived cluster band. These dispersing features are known from photo emission spectra from (111)-oriented single crystals [128] and polycrystalline films [69] and, in the case of argon, were discussed in terms of dispersion of the valence band [129].

If the observed dispersing feature is indeed caused by band dispersion, then the question arises, how large do the clusters have to be in order to show this feature? The data presented shows that argon clusters with a size of approximately 230 atoms already show bulk-like behavior. This is very interesting, because clusters with that size still have more atoms on the surface than in the bulk.

The argon data presented here is an expanded version of earlier publications [130] and [131]. The discussion is based on these papers. The argon data was recorded at TGM 4. The krypton data was measured at UE112.

4.1 Electronic band dispersion in argon clusters.

Figure 4.1 shows high-resolution Ar $3p$ photoelectron spectra of clusters with a mean size according to Hagenas' scaling law of $\langle N \rangle = 1670$. They were measured at an earlier experiment at the UE112/lowE PGMA beamline at BESSY II using horizontally linearly polarized light. This data set was also used in discussing the argon band structure in an earlier paper [130]. Details regarding this experiment can be found in [70], so only a brief outline will be given here. Clusters were produced via supersonic expansion of argon through a nitrogen cooled nozzle. The vacuum chamber is separated in three parts which are pumped individually: a differentially pumped section which connects the main chamber to the beamline and which provides a sufficient gradient in pressure between those two volumina, an expansion chamber which holds the cluster source, and the main chamber which holds the electron detector. The expansion chamber and the main chamber were separated by a conical skimmer. The electron detector was a hemispherical analyzer ¹, mounted in the dipole plane under the magic angle of 54.7° . The pass energy was set to 5 eV. The apparatus energy resolution was approximately 20 meV.

The spectra at high excitation energies resemble those reported previously [70, 73, 132, 133]. They consist of a largely unstructured valence band in the binding energy range between 14.1 eV to 15.6 eV. It has been discussed that this band is the result of spin-orbit splitting and additional splitting of the $3p_{3/2}$ band into its magnetic sub-levels $m_j = \pm 3/2, \pm 1/2$ due to crystal field splitting [134]. This means that the broad feature contains six component peaks. Rolles *et al.* were able to perform fits containing six peaks on the $5p$ derived cluster band of xenon [133]. They also have made such plots for argon and krypton, but remark that such fits are not as straightforward, due to the much smaller spin-orbit splitting.

In addition to that cluster band, at excitation energies in the range between 15.9 eV to 17.5 eV, a second feature is visible. This peak has a FWHM of approximately 0.25 eV and shifts smoothly in binding energy from 14.6 eV to 15.1 eV in this excitation energy range. It can be seen in panel a) of figure 4.1 that at 16.9 eV, this peak strongly dominates the spectrum.

The green line in figure 4.1 connects the maximum positions of the dispersing feature in our measurement. Asterisks in the figure represent maximum positions of measurements by Kassühlke [128] and Schwentner *et al.* [69]. They also show the maximal range of excitation energies in which this feature was present in those earlier experiments.

¹ SES ES200, VG Scienta AB, Vallongatan 1, SE-752 28, Uppsala, Sweden

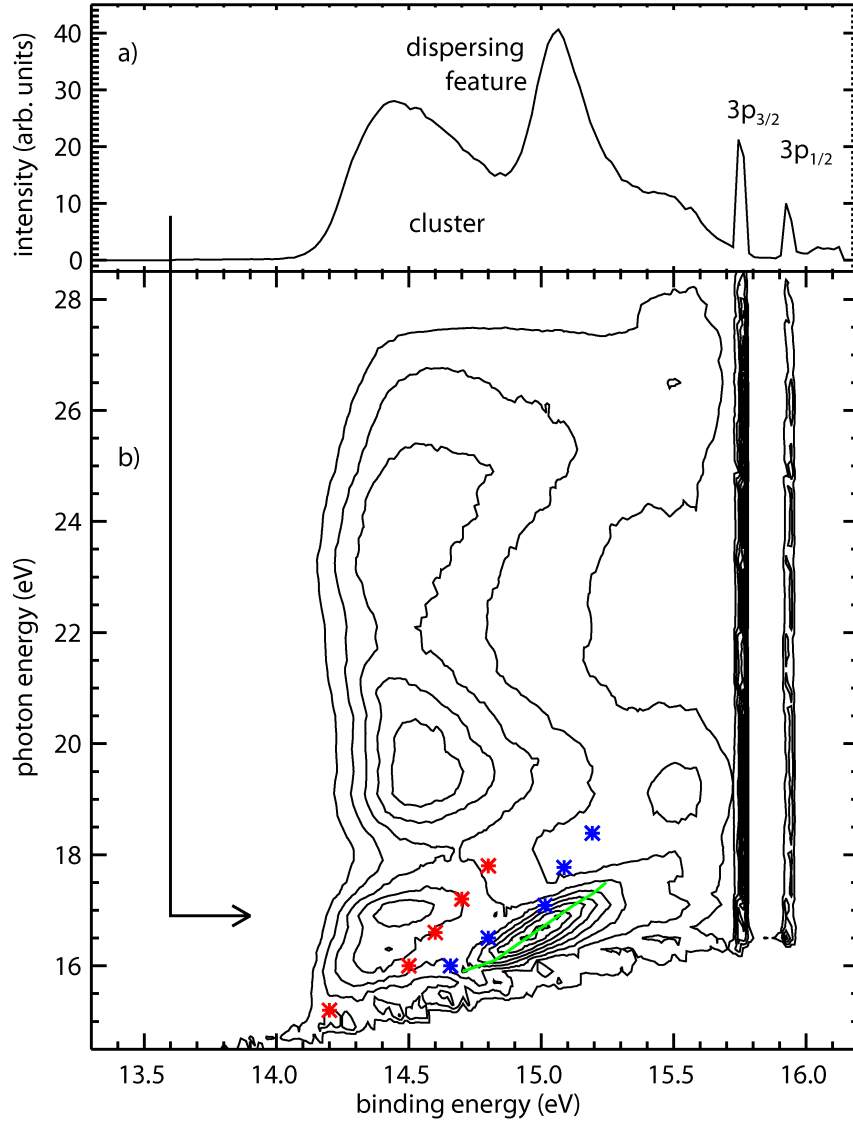


Figure 4.1: (a) Single scan high-resolution Ar 3p photoelectron spectra of clusters with a mean size of $\langle N \rangle = 1670$ at an excitation energy of 16.9 eV. Panel (b) shows the complete data set as a contour plot. The green line connects the maxima of the measured dispersing feature. The red asterisks represent data measured by Kassühlke *et al.* on an (111) argon multilayer [128] and the blue asterisks are extracted from energy distribution curves measured by Schwentner *et al.* on a polycrystalline film of argon [69]. The atomic Ar 3p_{1/2} and Ar 3p_{3/2} photoelectron lines seen in both panels stem from uncondensed argon in the cluster beam.

The photoemission data from Kassühlke are from a measurement of 25 layers of argon on a ruthenium substrate. Their measurements were made under grazing incidence of linearly polarized light. The electron detector was mounted to collect electrons emitted in the direction defined by the normal of the substrate's surface. The data from Schwentner *et al.* are from a thick polycrystalline argon film measured under normal incidence with an electron spectrometer also mounted normal to the sample. The maximum positions shown in figure 4.1 were extracted from figure 1 in [69]. Both datasets show a dispersing feature which dominates the whole spectrum. Both shift in binding energy by approximately 0.6 eV. By comparing their data to the theoretical work [135], Kassühlke comes to the conclusion that, in the case of bulk argon, the dispersing feature observed is the result of dispersion perpendicular to the (111) surface along the Γ -L direction of the *fcc*-lattice.

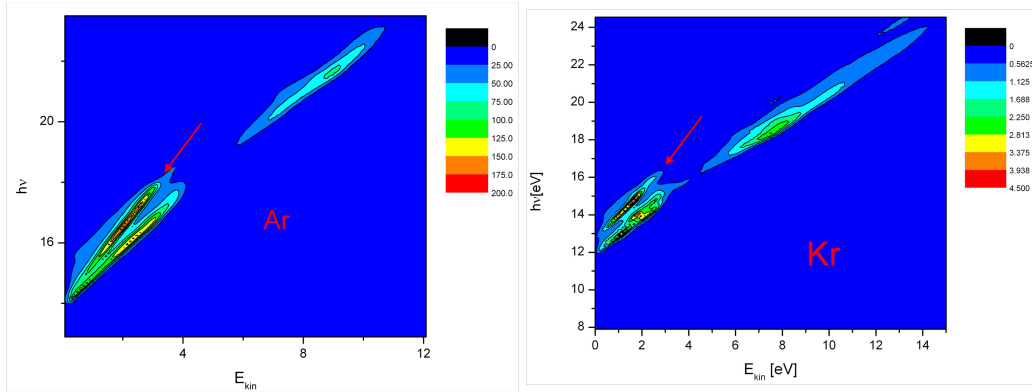


Figure 4.2: Color-coded contour plot of photoelectron spectra of an argon multilayer (left) and a krypton multilayer (right), taken from [136] and [128]. Red arrows mark the dispersing feature which was included in figures 4.1 and 4.7. The measurements are described in detail in [128]. Reprinted with permission from P. Feulner.

The slope of the dispersing cluster feature is almost identical to the slopes from the polycrystalline and the crystalline feature. The absolute positions of the polycrystalline feature and the cluster feature are separated by approximately 0.1 eV. The crystalline feature is separated from the cluster feature by approximately 0.6 eV.

The identical excitation energy range, the nearly identical slopes and binding energy positions and the fact that the dispersing features dominate the spectra are very strong indications that they originate from the same effect and can be attributed to energy band dispersion. This means that clusters with a mean size of $\langle N \rangle = 1670$ show bulk-like electronic properties. This is in agreement with expectations because at this cluster size, the number of atoms on the surface is smaller than the number of atoms in the bulk.

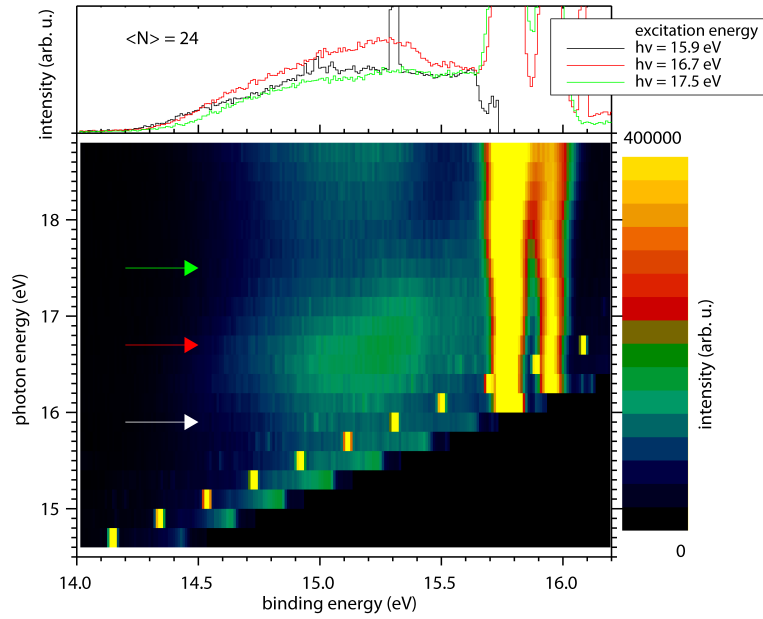


Figure 4.3: Color-coded intensity plot of the Ar 3p derived spectra of argon clusters with a mean size of $\langle N \rangle = 24$. The upper panel shows three photoemission spectra at selected excitation energies indicated by arrows of the respective colors. The spectra were recorded with the magnetic bottle spectrometer at TGM 4.

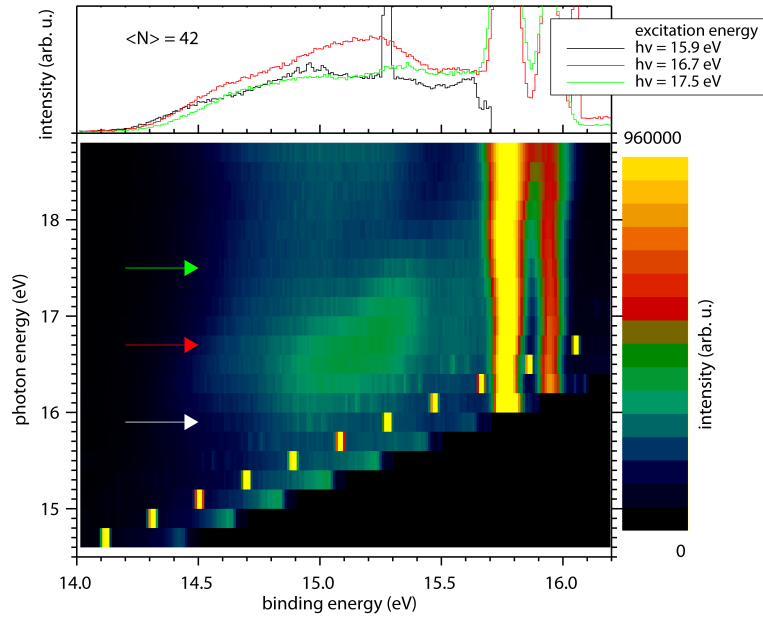


Figure 4.4: Color-coded intensity plot of the Ar 3p derived spectra of argon clusters with a mean size of $\langle N \rangle = 42$.

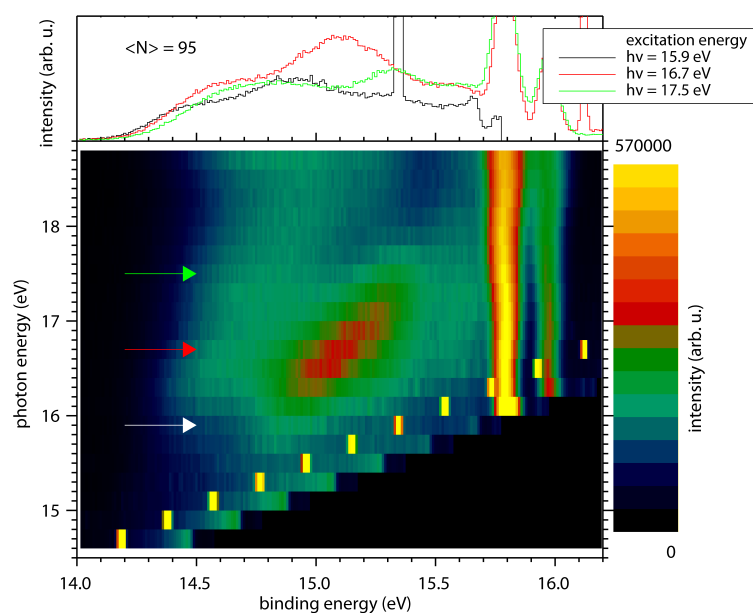


Figure 4.5: Color-coded intensity plot of the Ar $3p$ derived spectra of argon clusters with a mean size of $\langle N \rangle = 95$.

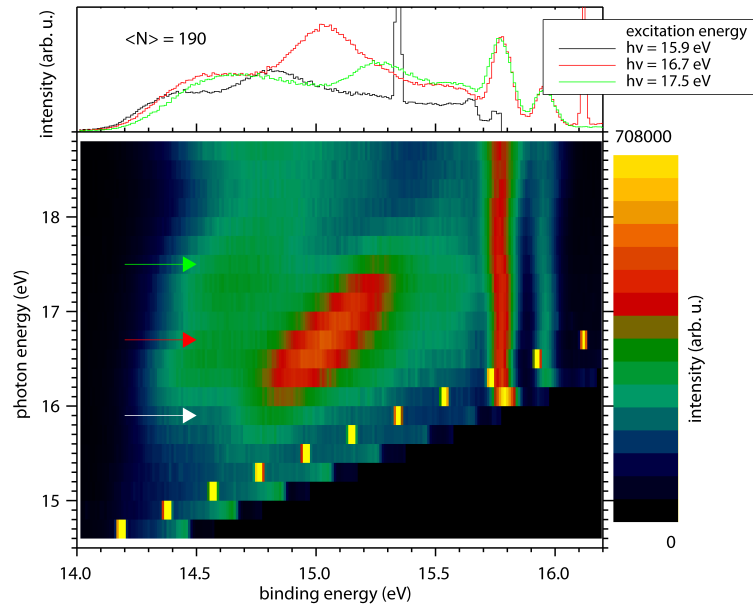


Figure 4.6: Color-coded intensity plot of the Ar $3p$ derived spectra of argon clusters with a mean size of $\langle N \rangle = 190$.

The observation of the dispersing feature is a more direct way to establish the onset of bulk-like behavior. Figures 4.3 to 4.6 show color-coded intensity plots of the Ar $3p$ derived cluster band in the excitation energy region of the dispersing feature. The mean cluster sizes of $\langle N \rangle = 24$, $\langle N \rangle = 42$, $\langle N \rangle = 95$ and $\langle N \rangle = 190$ were derived using the scaling law from Hagena. All plots show the Ar $3p_{1/2}$ and the Ar $3p_{3/2}$ monomer lines at their respective binding energies of 15.94 eV and 15.76 eV as vertical, intense features. The small deviations of the binding energy of these features are a result of imprecisions in the photon energy step of the monochromator of TGM 4 and the resulting uncertainty of the time-to-energy conversion. The energy resolution obtained is approximately $E/\Delta E = 20$. The energy resolution can directly be observed in the datasets by measuring the widths of the monomer peaks. The sharp peaks in the photon energy range of 14.7 eV to 16.7 eV are a result of second order radiation. In order to increase the energy resolution, the spectrometer was set such that the TOFs of the slow electrons exceeded 800 ns. The time difference between two subsequent pulses is 800 ns. This means that slow electrons are mapped into a TOF region that also may include fast electrons from the following photon bunch. The time-to-energy conversion, which uses a table made for electrons from first order radiation, then places fast electrons stemming from second order contributions at the wrong binding energies. The second order line is sharp and includes both contributions from the monomer and the cluster. This artifact can be seen in all four intensity plots and in the black and red single photoelectron spectra in the upper panels.

The upper panels in figures 4.3 to 4.6 show three selected single photoelectron spectra from the respective datasets. In each color plot, colored arrows mark the excitation energies of the spectra in the upper panels. The excitation energies were selected at points where the onsets of the dispersing features and the maximum intensities of the dispersing features are visible in the high resolution spectra of large clusters shown in figure 4.1.

The dispersing feature can be identified in the figures of the smallest cluster sizes. However, it is less intense than the background from the cluster valence band. The energy shift is smaller than that of the large clusters shown in figure 4.1. The shift is approximately 0.3 eV and 0.35 eV for clusters with a mean size of $\langle N \rangle = 24$ and $\langle N \rangle = 42$, respectively. The clusters with mean sizes of $\langle N \rangle = 95$ and $\langle N \rangle = 190$ both show a shift in binding energy of approximately 0.6 eV. This is as large as the shift observed in the high-resolution spectra of the large clusters. The clusters with a mean size of $\langle N \rangle = 190$ already closely resemble those shown in figure 4.1. The slope of the dispersing feature vs. binding energy, as well as the ratio of background to dispersing feature intensity, are comparable. The FWHM of the valence band increases with increasing cluster size. It ranges from approximately 1.2 eV for clusters with $\langle N \rangle = 24$ to approximately 1.5 eV for clusters with $\langle N \rangle = 190$. The width of the valence band

measured for bulk, polycrystalline argon is approximately 1.8 eV [69].

A more precise estimate of the clusters' size can be obtained by comparing bulk and surface contributions in spectra from the inner valence or core level photoelectron spectra. Therefore, in a separate experiment, we have measured Ar 3s photoelectron spectra at various expansion conditions using a Scienta analyzer. We determined the area ratios of the bulk-to-surface contributions. These ratios can be compared to theoretical ratios derived from a bulk-to-surface ratio of hypothetical clusters with a known structure (compare equations: 2.6 and 2.7). For clusters with mean sizes of $\langle N \rangle = 40, 90$ and 150 (according to the expansion conditions), we determined cluster sizes of $N_{ph} = 160, 200$, and 300 according to photoemission spectra, respectively. The agreement between cluster sizes derived from scaling law and photoemission spectra increases with increasing cluster size. An extrapolation of these measurements yields, for the clusters observed here, sizes of $N_{ph} = 230$ and 400 for $\langle N \rangle = 95$ and $\langle N \rangle = 190$, respectively.

The width of the size distribution in the cluster beam is large (compare figure 2.2). This means that, even in a cluster beam with a mean size of the clusters of $\langle N \rangle = 24$, a small fraction of large clusters is present. It must be assumed that this small fraction of large clusters is the reason why the dispersing feature is seen in the spectra of very small clusters.

4.2 Electronic band dispersion in krypton clusters.

Analogous to the argon measurements, we have measured krypton clusters close to their ionization threshold. Experiments by Schwentner *et al.* on polycrystalline, bulk krypton show a dispersing feature [69]. This feature is also present in measurements on ordered multilayers of krypton made by Kassühlke [137]. Unfortunately, the latter dataset has not been published. Their data shows two features in the excitation energy range of 12.0 eV to 16.5 eV: one broad feature with a constant binding energy of approximately 11.7 eV, and one dispersing feature which is visible in the excitation energy range of approximately 13.5 eV to 15.6 eV, where it dominates the spectrum.

Figure 4.7 shows a color-coded intensity plot of the Kr 4p derived cluster band at excitation energies in the excitation energy region of the dispersing feature. The measurements on krypton clusters were made at UE112 at BESSY II. The increased energy resolution in comparison with the argon measurements is reflected in the narrower width of the monomer lines. They can be seen at their binding energies of 14.0 eV and 14.67 eV. At excitation energies above 15.5 eV, the cluster band resembles those reported earlier (for example [133]). It is separated into the Kr 4p_{1/2} derived band at approximately 14.2 eV binding energy and the broader Kr 4p_{3/2} derived band with a

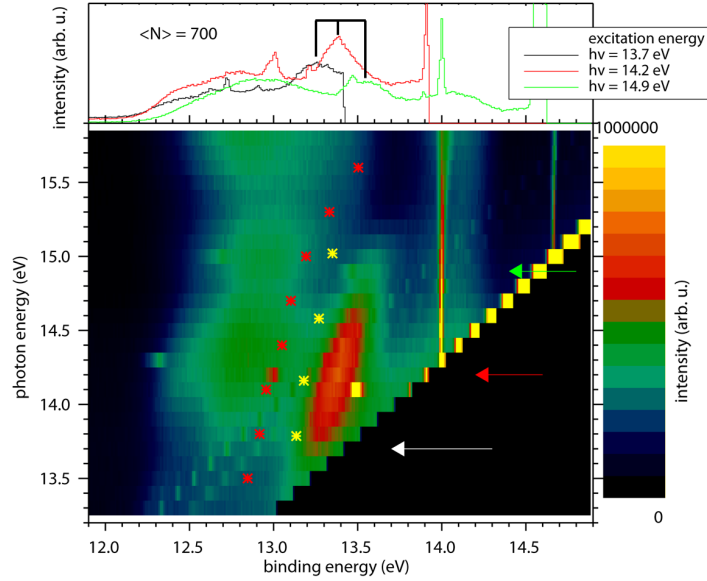


Figure 4.7: Color-coded intensity plot of the Kr 4p derived spectra of argon clusters with a mean size of $\langle N \rangle = 700$. The upper panel shows three photoemission spectra at selected excitation energies, as indicated by arrows of the respective colors in the map. Asterisks in red indicate the maxima of the dispersing feature in the spectra of an annealed krypton multilayer [137]; those in yellow, the maxima in the spectra of a polycrystalline film of krypton [69]. The maxima of the dispersing feature are marked in the upper plot.

FWHM of approximately 0.9 eV, with a maximum at a binding energy of approximately 13.0 eV. Again, asterisks mark the maxima of the dispersing feature measured by Kassühlke (red) [137] and Schwentner (yellow) [69]. Kassühlke's dataset was measured on multilayers of crystalline krypton. Electrons emitted in the normal direction of the multilayer were detected. The datapoints from Schwentner *et al.* are taken from figure 1 in [69]. Schwentner *et al.* measured bulk, polycrystalline krypton. The photon energy range of drawn datapoints drawn also represents the maximum range in which the dispersing feature is seen in their data.

Our dataset shows a dispersing feature which dominates the spectrum in the photon energy range between 13.7 eV and 14.8 eV. Its shift in binding energy in that photon energy range is approximately 0.25 eV. Its FWHM is approximately 0.25 eV. The slope and the photon energy range are almost identical to the polycrystalline data. A shift in total binding energy of 0.2 eV is observed in our data and in the data from the polycrystalline krypton.

Additionally, in the upper panel, figure 4.7 shows three spectra at selected excitation energies. The excitation energies were chosen at energies at which the dispersing

feature is just visible in our krypton data of the largest clusters we measured. The corresponding excitation energies in the intensity plot are marked by arrows.

Apart from the monomer lines, the cluster band and the dispersing feature, our data contains several artifacts which I would like to explain. All krypton maps shown contain two sharp peaks which appear at almost constant kinetic energies. These two peaks appear to be approximately 0.2 eV apart. In the upper panel of figure 4.7, they can be seen at the 13.7 eV spectrum at binding energies of 12.72 eV and 12.92 eV. In the TOF spectra, these features shift by only a few nanoseconds in the observed excitation energy range. To increase the energy resolution, the magnetic bottle was set to parameters at which slow electrons have TOFs above 800 ns. In fact, electrons with kinetic energies below approximately 0.32 eV had TOFs above 1600 ns. This means that the slow electrons are recorded at TOF regions also accessible to fast electrons from the preceding photon bunch. The time of flight conversion, which was intended for the slow electrons, incorrectly converts those fast electrons. Contributions in the excitation light from the third and fifth harmonic are probably present in the excitation energy range used here.

A second artifact in the maps is from the Kr $4p_{3/2}$ and Kr $4p_{1/2}$ monomer lines which, for some photon energies, have kinetic energies below approximately 0.32 eV. These two sharp peaks appear in the plot at excitation energies of 14.1 eV to 14.3 eV and 14.7 eV to 15.0 eV, respectively. This artifact is seen best at an excitation energy of 14.1 eV. There, it appears to be at a binding energy of 13.5 eV. This peak is the Kr $4p_{3/2}$ monomer line, with a kinetic energy of approximately 0.1 eV. It has a TOF above 1600 ns and is therefore incorrectly converted by the time to energy table. Again, the reason that the acceleration voltage was set so low was to increase the energy resolution at those kinetic energies at which the dispersive feature is visible.

In order to obtain an estimate for the onset of the bulk behavior, we measured krypton clusters of different sizes. Figures 4.8 and 4.9 show color-coded intensity plots of photoelectron spectra of krypton clusters with mean sizes of $\langle N \rangle = 270$ and $\langle N \rangle = 120$.

The aforementioned monomer lines and artifacts are visible in both figures. The dispersing feature is also visible in both plots. Clusters with a mean size of $\langle N \rangle = 270$ show a dispersing feature which resembles, both in slope and excitation energy range, that of clusters with a mean size of $\langle N \rangle = 700$. It is slightly shifted towards higher binding energies, by approximately 0.05 eV, and its intensity relative to the intensity of the cluster band is reduced. Clusters with a mean size of $\langle N \rangle = 120$ show a dispersing feature in a slightly narrower range of excitation energies compared to larger clusters. The feature is, compared to clusters with a mean size of $\langle N \rangle = 700$, shifted to higher binding energies by approximately 0.1 eV. The intensity, relative to the broad cluster band, is small.

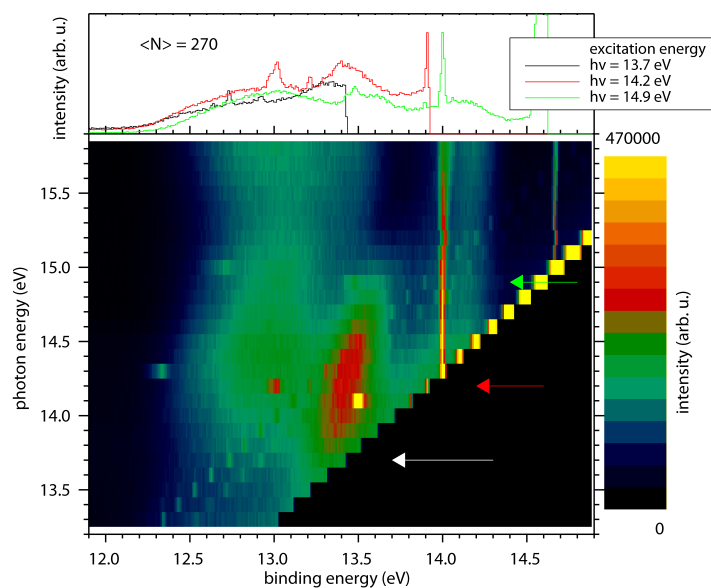


Figure 4.8: Color-coded intensity plot of the Kr $4p$ derived spectra of krypton clusters with a mean size of $\langle N \rangle = 270$.

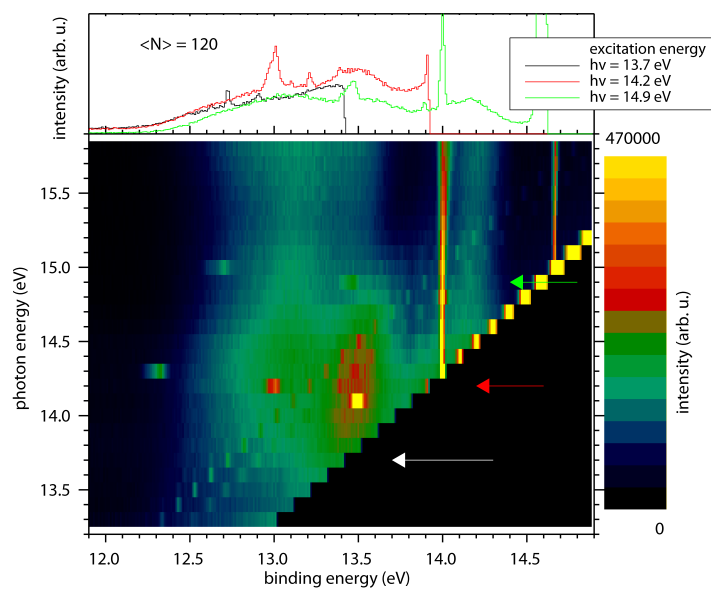


Figure 4.9: Color-coded intensity plot of the Kr $4p$ derived spectra of krypton clusters with a mean size of $\langle N \rangle = 120$.

We also measured a series of Kr $3d$ spectra. Comparison of the Kr $3d_{5/2}$ derived bulk and surface contributions should allow for an estimate of the cluster size [132]. Unfortunately, the quality of these measurements is poor, due to a high background and low statistics. Clusters with a mean size of $\langle N \rangle = 700$ had a bulk-to-surface ratio of approximately unity. Assuming an *fcc*-like, icosahedral structure, this corresponds to a cluster size between 300 and 500 atoms. All other clusters had a bulk-to-surface ratio in the range of 0.4 to 0.7. However, due to a substantial non-linear background, the uncertainties are very large and systematic differences in the bulk-to-surface ratio for clusters with mean sizes of $\langle N \rangle = 120$, $\langle N \rangle = 270$ and $\langle N \rangle = 420$ could not be verified. For all three cluster sizes, the bulk-to-surface ratios were approximately 0.5 ± 0.3 . Comparing the cluster sizes obtained from the scaling law with bulk-to-surface measurements of the largest clusters suggests that the scaling law overestimates the actual cluster size.

4.3 Discussion and conclusions

Both argon and krypton clusters show a dispersing feature in a narrow range of excitation energies. The shift in binding energy of large clusters is approximately 0.6 eV in the case of argon and approximately 0.25 eV in the case of krypton clusters. These dispersing features are also seen in photoemission spectra of the bulk, both in crystalline and polycrystalline samples. Argon clusters with a mean size of $\langle N \rangle = 95$ show a shift in binding energies almost as large as that of large clusters. A comparison with cluster sizes determined by measuring bulk-to-surface ratios in Ar $3s$ photoemission spectra shows that this corresponds to clusters with a size of approximately 230 atoms. In case of krypton clusters, the full shift in binding energy is observed at clusters with a mean size of $\langle N \rangle = 270$. Measurements of bulk-to-surface ratios of the Kr $3d_{5/2}$ cluster contribution indicate that the scaling law slightly overestimates the actual cluster size. This means that the onset of bulk-like behavior is at cluster sizes of approximately 230 atoms in the case of argon and at cluster sizes below approximately 270 in the case of krypton.

The question arises whether effects other than band dispersion can explain the feature observed. A depth dependence in the binding energy could be caused by inelastic intracluster electron-electron scattering. The electron kinetic energies at which the feature is visible are in the range of 1 eV to 2.3 eV in the case of argon clusters and in the range of 0.4 eV to 1.4 eV in the case of krypton clusters. The mean free path of electrons in bulk argon and krypton has been measured by Schwentner *et al.* [76]. Their findings for the onset of inelastic electron-electron scattering are summarized in table 2.3. At the kinetic energies observed both argon and krypton have a mean free path

of at least some hundred nanometer. Argon clusters with a size of $N = 1670$ have a diameter of approximately 5.5 \AA . This means that electrons from bulk sites of any of the observed clusters are essentially unattenuated. If any depth dependency effects play a role, then the feature should also be observable in spectra of mixed Ar-Xe clusters as shown in figure 6.1. In this system, up to three argon layers are found to surround a core consisting of xenon atoms. This means that an electron from an argon atom at an interface site has to pass at least two argon atoms to reach the vacuum. This is somewhat comparable to an electron stemming from the central site of a homogeneous cluster with five layers. A cluster with five layers has 309 atoms. But at this size, both in argon and krypton clusters, the dispersing feature is already fully developed.

The observation of dispersion in a non-oriented sample is surprising. Usually, a single crystal sample is fixed in space and a dispersion curve can be measured under a fixed emission angle. This way, the dispersion can be determined along a selected symmetry direction in reciprocal space. In our case, the dispersion of the initial state may be similar along different directions of the Brillouin zone. Another explanation: if the transitions are confined to only one direction in the Brillouin zone, those clusters with approximately the correct orientation will show the effect.

Comparisons to theory are not easy because, to my knowledge, no calculations for rare gas clusters exist. Some experimental data from bulk argon could only recently be reproduced theoretically by Galamic-Mulaomerovic *et al.* [129].

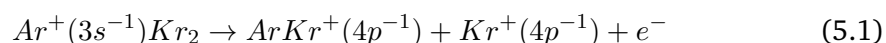
The large width of the cluster size distribution is a major handicap in the experiment described here. Electron spectra of size-selected clusters could be produced using photoelectron-cluster ion coincidence spectroscopy (see for example [138]). Here, however, evaporation of neutrals would have to be quantified. Also, the drastic decrease in signal is a challenge that future experiments must resolve.

In summary, I have presented photoelectron spectra of argon and krypton clusters measured close to the ionization threshold. Both argon and krypton clusters show a dispersing feature in a small region of excitation energies. By comparing these spectra with experimental results from bulk-monocrystalline and bulk-polycrystalline species, I arrive at the conclusion that the feature is caused by dispersion of the np -derived valence band. The feature was then measured at a series of cluster sizes to establish the onset of this bulk-like behavior. Using scaling laws and comparisons to measurements of bulk-to-surface ratios, I come to the conclusion that the feature begins to show its full dispersion at cluster sizes of approximately $N = 230$ in the case of argon and $N \leq 270$ in the case of krypton.

In the next chapters, I will present outer valence spectra of mixed Ar-Kr and Ar-Xe clusters. The cluster size dependent measurements of the outer valence spectra of the homogeneous species, which have been presented in this chapter, will be used to discuss aspects of the size and composition of the mixed clusters.

5 Electron transfer mediated decay in mixed Ar-Kr clusters

The ETMD process has already been described in general in section 2.3.4. Pernpointner *et al.* predicted the occurrence of ETMD in Ar-Kr₂ trimers [6]. They found that an Ar⁺(3s⁻¹) vacancy in that trimer cannot decay via ICD, while a decay according to:



is energetically allowed, if the two krypton atoms are at least a certain minimum distance apart. The linear configuration of the trimer, Kr - Ar - Kr, already has a DIP of only 29 eV. This is below the single ionization energy of the Ar⁺(3s⁻¹) state of 29.3 eV. This chapter presents experiments made on mixed Ar-Kr clusters to demonstrate the existence of ETMD. I will present outer and inner valence photoelectron spectra of argon, krypton and mixed Ar-Kr clusters in order to discuss aspects of the composition and structure of the mixed clusters. I will also present two-electron coincidence maps recorded after inner-valence ionization of argon, krypton and Ar-Kr clusters. I will argue that the data presented provides clear evidence for the occurrence of ETMD. Some of the presented data has been published in reference [139].

5.1 Outer valence spectra of mixed Ar-Kr clusters

Figure 5.1 shows the photoelectron spectra of homogeneous argon and krypton clusters. Both spectra were taken at an excitation energy of 16.2 eV. The measurement of argon clusters comes from the experiments described in the previous chapter and was taken at TGM4; the other three were made at UE 112. In the left panel, both the Ar 3p_{1/2} and Ar 3p_{3/2} monomer lines can be seen at their respective binding energies of 15.94 eV and 15.76 eV. The sharp feature at approximately 0.5 eV kinetic energy is an artifact from a higher harmonic contribution in the excitation light. The broad Ar 3p derived cluster contribution can be seen, with a FWHM in kinetic energy of 1.3 eV and a maximum at 1.25 eV kinetic energy. It is dominated by the dispersing feature described in the previous chapter.

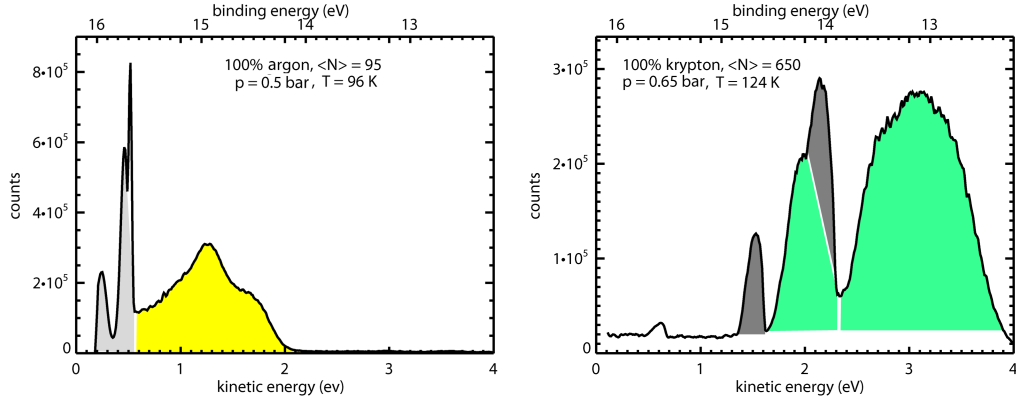


Figure 5.1: Argon cluster (left) and krypton cluster (right) photoelectron spectra at an excitation energy of $h\nu = 16.2$ eV. The contributions from the monomers are shaded in gray. The cluster contributions are highlighted in different colors.

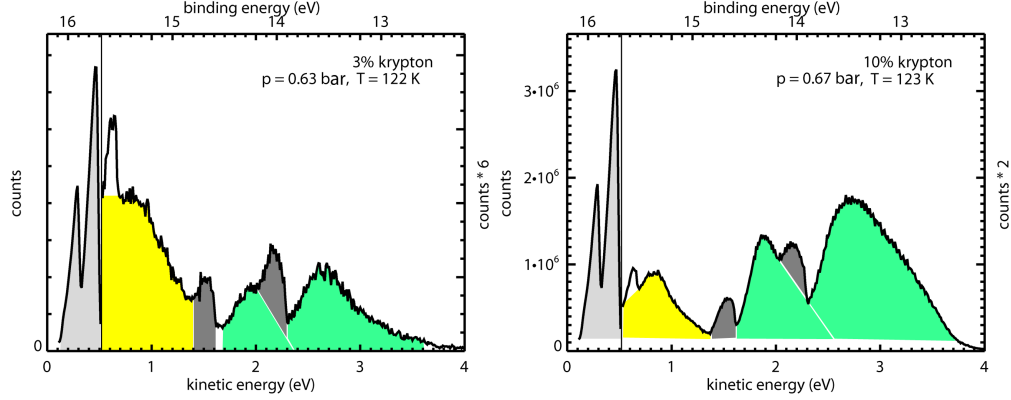


Figure 5.2: Photoelectron spectra of mixed Ar-Kr clusters taken at $h\nu = 16.2$ eV. For clarity, the monomer contributions of argon and krypton are shaded in light and dark gray, respectively, according to figure 5.1. The cluster contributions of argon and krypton are highlighted yellow and green, respectively, also according to figure 5.1. The part of the spectra below 0.52 eV kinetic energy corresponds to the left vertical axis. This part is showing the Ar $3p$ monomer lines, which quantitatively dominate the spectrum. The remainder of the spectrum is scaled up, corresponding to the right vertical axis.

The photoelectron spectrum of krypton clusters, with a mean size of $\langle N \rangle = 650$, features both Kr $4p_{1/2}$ and Kr $4p_{3/2}$ contributions at binding energies of 14.7 eV and 14.0 eV, respectively. The latter is superimposed on the Kr $4p_{1/2}$ derived cluster band. The contribution from the Kr $4p_{3/2}$ cluster band has a FWHM of 1.1 eV and is symmetrical around a maximum at 13.1 eV binding energy. At 0.6 eV kinetic energy, this spectrum also shows an artifact from a higher harmonic contribution in the excitation light.

Figure 5.2 shows photoelectron spectra of a mixture of argon and krypton coexpanded at parameters comparable to those in figure 5.1. Results for two different mixing ratios, 3 % (left) and 10 % (right) krypton, are shown. The main contribution in both spectra, seen in the unscaled left parts, are the Ar $3p$ monomer lines. Additionally, the cluster contributions of the Ar $3p$ electrons, the Kr $4p$ monomer lines and the Kr $4p$ derived cluster contributions can be seen. The area ratios of the argon to krypton cluster contributions are roughly 1.7 and 0.3 for the 3 % and the 10 % mixtures, respectively. These values were corrected using the total absorption cross sections of the monomers at 16.2 eV: $\sigma_{Ar} = 30.7$ Mb and $\sigma_{Kr} = 42.9$ Mb [140]. The spectrum of the 10 % mixture shows a small shoulder at 3.2 eV kinetic energy. This feature is absent in the 3 % spectrum. Apart from these differences, the spectra are similar, with comparable binding energies and FWHM of the Ar $3p$ and Kr $4p_{3/2}$ cluster contributions within 0.1 eV.

However, both the Ar $3p$ and the Kr $4p_{3/2}$ cluster contributions differ strongly from the contributions seen in the spectra of the homogeneous species. The maximum of the Ar $3p$ cluster contribution shifts by 0.3 eV to 15.4 eV binding energy while the FWHM decreases by 0.4 eV to 0.9 eV. The dispersing feature is completely absent. The maximum of the Kr $4p_{3/2}$ cluster contribution shifts by 0.4 eV to 13.5 eV binding energy while the FWHM decreases by 0.3 eV to 0.8 eV. The shape of the contribution changes from the symmetrical distribution around the maximum seen in the homogeneous species to a contribution resembling a log-normal distribution in the heterogeneous spectra.

The shift in binding energies and FWHM of the cluster contributions, as well as the change in the degree of condensation, shows that the clusters produced here were mixed. This is the case for both mixing ratios shown. It is plausible that the mixed clusters are spherical (compare section 2.1.3). The parameters α and β (compare table 2.2) are almost equal. This means that interactions between the argon and krypton atoms are almost identical.

Experimental findings by Lundwall *et al.* [54, 55], as discussed in section 2.1.3, show that coexpanding a mixture of argon and krypton leads to mixed clusters with a krypton core and an argon shell, but without a sharp segregation of the two atomic species. Based on theoretical considerations, Vach comes to similar conclusions [29].

The strong red shift and the narrowing of the FWHM of both the krypton and the

argon cluster bands indicates that the delocalization of the outer valence electrons is small. This means that the clusters produced are probably very small. Another explanation is that the clusters are highly amorphous. The shoulder observed at 3.2 eV kinetic energy in the spectrum of the 10 % mixture indicates a larger delocalization of outer valence electrons as compared to the 3 % mixture.

5.2 Inner valence spectra of mixed Ar-Kr clusters

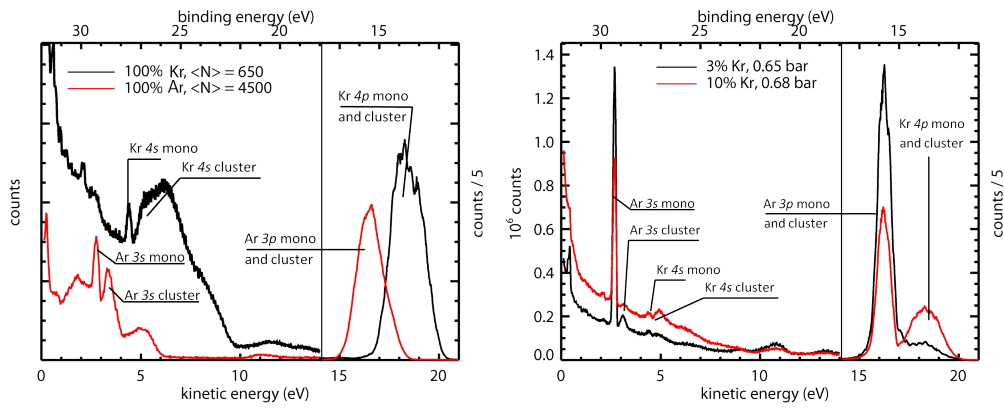


Figure 5.3: Photoelectron spectra of homogeneous argon and krypton clusters at an excitation energy of $h\nu = 32.0$ eV (left) and photoelectron spectra of the heterogeneous species Ar-Kr at the same excitation energy and with two different mixing ratios (right). At kinetic energies above 14 eV, the spectra have been scaled down by a factor of five.

The inner valence photoelectron spectra of homogeneous argon, homogeneous krypton and mixed Ar-Kr clusters at two different mixing ratios are shown in figure 5.3. Again, the spectrum of homogeneous argon clusters was measured at TGM 4; the other three spectra were taken at UE112. The spectra are dominated by the np -contributions. This part of each spectrum was scaled down by a factor of five. The region of higher binding energy is dominated by contributions from excitonic states. This is to be expected at these low excitation energies. The Ar 3s and Kr 4s monomer lines can be seen as sharp features at their respective binding energies of 29.3 eV and 27.5 eV. The Ar 3s cluster and bulk contributions in the homogeneous spectra can be seen at binding energies in the range of 28.1 eV to 29.0 eV. The Kr 4s cluster and bulk contributions cannot be distinguished clearly due to the high background in that region.

The spectra of the mixed species show the same features. Again, the Kr 4s cluster contribution cannot be distinguished. The Ar 3s cluster contribution is very small compared to the contribution from the monomers. This is the case for both mixing

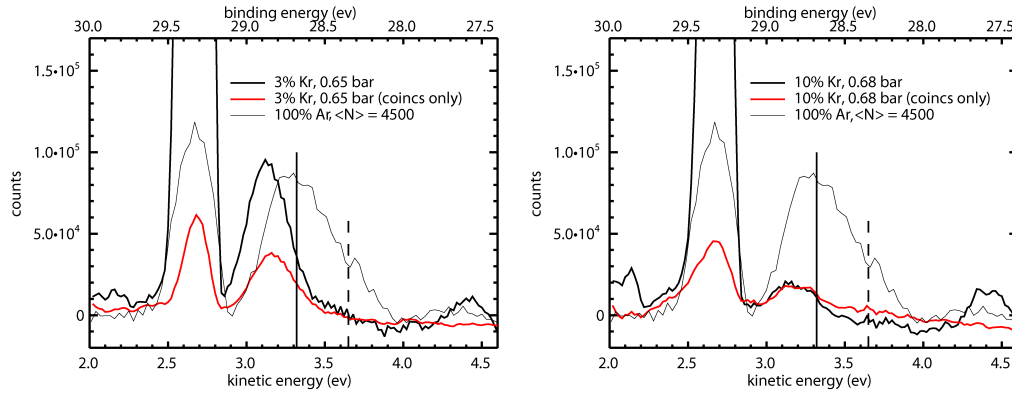


Figure 5.4: The Ar 3s region of the mixed Ar-Kr clusters with 3 % krypton in the initial mixture (left) and 10 % krypton in the initial mixture (right) in comparison with homogeneous argon clusters. The spectra shown were extracted from the spectra in figure 5.3. A non-linear background was subtracted for clarification. Two vertical lines have been included to mark the position of the maxima of the bulk contribution (dashed) and surface contribution (solid) of argon clusters with a mean size of $\langle N \rangle = 1000$ as found by Feifel *et al.* [132]. Additionally, the colored lines show the contribution of only the coincident electrons to the total spectra of the mixed species.

ratios. Each spectrum includes counts from a 600 s long measurement. Before and after that measurement, spectra as shown in figure 5.2 were taken. There is a discrepancy between the degrees of condensation derived from the outer and the inner valence spectra. The outer valence spectra consistently showed a much higher cluster to monomer ratio (compare figures 5.4 and 5.2). I cannot explain this discrepancy; I can only assume that there is a difference in the differential cross-section between the Ar 3s monomer and the Ar 3s cluster contributions. However, what is important here is that the Ar 3s cluster contributions can clearly be seen in a binding energy range from approximately 28.5 eV to 29.1 eV.

Figure 5.4 shows a magnified section of the spectra from figure 5.3 in the kinetic energy region of the Ar 3s electrons. Also shown are spectra from the same dataset, from which hits which include only one electron have been subtracted. This means, electrons are only histogrammed if they were recorded in coincidence with a second electron. Included in this figure are also spectra from homogeneous argon clusters with a mean size of $\langle N \rangle = 4500$. For clarity and to allow comparison, a non-linear background was subtracted from the spectra (a background was not subtracted from the spectra shown in figure 5.2).

The binding energy range of the Ar 3s derived cluster band is, in both cases shown, narrower and red-shifted compared to the spectrum from the homogeneous species.

The 3 % mixture has contributions at binding energy ranges even lower than those expected from surface sites in the homogeneous argon cluster. The 10 % mixture shows argon binding energies in the energy region corresponding to the surface contributions in the homogeneous species.

Let's take a look at the differences between the spectra of all recorded electrons and those which include only coincident electrons. The 10 % mixture (right panel in figure 5.4) shows almost no difference between the total and the coincidences-only spectra. This means, that almost all electrons from the Ar 3s band lead to the emission of secondary electrons. This is different in the 3 % mixture. Not only is the contribution of coincident electrons to the total spectrum smaller, it is also slightly shifted to lower binding energies. This means that the binding energies of the electrons which autoionize are shifted compared to those which don't. Interestingly, the spectra of the coincident electrons has intensity at the same binding energy region as the surface contribution from the homogeneous species. An explanation of this effect is given in the next section.

The narrowness of the outer valence cluster bands shows that the clusters produced are very small. The Ar 3s derived cluster band contribution indicates a reduction in the number of nearest neighbors of the argon atoms which pertain to the spectrum. This suggests that, especially in the 3 % mixture, the argon surface layer of the clusters is not completely filled. The 3 % mixture results in a ratio of argon to krypton atoms in the clusters of approximately 1.7 (derived from the outer valence spectra, assuming that the atomic cross sections are identical to the cross sections of the atoms in the cluster). These findings, in combination with a comparison with figure 6.4, indicate a krypton core of three layers. Lundwall *et al.* [54, 55] found, in agreement with theoretical expectations (compare table 2.2), that, at least in the interface region, mixing of argon and krypton atoms takes place. The spectra measured here show no argon bulk contributions.

The 10 % mixture shows an argon to krypton ratio of approximately 0.3. Again, the spectrum suggests that argon is only found on some sites of the surface of the cluster (narrow Ar 3s bands). Assuming this is true, comparison with figure 6.4 indicate a krypton core of approximately 9 to 10 layers. However, this conclusion is in disagreement with the width of the outer valence band. It is narrower than that of the homogeneous species with a mean size of $\langle N \rangle = 650$, or approximately 5 layers of krypton.

Therefore it is difficult to draw final conclusions about the clusters' structure. To do so, it would be necessary to conduct a more detailed study of the inner valence spectra at excitation energies which show no excitonic states. This, however, would be difficult with the experimental equipment used here because the energy resolution decreases with increasing kinetic energy.

An important detail about the spectra is that the Ar 3s cluster feature can be clearly

distinguished from the Ar $3s$ monomer and krypton contributions. This is the region of primary electron energy in which coincidences are expected, if ETMD indeed takes place.

5.3 Electron-electron coincidence spectra of Ar-Kr clusters

Using equation 2.20, an Ar $3s$ cluster ionization energy range of 28.1 eV to 29.0 eV, a Kr $4p$ cluster ionization range energy of 12.5 eV to 14.0 eV and an internuclear distance between two krypton atoms in a Kr–Ar–Kr configuration of 0.7 nm (compare table 2.3), one can calculate the expected energy of the ETMD electron to be in the range of 0 eV to 1.1 eV. Electrons with such low kinetic energies are difficult to detect against a background of secondary electrons, which clearly dominate the spectrum (compare the spectra in figure 5.3). For this reason, it is necessary to measure the electrons in coincidence. Figures 5.5 to 5.7 show color-coded coincidence maps of histogrammed two-electron events as explained in section 3.5.2. The yield of electron coincidences is plotted as a function of the binding energy of the first electron versus the kinetic energy of the second electron. Figure 5.5 shows the coincidence maps of homogeneous argon clusters with a mean size of $\langle N \rangle = 4500$ (left panel) and of homogeneous krypton clusters with a mean size of $\langle N \rangle = 650$ (right panel). The corresponding non-coincidence spectra are shown in the left panel of figure 5.3. Both figures were generated from the same experiment and data-set. The map of argon shows almost no coincidences. Only in a region in which both the first and second electrons had very small kinetic energies, some coincidences are seen. The region of the Ar $3s$ cluster contribution is marked by two horizontal lines. The coincidence map of krypton clusters shows a broad, unstructured intensity in the range from 26 eV to 28 eV binding energy of the first electron and very low kinetic energies of the second electron. In all figures, the panels labeled a) and c) show the projections of the coincidence maps onto the axes of the respective electrons. While in the c)-panels, all coincidences of the map are included in the projection, the a)-panels only show the projection of the region marked by two horizontal black lines. This region corresponds to the binding energy region of the Ar $3s$ cluster electron as determined from the non-coincident spectra; in the case of homogeneous krypton clusters, the same region as in the homogeneous argon clusters was chosen.

Figures 5.6 and 5.7 show coincidence maps of mixed Ar-Kr clusters, all excited at an energy of 32 eV. Table 5.1 gives an overview of the experimental parameters which correspond to the data presented in figures 5.3 to 5.7. In all figures, the binding energy region of the Ar $3s$ cluster contribution is marked in the b)-panels by two horizontal black lines. The four horizontal red lines in the b)-panels indicate regions of the spectra

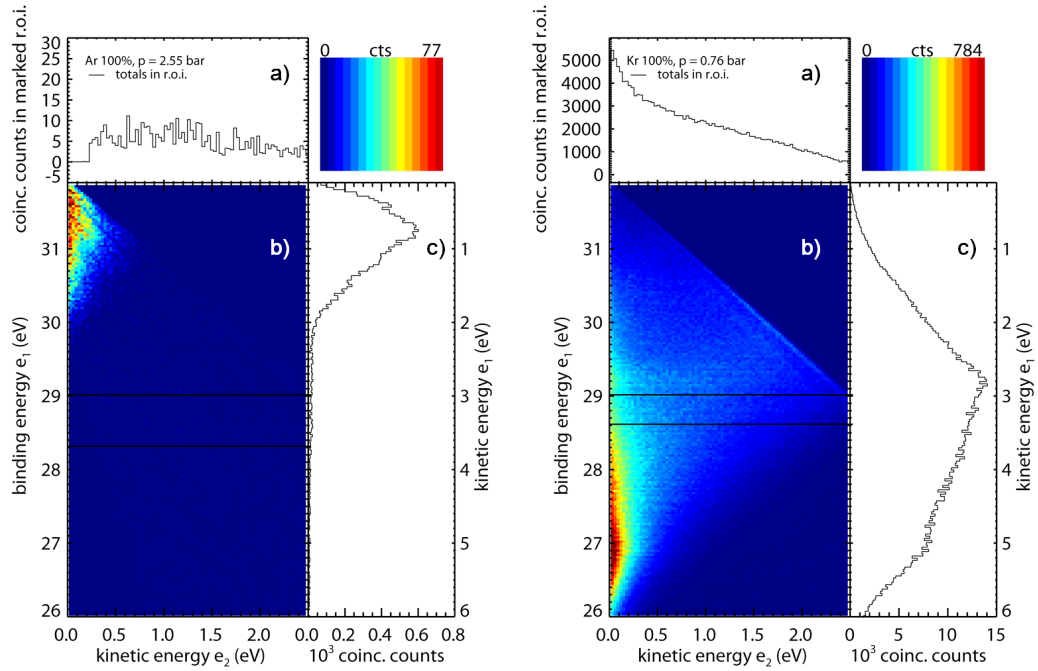


Figure 5.5: Electron-electron coincidence spectra after photoionization of argon clusters (left) and krypton clusters (right) at $h\nu = 32$ eV. In both maps, the black horizontal lines in the b)-panels mark the binding energy region of the Ar $3s$ cluster electrons. The c)-panels show the projection of all counts onto the axis of e_1 . This corresponds to the binding energy spectrum of all primary electrons that contribute to the emission of secondary electrons. The a)-panels show the projection of all counts within the region marked by two horizontal black lines in the b)-panels, onto the axis of e_2 . This is the kinetic energy spectrum of all secondary electrons emitted in coincidence with primary electrons which have binding energies in the region of the Ar $3s$ cluster band. Intensity is given as events per pixel, with a pixel width of 33 meV x 33 meV.

which were used to estimate the background in the Ar $3s$ cluster region. It is important to mention that this *background* comes from true coincidences, because a background of random coincidences has already been subtracted. A discussion of this broad feature, which is apparent in all coincidence maps, will be given below. The a)-panels show, with a red line, the projection of the map within the region between the two black horizontal lines minus half the sum of the projection of the map within the regions marked by the red horizontal lines. This is an estimate of the kinetic energy spectrum of secondary electrons which were recorded in coincidence with electrons in the binding energy region of the Ar $3s$ cluster contribution.

The left panel in figure 5.6 shows results from measurements made with the lowest krypton content in the initial gas mixture. A sharp feature, at kinetic energies of up

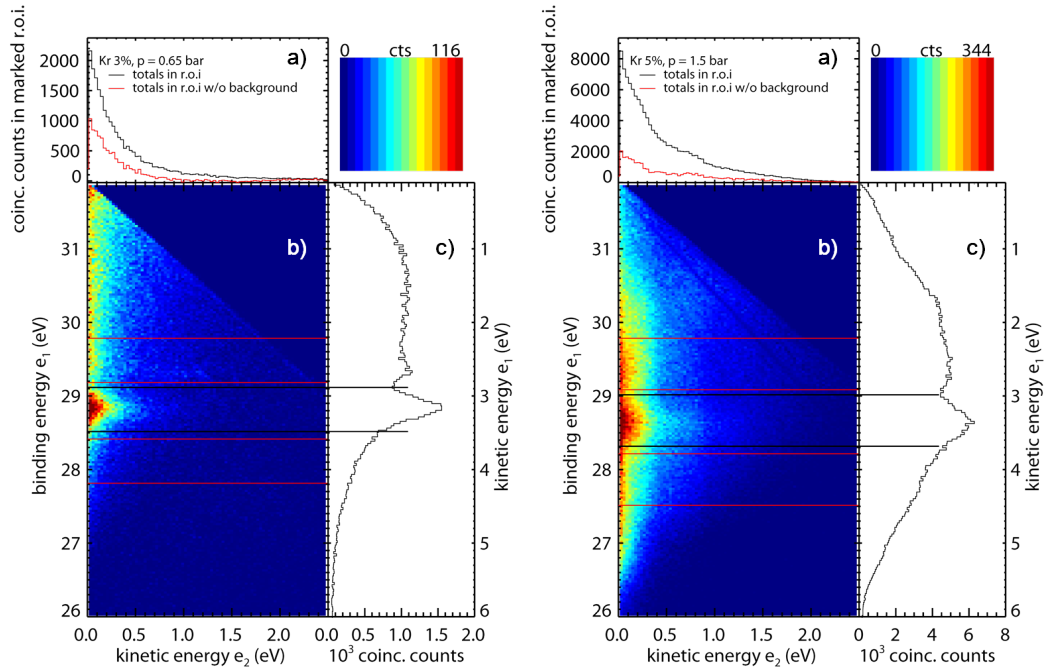


Figure 5.6: Electron-electron coincidence spectra after photoionization of Ar-Kr clusters with different mixing ratios and expansion pressures, taken at $h\nu = 32$ eV. Again, in all maps, the black horizontal lines in the b)-panels mark the binding energy region of the Ar $3s$ cluster electron. The red horizontal lines mark regions which were used to estimate the background. In all maps, the red spectra in the a)-panels show the difference of the of the projection within the black horizontal lines minus half the sum of the projections within the regions between the red horizontal lines in the b)-panel. The intensity is given as events per pixel, with a pixel width of 33 meV x 33 meV.

to 0.6 eV of the e_2 electron, can be seen at binding energies between approximately 28.5 eV and 29 eV. This is the binding energy region of the Ar $3s$ derived cluster band. There are no counts in the region of the atomic Ar $3s$ line other than those from the background. This was expected, because an Ar $3s$ vacancy in the monomer cannot decay via emission of a second electron. The background comes from coincidences of electrons in the kinetic energy region of 0 eV to 4 eV with coincident electrons in the kinetic energy region of 0 eV to approximately 0.3 eV. The maximum of the distribution is at very low kinetic energies of both electrons.

The right panel in figure 5.6 and both panels in figure 5.7 show coincidence maps resulting from initial mixing ratios with at least 5 % krypton. All maps show an increased intensity in the Ar $3s$ cluster band region. The kinetic energies of the secondary electrons reach up to 0.9 eV. The maximum of the distribution of the kinetic energies of the secondary electrons is below 0.1 eV. There is also a broad and unstructured feature of

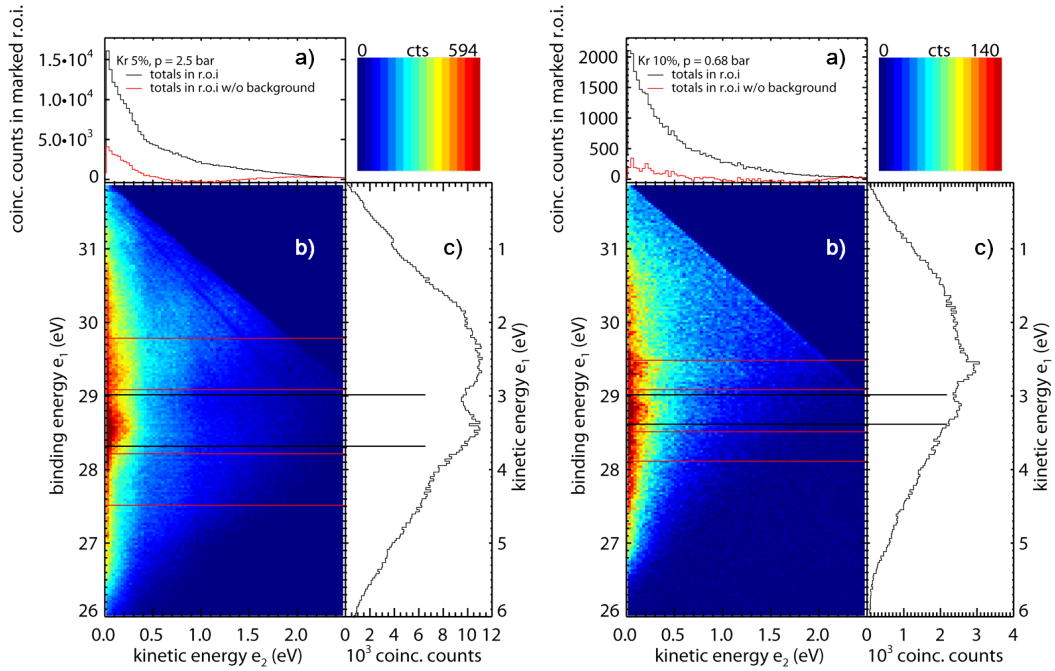


Figure 5.7: Electron-electron coincidence spectra after photoionization of Ar-Kr clusters with different mixing ratios and expansion pressures taken at $h\nu = 32$ eV. More details are found in the caption of figure 5.6 and in the text.

very slow electrons in coincidence with electrons from binding energies in the range of 27 eV to 31 eV. As expansion pressure and krypton content rise, this feature increasingly becomes the dominating feature on the map.

I identify the low kinetic energy electrons, which are detected in coincidence with the Ar 3s cluster band, as the continuum electrons emitted via the ETMD(3) process. The coincidence maps of the homogeneous species show no similar features in the region of interest. Spectra taken at different excitation energies (31 eV and 34 eV, not shown here) exhibit a similar feature at binding energies corresponding to the Ar 3s cluster electron. The clusters are mixed and the DIPs are lower than required. Figure 5.8 shows the ETMD spectrum measured at the smallest cluster size and smallest krypton ratio in the initial gas mixture. This is the spectrum with the lowest background. The ETMD electrons have kinetic energies up to approximately 1 eV. This agrees very well with the calculations made at the beginning of this chapter. The kinetic energy distribution of the ETMD electrons has its maximum below 0.1 eV.

Could other processes pertain to the ETMD spectrum? A decay via Ar-Kr ICD may be energetically allowed for large clusters. Assuming binding energies of 15 eV and lower for the Ar 3p cluster band, 12.7 eV and lower for the Kr 4p band and binding energies of

Table 5.1: Parameters pertaining to the data presented in figures 5.3 to 5.7. The values of the energy ranges were determined from the non-coincident spectra of the respective species. The uncertainties were estimated using Gaussian fits of the data and the energy resolution of the beamline. (* krypton content in the initial gas mixture, ** krypton content in the clusters as derived from the outer valence spectra.)

% Kr*	% Kr**	p_{stag}/bar	T/K	$\langle N \rangle$	$E_{bind}(Ar3s) / eV$	Beamline
0	0(0)	2.5	113	4500	28.2(1) to 29.0(2)	TGM 4
3	37(10)	0.65	122	/	28.5(1) to 29.1(1)	UE 112
5	/	1.5	118	/	28.3(3) to 29.0(2)	TGM 4
5	/	2.5	118	/	28.3(3) to 29.0(2)	TGM 4
10	77(10)	0.68	123	/	28.6(2) to 29.0(1)	UE 112
100	100(0)	0.76	123	650	/	UE 112

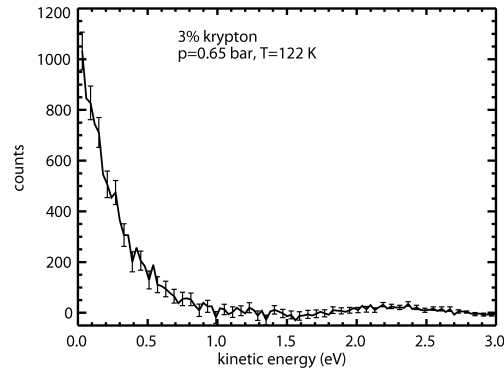


Figure 5.8: ETMD spectrum, after background subtraction from measurements of mixed Ar-Kr clusters with 3 % krypton in the initial gas mixture (approximately 37 % krypton in the final cluster). Error bars are plotted for every second data point. The error was calculated as the weighted sum of the statistical error of the estimated background and the statistical error of the spectrum before background subtraction.

up to 28.8 eV in the Ar 3s band, one can calculate that the minimum distance at which ICD is possible is approximately 13 Å:

$$\frac{1}{4\pi\epsilon_0} \frac{e^2}{r} > IP_{Ar3s} - IP_{Kr4p} - IP_{Ar3p} \quad (5.2)$$

The decay width at this distance can be estimated, according to 2.23, to be in the order of 1×10^{-4} meV. This corresponds to a lifetime of 6.5 ns, which is almost as long as the radiative lifetime of the Ar 3s vacancy with 7.4 ns [141]. The coincidence spectra of the

Ar $3s$ line shows that a large percentage of the Ar $3s$ vacancies in the cluster autoionize. The fraction of the recorded signal in the binding energy range of the valence bands in which ICD is allowed is, especially in the case of small clusters, very small. For these two reasons, a contribution of ICD to the ETMD spectrum is very unlikely.

Let us address the aforementioned shift in binding energies of coincident electrons in the Ar $3s$ derived cluster band of the 3% mixture. I showed that, at this mixing ratio, it is likely that most of the argon atoms are located on the surface of clusters with a small krypton core. This, however, means that the number of available sites for ETMD is reduced. The two krypton atoms participating in the ETMD cannot be neighbors due to energetic reasons. But the argon atom and at least one krypton atom must be neighbors because an overlap of the valence orbitals is crucial for ETMD. Therefore, only argon atoms which are at least partially surrounded by krypton atoms are able to decay via ETMD. Such argon atoms have smaller binding energies than those on the surface; therefore the spectrum of the coincident Ar $3s$ cluster electrons is shifted compared to that of all electrons (again, *all electrons* means electrons corresponding to histogrammed TOFs of all hits from all events which have one or two hits). The argon atoms on the surface cannot decay via autoionization and therefore must decay via radiation. As a result, electrons from photoionization of these sites are not visible in the coincidence spectrum. I present some of these different situations in figure 5.9 using two dimensional schematics of clusters.

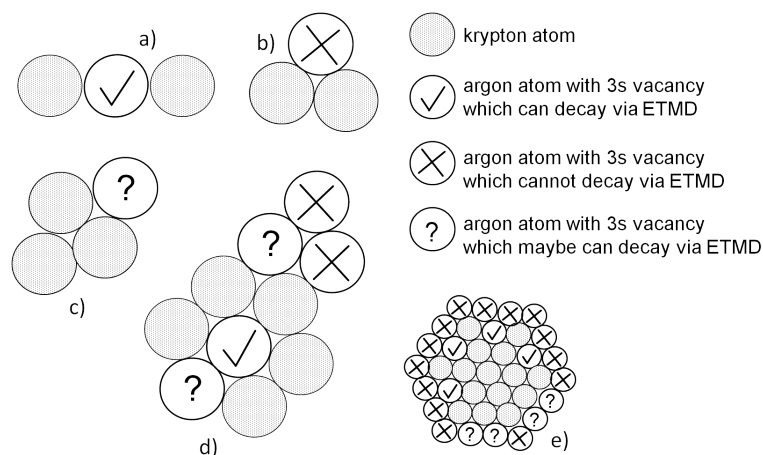


Figure 5.9: Schematic of some two-dimensional hypothetical geometries of two-dimensional Ar-Kr clusters to illustrate sites at which an Ar $3s$ vacancy can decay via ETMD and others at which it cannot. Cluster a) is the hypothetical trimer for which ETMD is energetically possible and was predicted by Pernpointner *et al.* [6]. In case b), a decay is energetically impossible. It is not clear, whether a decay is energetically possible in case c). In clusters d) and e), a decay is geometrically not possible at some sites and might energetically not be possible at other sites.

Let me now address the broad feature in the coincidence maps. It is seen with different intensities and energies in all coincidence maps of the mixed species. Its intensity increases with increasing krypton content in the initial gas mixture and with increasing expansion pressure. The kinetic energy of the second electron reaches approximately 1 eV and the kinetic energy of the first electron is in the region of approximately 0 eV to 6 eV. The homogeneous species also show intensity in the coincidence maps. The homogeneous argon clusters show pairs of electrons with a total kinetic energy of no more than approximately 1.5 eV. Homogeneous krypton clusters show electron pairs with total kinetic energies in the range of approximately 2.5 eV to 5.5 eV. Assuming that those features are solely caused by intracluster electron-electron scattering from electrons of the np orbitals, one can make the following assumptions.

The Coulombic energy between two vacancies in a krypton cluster can be estimated according to 2.21. Using interatomic distances in the range of 3.6 Å to 14.6 Å (compare table: 2.3) and 2.21, one can calculate values in the range of 1 eV to 4 eV. Using a binding energy of 12.5 eV for large clusters of the Kr $4p$ cluster band and an excitation energy of 32 eV, one can now estimate the total energy available for a pair of electrons after intracluster electron-electron scattering to be in the region of 3 eV to 6 eV. This is approximately the region in which the feature of the homogeneous krypton clusters is seen. According to similar considerations, one can calculate a total kinetic energy below approximately 1 eV for the scattering of two Ar $3p$ electrons. This, again, is the energy region in which the feature of the homogeneous argon clusters is seen. The mixed species contain argon and krypton and a third possibility for intracluster electron-electron scattering exists. Scattering of one Kr $4p$ and one Ar $3p$ electron would lead to a total available kinetic energy in the range of approximately 0 eV to 3 eV (according to the same calculations and estimations as above).

Figure 5.10 shows the kinetic energy spectra of all primary coincident electrons of some selected clusters up to energies of 7.5 eV. The spectra of the clusters which contain krypton were normalized to the area of the coincident Kr $4s$ contributions (shown in figure 5.3). The spectrum of argon clusters was scaled up. With the assumption that the broad feature from the homogeneous species is caused by electron scattering, the spectra of the mixed clusters in figure 5.10 can be explained as follows. Clusters with a 3 % krypton content in the initial gas mixture show intracluster electron-electron scattering mainly from Ar $3p$ - Ar $3p$ and Ar $3p$ - Kr $4p$ electrons. The clusters with a 10 % krypton content in the initial gas mixture show mainly Kr $4p$ - Kr $4p$ and Ar $3p$ - Kr $4p$ scattering. The aforementioned expected kinetic energy regions of electrons pertaining to these scattering processes, match this picture. It is also in agreement with the conclusions about the cluster sizes drawn earlier. Kr $4p$ - Kr $4p$ scattering is not expected in clusters with a very small krypton core (3 % mixture). Kr $4p$ -Kr $4p$ scattering is more likely in the larger clusters (10 % mixture). Here, however, Ar $3p$ - Ar $3p$ scattering is

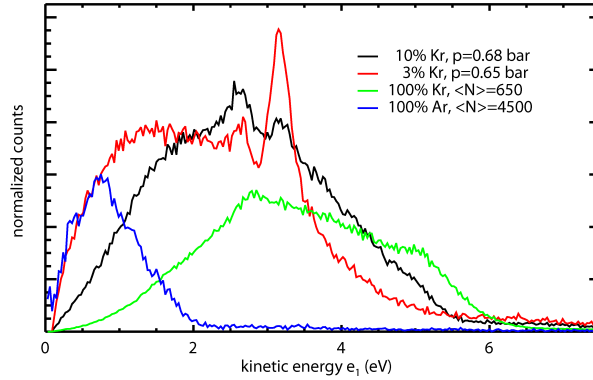


Figure 5.10: Kinetic energy spectra of all e_1 electrons of clusters with various expansion parameters. All spectra from clusters containing krypton were normalized to the area of the Kr $4s$ derived signal shown in figure 5.3 (coincident electrons only). The spectra from the homogeneous argon clusters was scaled up to match the slope of the inhomogeneous species with 3 % krypton in the initial gas mixture at low kinetic energies.

less likely due to a low argon content and because argon is mainly found on the surface of the cluster.

This means that the broad feature can be explained solely by intracluster electron-electron scattering. Three different but overlapping regions of total kinetic energies contribute to the feature. They stem from inelastic scattering of electrons from the np orbitals of different atoms in the clusters.

It might also be possible to explain parts of the spectra as resulting from ICD of the Kr $4s$ cluster vacancy. An estimate using equation 2.21 shows that this would require a distance of approximately 12 \AA between two participating krypton atoms. With a cluster size of approximately $\langle N \rangle = 650$, this distance might be present. However, the r^{-6} dependence of ICD makes this decay channel very unlikely.

Another contribution to the unstructured feature above 29 eV might come from the ICD of KrKr^{+*} satellite states as observed by Lablanquie *et al.* in krypton dimers [82]. These satellite states exist in a dense band above 29 eV binding energy. However, a comparison with the coincidence map of homogeneous krypton clusters shows that this explanation is unlikely.

The spectra show that with increasing cluster size and krypton content, the contribution to the coincidence map from the ETMD electrons becomes smaller. It is unclear whether an unknown competing process to ETMD becomes more relevant with increasing cluster size or whether a decrease is only due to an increase in the aforementioned broad feature with respect to the ETMD feature.

5.4 Conclusions

This chapter presented experiments on heterogeneous Ar-Kr clusters performed to prove the existence of the autoionization decay channel ETMD. Until now, it was not possible to observe this decay channel due to its very low efficiency compared to other autoionization channels and due to a very low expected kinetic energy of the ETMD electron. By preparing mixed Ar-Kr clusters and using electron-electron coincidence spectroscopy with an instrument capable of detecting very slow electrons in very high transmission, I was able to obtain clear evidence for the occurrence of ETMD(3). Three different sites participate in this decay and are connected by electron correlation. The kinetic energy spectrum of the ETMD electron was measured. Its maximum intensity is seen at kinetic energies below 0.1 eV and its maximum energy is reached at energies of approximately 1 eV.

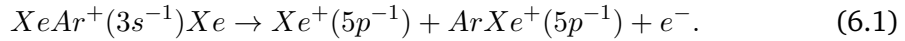
The first parts of this chapter addressed the formation and structure of the mixed species by comparing outer valence spectra of the mixed and the homogeneous clusters. Here, I showed that the clusters produced were mixed, which is a prerequisite for the occurrence of ETMD. In addition, several other interesting aspects of the formation of the mixed clusters were discussed. The outer valence spectra of both species in the mixed clusters are blue shifted compared to the spectra from the homogeneous species. Lundwall *et al.* found that co-expanded Ar-Kr clusters consist of "mainly argon on the surface and dominantly krypton in the bulk" [54]. I was not able to detect bulk contributions in the argon part of the spectra. The Ar 3s spectra indicate that the argon atoms are found mostly on surface sites with a small coordination number. With high krypton content in the initial gas mixture, the outer valence spectra of the Kr 4p band broadens and a contribution from the bulk can be distinguished. The argon content in the final clusters then implies that the clusters produced are very small, in the case of the initial mixture with 3 % krypton, and large, in the case with 10 % krypton. Another explanation for the observations is that the cluster is strongly amorphous, i.e. it is very hot and the interatomic distances are high. This, again, is very unlikely because clusters which are produced via co-expansion are known to be very cold [142].

I also used the site dependency of ETMD to explain a shift in the binding energy of the Ar 3s derived cluster band observed in the mixed cluster spectra, by comparing the spectra of primary electrons which lead to autoionization to the spectra of those which do not autoionize. This finding already represents one application of ETMD. The ratio of atoms which do not autoionize compared to atoms that do, gives us the ratio of argon atoms on surface sites with small coordination numbers compared to the argon atoms which are somewhat embedded in the krypton matrix. In the experiment using the 3 % mixture, almost 70 % of the argon atoms did not autoionize. In case of the 10 % mixture approximately all argon atoms autoionized.

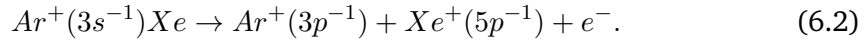
The experiments described here provide the first experimental evidence of ETMD(3). We published some of the findings presented here in reference [139]. Around the same time, an experimental evidence of ETMD(2) was provided by Sakai *et al.* [143]. Hoener *et al.* measured ionic spectra of large Ar-Xe clusters after photoionization. They found traces which require an efficient charge transfer [144]. ETMD could be such a mechanism.

6 ICD and ETMD in mixed Ar-Xe clusters

Like the Ar-Kr₂ trimer, the Ar-Xe₂ trimer can decay via ETMD [10]:



While in the case of Ar-Kr₂, ETMD is energetically only possible if the two krypton atoms are a certain distance apart, there is no geometrical restriction on ETMD in the case of the Ar-Xe₂ trimer. In contrast to large Ar-Kr clusters, in larger Ar-Xe clusters, ICD may also occur [10]:



This chapter presents experiments made on mixed Ar-Xe clusters of different sizes and compositions to identify the expected ICD and ETMD features. Here, for the first time, we have systematically varied the mixing ratio of argon and xenon and have systematically determined the cluster structure using outer valence spectra. Electron-electron coincidence maps will be used to identify and specify the ICD and the ETMD features. In an earlier work, Mucke [11] presented a different dataset of coincidence maps after photoionization of Ar-Xe clusters to discuss the same questions. However, due to a smaller range of mixing ratios and expansion parameters, as well as the absence of outer valence spectra, it was not yet possible to draw final conclusions on the co-occurrence of ICD and ETMD in that work.

In the trimer Ar-Xe₂, ETMD is expected because no other non-radiative decay mechanism is energetically allowed. Fasshauer *et al.* found that in large Ar-Xe clusters, ICD becomes energetically possible. They write that "with the appearance of xenon atoms in the third coordination shell around Ar, ICD processes of the Ar 3s⁻¹ hole involving these Xe atoms become energetically possible" [10]. They argue that two scenarios are possible. Either the ICD efficiency exceeds the ETMD efficiency significantly and ICD becomes the dominant decay or the processes compete and signatures of both can be observable experimentally. Very recent calculations by Fasshauer *et al.*, made for large Ar-Xe clusters, predict total decay rates of 4.5 * 10⁻⁴ eV for ICD and 4.9 * 10⁻⁴ eV for ETMD [145]. This means that both decays have comparable lifetimes of approximately 1.4 ps.

6.1 Outer valence spectra of mixed Ar-Xe clusters

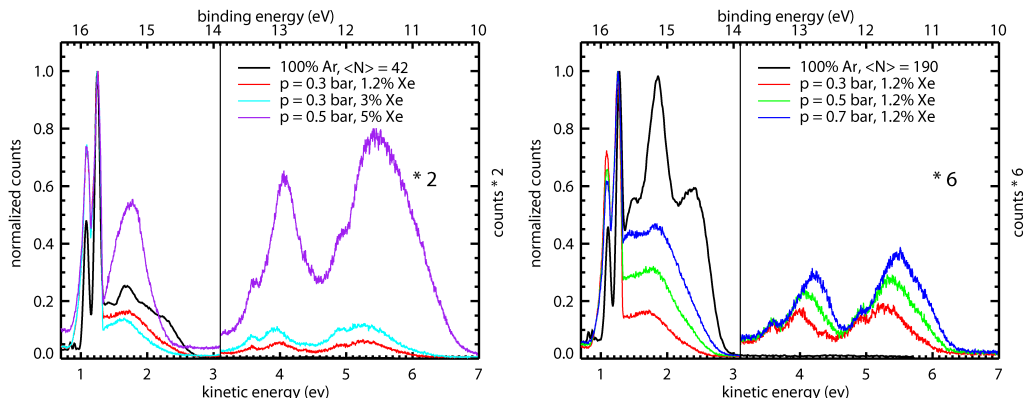


Figure 6.1: Outer valence spectra of small homogeneous argon clusters (left panel, black line), medium-sized homogeneous argon clusters (right panel, black line) and mixed Ar-Xe clusters at varying mixing ratios (left panel) and varying expansion pressures (right panel). The spectra were normalized to the Ar $3p_{3/2}$ monomer line. For clarity, the part with kinetic energies above 3.1 eV was scaled according to the factor given in the respective figures. All spectra were recorded at an excitation energy of 17.0 eV.

Figure 6.1 shows outer valence spectra of homogeneous argon clusters and of Ar-Xe clusters with different mixing ratios and expansion pressures. The parameters relevant to the discussion are summarized in table 6.1. They were obtained using Gaussian fits of the spectra. Figure 6.2 shows an example of such a fit. Rolles *et al.* used more sophisticated fits, with the assumption that there is a bulk-surface splitting and an additional splitting into magnetic sub-levels for the xenon cluster contributions.

It can be seen that a wide variety of cluster sizes and of Ar/Xe ratios in the mixed clusters was achieved. The Ar $3s$ derived cluster bands from the heterogeneous species are approximately 50 % to 100 % as wide as the bands from the homogeneous species (also compare figure 5.2). The bands narrow with increasing xenon content in the cluster and widen slightly with increasing expansion pressure. The aforementioned dispersing feature clearly dominates the spectrum of the medium sized homogeneous argon clusters and is also present in the spectrum of the small homogeneous argon clusters. It is not present in any of the spectra of the heterogeneous species.

Outer valence spectra of the homogeneous xenon clusters were not measured in this experiment. Comparisons to measurements made by Feifel *et al.* [132] and Rolles *et al.* [133] show that the widths of the xenon cluster bands in the mixed species reaches those from the homogeneous species with a size between $\langle N \rangle = 500$ and $\langle N \rangle = 1000$. In the spectra with a low xenon content in the initial gas mixture, it can be seen that

Table 6.1: Summary of the parameters extracted from the outer valence spectra shown in figure 6.1. Values for homogeneous xenon clusters have been taken from [132]. They represent xenon clusters with a size of $\langle N \rangle = 1000$. All other values were estimated using Gaussian fits of the respective spectral features. The xenon content in the clusters was determined from the areas of the argon and xenon cluster contributions in the outer valence spectra. These areas were then corrected using the respective atomic cross-sections of $\sigma_{Ar}(17eV) = 33.0Mb$ and $\sigma_{Xe}(17eV) = 51.3Mb$ [146]. The uncertainty of the xenon content is in the order of 3%. Energy values are in eV. E_b is given as the position in binding energy of the maximum of a Gaussian fit of the cluster band feature. ΔE is the FWHM of the Gaussian fit of the respective cluster feature. For xenon, only the width and position of the Xe $5p_{3/2}$ cluster feature were evaluated. Uncertainties of the energy values are approximately $\pm 0.1eV$ according to the resolution of the spectrometer. * xenon content in the initial gas mixture, ** xenon content in the cluster as derived from the outer valence spectra.

%Xe*	T/K	p_{stag}/bar	$\langle N \rangle$	%Xe**	$E_b(Ar)$	$\Delta E(Ar)$	$E_b(Xe)$	$\Delta E(Xe)$
0	96.5	0.35	42	0	15.3	1.1		
0	96.5	0.67	190	0	15.1	1.3		
1.2	174	0.3		12	15.40	0.9	11.7	0.85
1.2	174	0.5		11	15.31	1.0	11.6	0.85
1.2	174	0.7		10	15.26	1.1	11.5	1.08
3.0	174	0.3		29	15.40	0.8	11.8	1.02
5.0	174	0.5		53	15.27	0.6	11.5	1.24
100	178	1.5	1000	100			11.1	1.2

the width of the Xe $5p_{3/2}$ derived band increases with increasing expansion pressure and the binding energy shifts to smaller values.

It is expected that Ar-Xe clusters produced via co-expansion will form a xenon core surrounded by an argon layer [53, 57]. All the spectra shown here are consistent with this expectation. Measurements made with a low xenon content in the initial gas mixture indicate a very small xenon core. The number of atoms in this core increases with increasing pressure, and with increasing xenon content in the initial gas mixture.

The Ar $3p$ derived band in the mixed clusters ranges in width from narrower to slightly broader than that of the homogeneous argon clusters with a size of $\langle N \rangle = 42$. It is, however, always narrower than that of argon clusters with a mean size of $\langle N \rangle = 190$. Additionally, a dispersing feature is never present in the spectra from the mixed species.

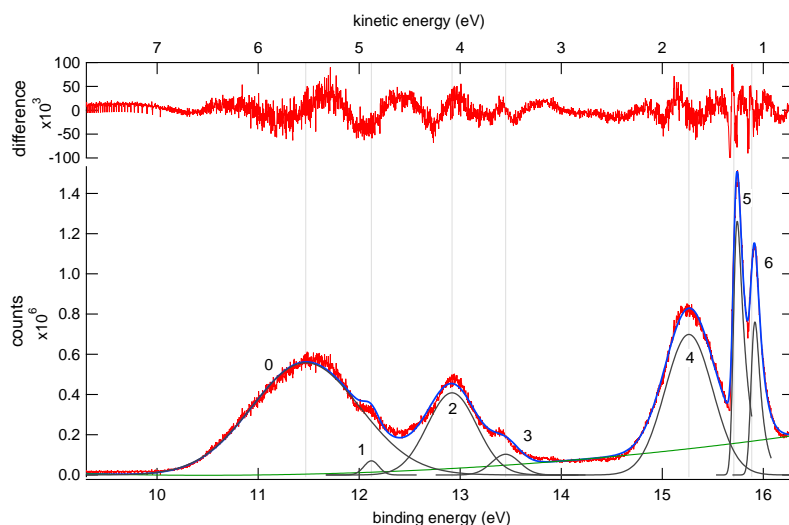


Figure 6.2: Figure illustrating the type of fit used for the analysis of the cluster composition based on outer valence photoelectron spectra (see table 6.1). Shown here is an outer valence spectrum of Ar-Xe clusters with an initial mixing ratio of 5 % xenon at an expansion pressure of 0.5 b. The green solid line shows a background which also was a fit parameter. The red line shows the measured spectrum, the solid blue line is the total fit and the labeled grey lines are the single fitted peaks: 0 - Xe cluster $5p_{3/2}$, 1 - Xe monomer $5p_{3/2}$, 2 - Xe cluster $5p_{1/2}$, 3 - Xe monomer $5p_{1/2}$, 4 - Ar cluster $3p$, 5 - Ar monomer $3p_{3/2}$, 6 - Ar monomer $3p_{1/2}$. The red line on top shows the difference between the fit and the measured spectrum. The area of peak 1 should be larger than that of peak 3 [147]. The discrepancy in the fit may be a result of a poor background subtraction in the region between 14 eV to 12 eV binding energy.

6.2 Inner valence spectra of mixed Ar-Xe clusters

Figure 6.3 shows the Ar $3s$ cluster and monomer contributions in the photoelectron spectra of mixed Ar-Xe clusters and of large homogeneous argon clusters. The three selected spectra from the heterogeneous species represent the maximum range of FWHM of the Ar $3s$ band that was measured. The FWHM of the Ar $3s$ cluster feature only changes by approximately 0.2 eV. The spectrum of the homogeneous species was recorded at TGM4. However, the energy resolution of the spectra is comparable because the width of the monomer lines is almost identical. A non-linear background was subtracted in order to make a comparison easier. Both, events with one electron hit and events with two electron hits are included in the spectra shown. Also shown in the right panel is the part of the spectrum which results from events with only one electron. It can be seen that the electrons from the monomer do not lead to the emission of a second electron, while most cluster Ar $3s$ cluster band vacancies autoionize.

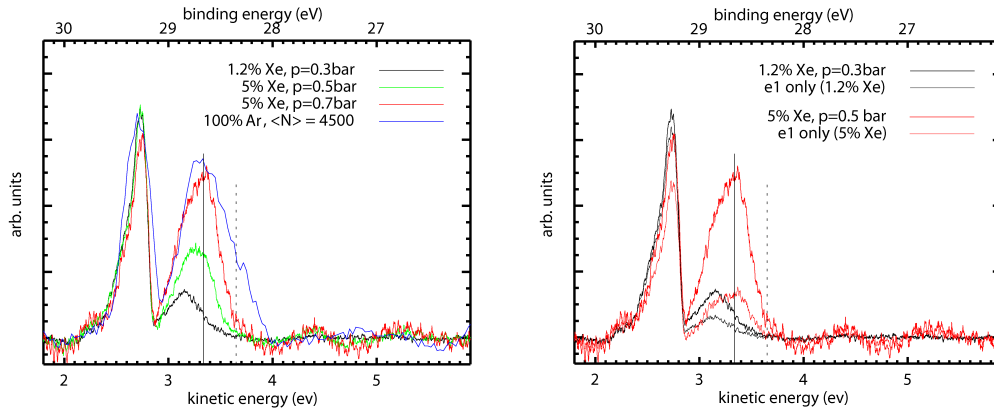


Figure 6.3: Comparison of three Ar-Xe inner valence spectra in the Ar $3s$ binding energy region with a spectrum from the homogeneous species (left panel), all taken at 32 eV. A non-linear background was subtracted. The right panel shows the same spectra of two selected clusters in comparison with the part of the spectrum which is caused by events with only one hit, these are the vacancies which do not autoionize (or the coincident electron was not recorded). The full spectra of the homogeneous species (without background subtraction) was already shown in the left panel of figure 5.3. The Ar-Xe spectrum was recorded at UE112, the homogeneous argon spectra at TGM4. Vertical lines indicate the positions of the bulk contribution (dashed) and surface contribution (solid) maxima of argon clusters with a mean size of $\langle N \rangle = 1000$ found by Feifel *et al.* [132].

The spectra also show that the Ar $3s$ feature of the mixed cluster is narrower and blue shifted compared to that of the homogeneous species. Its width increases with increasing pressure and xenon content. Marked with horizontal lines are the maxima of the Ar $3s$ bulk (dashed) and surface (solid) contributions as measured by Feifel *et al.* on clusters with a mean size of $\langle N \rangle = 1000$ [132]. The black spectrum has its maximum at binding energies smaller than the binding energy of the surface contribution of the homogeneous species. The red spectrum, which was taken at highest expansion pressures and highest xenon content, is narrower than the spectrum of the homogeneous species. Its maximum, however, is in the region of the surface contribution of the homogeneous species. The results confirm and refine the findings which were obtained from the outer valence spectra. The argon atoms are sitting on a surface made of xenon atoms. An interface layer gives rise to the black spectrum in figure 6.3. The green spectrum then shows contributions from an argon surface layer and an interface layer. The increased width of the red spectrum compared to the green spectrum indicates that a bulk layer may be present. This means that, in the shown cases, the clusters consist of a xenon core surrounded by one to three layers of argon. With the measured Ar/Xe

content in the clusters and the assumptions about the number of argon layers, one can easily estimate the total cluster size and the xenon content of the clusters.

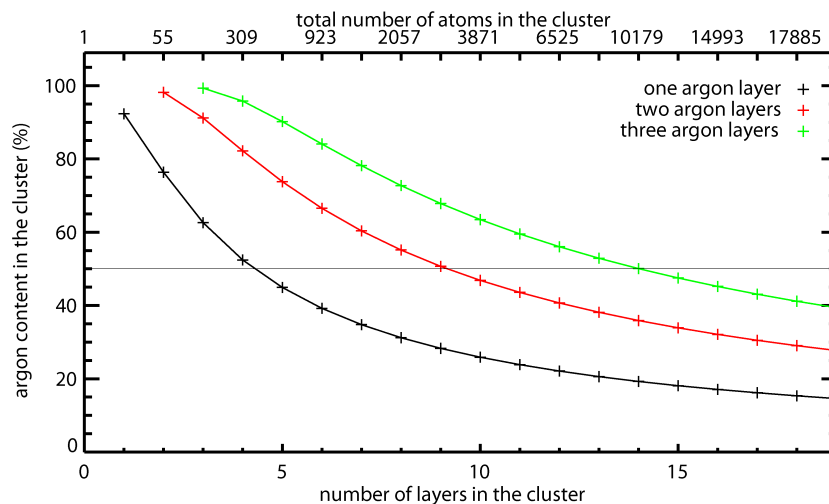


Figure 6.4: Percentage of argon atoms in an Ar-Xe cluster with a xenon core (of at least one atom) versus the total number of layers of the cluster. The number of atoms per layer is estimated using equation 2.6. A horizontal line is drawn where the number of argon atoms in the cluster equals the number of xenon atoms.

Figure 6.4 shows theoretical argon to xenon ratios which were calculated assuming icosahedral clusters and one, two and three argon layers, respectively, around a xenon core. The Ar $3p$ cluster spectrum with 5 % xenon in the initial gas mixture and an expansion pressure of 0.5 bar is narrow. The Ar/Xe ratio in the cluster is 0.9 (47 % Ar), the Xe $5p$ spectrum is comparable to that of large homogeneous clusters and the Ar $3s$ spectrum shows no bulk contribution. Using figure 6.4, I can estimate that with two argon layers (one interface, one surface), an argon content of 47 % is achieved with a xenon core consisting of approximately 2000 atoms. That is a xenon core with 8 layers.

The outer valence spectra, measured with a xenon content in the initial gas mixture of 1.2 % and an expansion pressure of 0.3 bar indicate that both argon and xenon atoms can be found on surface sites and interface sites only. The amount of argon in the clusters was measured as approximately 88 %. Comparing with figure 6.4 and assuming two argon layers, the cluster size can be estimated to be in the range of 150 to 310 atoms and therefore the number of xenon atoms is less than 55.

6.3 Electron-electron coincidence spectra of Ar-Xe clusters

The expected kinetic energies of the ICD and the ETMD electrons can be estimated as described in detail in the previous chapter. Using equation 2.21 and the ionization potentials presented in the previous section, one can calculate the minimum distance required for ICD to be approximately 5.8 \AA . At this distance, the kinetic energy of the ICD electron is zero. Larger distances yield ICD electrons with kinetic energies above 0 eV.

ETMD(3) is possible whenever the argon atom has two xenon neighbors. Using equation 2.21, a Xe $5p$ electron binding energy range of 10.8 eV to 12 eV, and a distance between two xenon atoms of 3.9 \AA (according to table 2.2), the expected kinetic energy range of the ETMD electron can be calculated as 1.0 to 3.4 eV.

In order to distinguish between these two processes, we have created electron-electron coincidence maps of our measurements. An electron-electron coincidence map of homogeneous argon clusters was shown in the previous chapter (figure 5.5). A coincidence map of homogeneous xenon clusters is shown in the left panel of figure 6.5. Neither map shows a structured feature in the energy region of the Ar $3s$ cluster electron. This is expected because, in the case of xenon, no initial states exist in that region and, in the case of homogeneous argon clusters, Ar $3s$ cluster vacancies cannot autoionize.

The right panel in figure 6.5 and both panels in figure 6.6 show electron-electron coincidence maps of heterogeneous Ar-Xe clusters at several different expansion pressures and mixing ratios of the initial gas. All maps show a strong signal in the energy region of the Ar $3s$ cluster binding energies. These regions are marked by two horizontal black lines.

In the maps, the a)-panels show the total number per energy interval of the e_2 electrons within the region marked by the horizontal black lines. This is the kinetic energy spectrum of secondary electrons emitted in coincidence with primary electrons which had binding energies in the region of the Ar $3s$ cluster band. The c)-panels show the total number per energy interval of the e_1 electrons along the kinetic energy interval of e_2 . This is the binding energy spectrum of all primary electrons that contributed to the emission of secondaries.

Apart from coincidences in the binding energy region of the Ar $3s$ cluster line, the maps show coincidences between primary electrons in the whole binding energy region and secondary electrons with energies below approximately 0.4 eV kinetic energy. This broad feature gains intensity with increasing expansion pressure and xenon content in the initial gas mixture. Following the reasoning of the previous chapter, a likely explanation for this broad feature is intracluster electron-electron scattering of electrons from the Xe $5p$ and Ar $3p$ derived cluster bands. Available kinetic energies for the

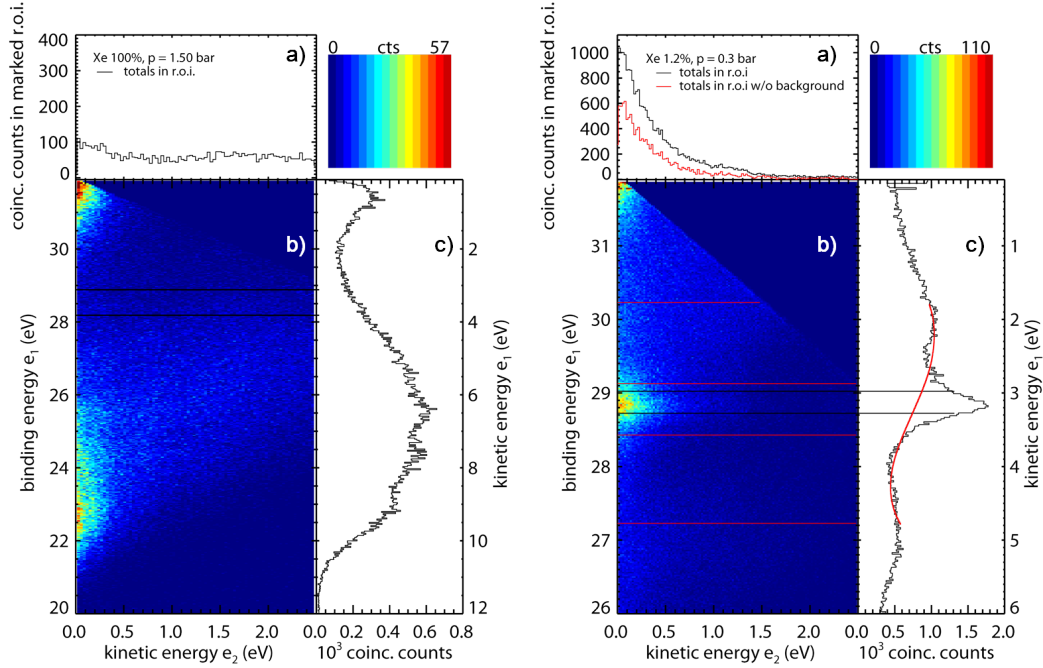


Figure 6.5: Electron-electron coincidence maps after photoionization of xenon clusters (left) and mixed Ar-Xe clusters (right) at $h\nu = 32$ eV. In both maps, the black horizontal lines in the b)-panels mark the binding energy region of the Ar 3s derived cluster band. The c)-panels show the projection of all counts onto the axis of e_1 . This projection corresponds to the binding energy spectrum of all primary electrons that contribute to the emission of secondaries. The a)-panels show the projection of all counts within the marked region in the b)-panels onto the axis of e_2 . This is the kinetic energy spectrum of secondary electrons emitted in coincidence with primary electrons which have binding energies in the region of the Ar 3s cluster band. Intensity is given as events per pixel, with a pixel width of 20 meV x 20 meV. In the right map, two regions are marked by red lines in the b)-panel. These regions were used to estimate the background. For each kinetic energy interval of e_2 , a fit was made which connects these two regions. The difference between this fit and the total spectrum in the Ar 3s energy interval is shown in red in the a)-panel. To obtain an estimate of the quality of these fits, the sum of all fits is shown in red in the c)-panel.

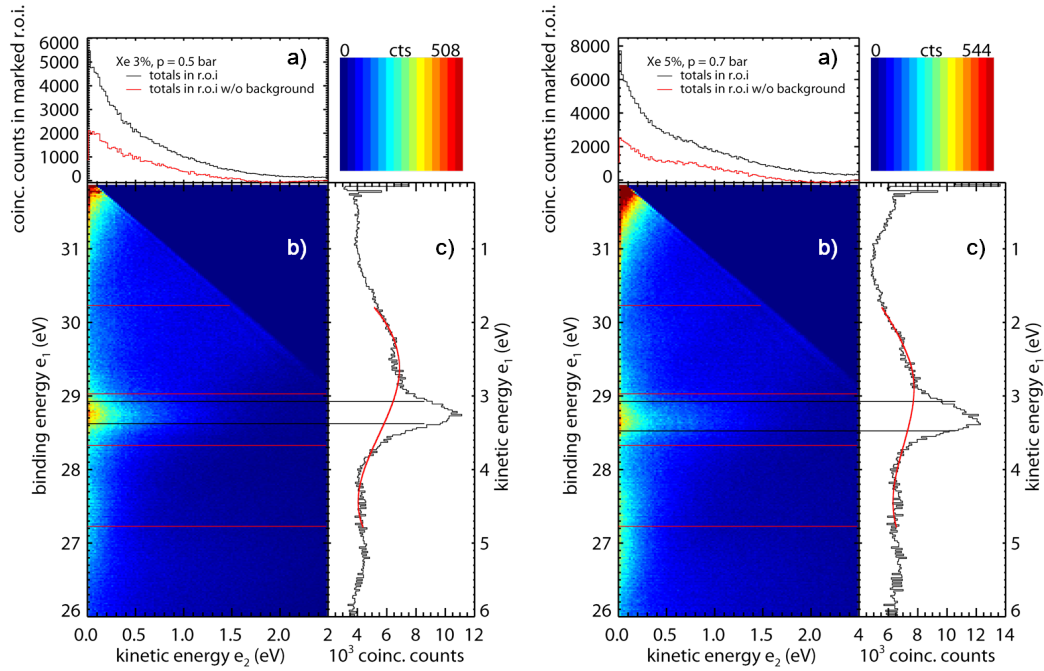


Figure 6.6: Electron-electron coincidence spectra after photoionization of Ar-Xe clusters with varying mixing ratios and varying expansion pressures taken at $h\nu = 32$ eV. Details are explained in the text and in the caption of figure 6.5

resulting electron pairs are in the range of 0 eV to 5 eV for Ar $3p$ - Xe $5p$ scattering and 2 eV to 8 eV for Xe $5p$ - Xe $5p$ scattering.

At e_1 binding energies above 31 eV and with kinetic energies of e_2 below 0.5 eV, a strong feature is seen in all spectra. A similar feature is present in the map of the homogeneous argon clusters. Again, for the same reasons described in the last chapter, this broad feature can be explained as Ar $3p$ - Ar $3p$ intracluster electron-electron scattering of the Ar $3p$ outer valence bands.

In order to derive a kinetic energy spectrum of only those secondary electrons which come from autoionization of vacancies of the Ar $3s$ cluster band, an estimate of the broad feature has to be subtracted. For the estimate, I used the two regions marked by red lines in the b)-panels. For each e_2 energy interval, these two regions were connected using a polynomial fit. This fit then provided the estimate of the background in the region marked by two horizontal black lines. The area of the resulting spectrum within the two horizontal black lines in the respective e_1 energy interval was then calculated and plotted in red in the a)-panels. The c)-panels show the sum of all of these fits as a red line.

Figure 6.7 shows the kinetic energy spectra of the e_2 electrons from three different

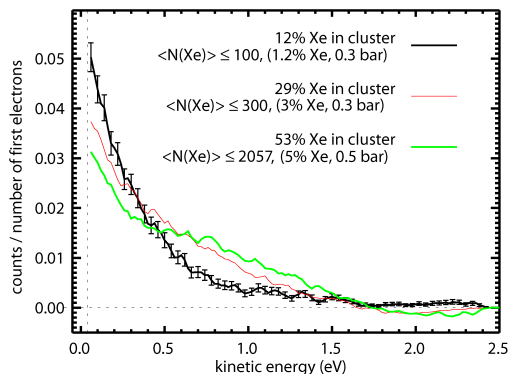


Figure 6.7: Kinetic energy spectra of e_2 electrons after background subtraction, normalized to the number of all coincident e_1 electrons in the Ar $3s$ cluster region. The number of xenon atoms in the clusters was estimated using figure 6.4 and the respective xenon contents in the cluster. Additionally, it was assumed that two argon layers were present in the black and red spectra and three argon layers in the green spectrum (apart from the normalization, these spectra are the same as those shown in red in the a-panels of the coincidence maps). Error bars are included for every second data point of one of the spectra. They were calculated using the weighted sum of the statistical error of the subtracted background and the statistical error of the spectra before subtraction of a background.

expansion parameters in more detail and in comparison with one another. The spectra are normalized to the number of all recorded e_1 electrons in the Ar $3s$ region which result in the emission of secondaries. The total areas of the normalized spectra in the kinetic energy range shown are 0.91, 0.96 and 0.94, for the black, red and green lines, respectively. This means that only a very small fraction of electrons are not considered in the kinetic energy range shown, most of which can be found in the kinetic energy region below 0.05 eV. This region was excluded from the plot of secondary electrons because a time-to-energy conversion cannot be made reliably at these low kinetic energies. Because the calculated areas are almost equal to one, it can reasonably be assumed that there were no electrons with kinetic energies above 2.5 eV.

The normalization also shows that the kinetic energy spectra of the secondary electrons consist of two parts. With increasing xenon content and increasing cluster size, the spectra develop an increasingly pronounced shoulder at kinetic energies above 0.5 eV, while a decreasing number of Ar $3s$ vacancies decay via emission of electrons below 0.4 eV.

As explained earlier in this chapter, ICD can only occur if the distance between the participating argon and xenon atom is at least 5.8 \AA . At this distance, the expected

kinetic energy of the ICD electron is zero, and with increasing distance, it increases, while the decay width of ICD decreases proportionally to R^{-6} . ETMD is only possible if the argon atom has a xenon atom as a direct neighbor and a second xenon atom in close vicinity. In an Ar-Xe cluster, this can only be the case in the interface layer. The kinetic energy of the ETMD electron is expected to be in the range of 1.1 eV to 3.1 eV.

By looking at the structure and composition of the clusters with an Ar/Xe ratio of 7.5 (1.2 % xenon in the initial gas mixture and an expansion pressure of 0.3 bar), I have arrived at the conclusion that these clusters have approximately two argon layers around a core of three xenon layers. This is a core of 55 xenon atoms. These hypothetical clusters have 92 argon atoms which each have two nearest neighbors of xenon. This means, that they have 92 atoms at sites where ETMD is allowed. The minimum distance for ICD to occur is above 5.8 Å. This means that the participating argon and xenon atoms have to be separated by at least one cluster layer. Therefore, our hypothetical clusters each have 254 argon atoms which can decay via ICD (i.e. all the argon atoms, since the cluster is assumed to have five layers, with the two outer layers consisting of argon atoms). These numbers are estimated based on the assumption that the cluster structure has no defects, which is unlikely, especially in the interface layer, because the argon and xenon atoms have different sizes. However, if both decays have the same decay width, these estimates allow us to calculate the maximal expected ICD to ETMD ratio to be 2.8.

With increasing cluster size, this ratio decreases, approaching 2 (assuming two or more argon layers). I estimated the number of xenon atoms in clusters made with an initial gas mixture of 5 % xenon at 0.5 bar expansion pressure to be approximately 2057. Assuming two argon layers, this gives 812 argon atoms which could decay via ETMD and 1820 which could decay via ICD. This is a ratio of 2.2.

With this information, interpreting the spectra shown in figure 6.7 is now straightforward. The black spectrum shows mainly ICD electrons. In these very small clusters, with a small xenon core and a high argon content, relatively few argon atoms have two xenon neighbors. Therefore, most Ar 3s vacancies can only decay via ICD. With increasing cluster size and Ar/Xe ratio, this changes, and the ratio of possible ICD sites to possible ETMD sites becomes smaller. The green spectrum, from clusters with a large xenon core and only a few argon layers, shows increased intensity above approximately 0.4 eV kinetic energy, compared to the spectra of smaller clusters, while the intensity in the region pertaining to very slow electrons decreases. I identify this new feature in the spectrum as contributions from ETMD electrons. It has kinetic energies in the range of 0.4 eV to 1.5 eV. The expected range is higher. It was, however, estimated using only the Xe 5p_{3/2} contributions. Additionally, only xenon atoms in the interface layer are possible ETMD sites. These sites probably contribute to the part of lower binding energies in the spectrum measured of the whole cluster. These are two reasons why the

energy range of the ETMD electron is somewhat smaller than calculated.

6.4 Conclusions

In summary, I have presented inner and outer valence spectra of small to medium-sized, mixed Ar-Xe clusters. By comparing the widths of the inner and outer valence cluster bands to those from the homogeneous species, and to previously published values, I have shown that the clusters form a xenon core surrounded by two to three argon layers. Using, additionally, the number of atoms per layer in a full icosahedron (calculated with equation 2.6) and the argon to xenon ratio (determined using the outer valence spectra), I have estimated the total cluster size.

I have presented electron-electron coincidence maps of mixed Ar-Xe clusters and of the homogeneous species. Only maps of the mixed species show a feature in coincidence with the Ar 3s-derived cluster band. After subtracting coincidences from other double-ionization processes, I have presented kinetic energy spectra of secondary electrons generated by autoionization of Ar 3s cluster vacancies. Those secondary electrons were found to have kinetic energies in the range between 0.0 eV to 1.7 eV. With changing cluster size, the spectral shape changes. In larger clusters, more Ar 3s vacancies decay via the emission of faster electrons. I interpreted this phenomenon as competition between ICD and ETMD.

By comparing the number of geometrically available Ar 3s vacancies which can decay via ICD to the number which can decay via ETMD, I have shown that, even though the decay rates of ICD and ETMD in this system are almost identical, ICD is always at least twice as probable as ETMD if more than one argon layer is present. For very small clusters, this ratio changes, and ICD becomes more likely due to the much higher availability of decay partners. This competition is reflected in the kinetic energy spectra of the secondary electrons.

The results of the experiments presented are very interesting. The ICD rate is strongly enhanced when the decay partners are neighbors, i.e. their outer valence orbitals overlap. In earlier experiments, this was always the case ([4] and references therein). Here, however, ICD is found in a system in which the participating atoms are so far apart that there can be no orbital overlap. The decay width of ICD is strongly decreased, but nevertheless, ICD is still the most efficient decay channel. Also, until now, it was believed that as long as ICD is possible, ETMD cannot take place. This is still the case in systems where there is an orbital overlap of the ICD participants, because the decay width of ETMD is several orders of magnitude smaller. Here, however, the two processes compete. The decay width of ETMD is still very small but the large distances between the possible ICD sites results in a strongly decreased ICD decay width.

7 Summary and Outlook

This work documents and discusses my experiments on homogeneous and inhomogeneous rare gas clusters. The main focus of this work lies in the investigation of a novel autoionization process termed *ETMD(3)*. It presents two systems which exhibit *ETMD(3)*. Here, I will give a brief summary of the most important results.

ETMD in mixed Ar-Kr clusters

Mixed Ar-Kr clusters were produced using supersonic co-expansion of a mixture of argon and krypton. Outer and inner valence spectra of the resulting mixed clusters are presented. I confirm that the clusters produced are mixed and I have determined the ratios of the composition of the final clusters using outer valence spectra. The electron-electron coincidence spectra of the mixed species show two features. One is broad and unstructured and is attributed to intracluster electron-electron scattering of electrons from the outer valence orbitals. There is also a sharp feature of low kinetic energy in coincidence with the Ar $3s$ derived cluster band. I identify this feature due to coincidences between the Ar $3s$ photoelectron and the expected *ETMD(3)* electron. I present the kinetic energy distribution of the *ETMD(3)* electron. It has its maximum at kinetic energies below approximately 0.1 eV and its maximum kinetic energy at approximately 1.0 eV.

ICD and ETMD in mixed Ar-Xe clusters

Mixed Ar-Xe clusters were produced via co-expansion. Outer and inner valence spectra are presented. I show that, in agreement with results from Lundwall *et al.* [54, 55], the clusters consist of a xenon core surrounded by argon. Based on a measurement of the argon and xenon content in the final clusters and reasonable assumptions about the number of argon layers, based on the outer and inner valence spectra, I give an estimate of the size of the clusters. Electron-electron coincidence maps are presented. They show a strong feature in the binding energy region of the Ar $3s$ derived cluster band. I show that this feature results mainly from ICD in the case of clusters with very small xenon cores and a large argon content. With increasing size of the xenon core, the kinetic energy distribution changes and contributions at higher kinetic energies are seen. I show that this behavior is caused by the co-occurrence of ICD and *ETMD*.

Outlook

There is already a long list of publications addressing ETMD and especially ICD. Nevertheless, research in this field is just starting. Very recently, funding for a new DFG research unit on ICD was granted [148]. The funding proposal for that research unit identifies the main questions, that future ICD research has to address: which physical and chemical parameters have the strongest influence on ICD, in which systems does ICD occur, how can ICD be employed as a method in chemical research, what are the biochemical implications of ICD and what is the time evolution of ICD [149]? This work represents only a small contribution to answering those questions, but the techniques developed and the experience gained can still provide much more to them. I believe that this thesis (and other related publications) show that electron-electron coincidence spectroscopy, in combination with a magnetic bottle electron TOF spectrometer, is a powerful tool for investigating complex systems exhibiting ETMD or ICD. Biomolecules solvated in liquid jets or water clusters are very interesting targets, for example. Though this is only speculation at this time, it may also be possible someday to trigger so far inaccessible chemical reactions using ICD and ETMD.

I also see the potential for improving technical and experimental aspects. An increase in the energy resolution of the magnetic bottle would be beneficial especially at high kinetic energies. The use of electrostatic lenses and a variable potential within the drifttube could yield improvements. And, finally, with the possibility to observe the structure of single clusters using new generation light sources (FELs), many interesting pump-probe experiments on size-selected and structure-selected clusters can be made.

Outer-valence spectra of argon and krypton

Apart from using the outer valence spectra of homogeneous argon and krypton clusters as a tool for the size and structure determination of the mixed species, I showed that they exhibit properties which allow to determine the onset of bulk-like behavior of the clusters. I presented outer valence spectra of small to large argon and krypton clusters, measured at a series of excitation energies close to the photoionization threshold. The cluster size dependency of the width of the valence band was determined. In addition to the broad cluster band, the spectra exhibit a strong feature with a FWHM of approximately 0.25 eV for both species. This feature shifts in binding energy with changing excitation energy. The observed shift is approximately 0.6 eV in the case of argon clusters and 0.25 eV in the case of krypton clusters. These features are also visible in spectra of crystalline and polycrystalline rare gas solids [69, 128]. I discuss these features in terms of electronic band dispersion of the valence band. The dispersion reaches its full extent (compared to large clusters) in argon clusters with a size of

approximately 230 atoms and in krypton clusters with a size below approximately 270 atoms.

In order to draw more precise conclusions on the onset of bulk-like behavior with respect to the cluster size, a sharper discrimination of the cluster sizes is desirable. Electron-ion coincidence spectroscopy using the magnetic bottle, combined with a reflectron mass spectrometer, could yield very interesting results in this respect. Arguably, no experiment so far had the power to discriminate at which size a certain cluster develops properties that are genuine only to the infinitely, ordered crystal lattice of the solid. For this reason, a continuation of the experiments shown here is very promising.

Bibliography

- [1] Aristotle. *Metaphysics VIII 1045a 8-10* (cit. on p. 1).
- [2] L. S. Cederbaum, J. Zobeley, and F. Tarantelli. “Giant Intermolecular Decay and Fragmentation of Clusters”. In: *Phys. Rev. Lett.* 79.24 (1997), pp. 4778–4781. DOI: [10.1103/PhysRevLett.79.4778](https://doi.org/10.1103/PhysRevLett.79.4778) (cit. on pp. 1, 23–25).
- [3] J. Zobeley, R. Santra, and L. S. Cederbaum. “Electronic decay in weakly bound heteroclusters: Energy transfer versus electron transfer”. In: *J. Chem. Phys.* 115.11 (2001), pp. 5076–5088. DOI: [10.1063/1.1395555](https://doi.org/10.1063/1.1395555) (cit. on pp. 1, 2, 26).
- [4] U. Hergenhahn. “Interatomic and intermolecular coulombic decay: The early years”. In: *J. Electron Spectrosc. Relat. Phenom.* 184 (2011), pp. 78–90. DOI: [10.1016/j.elspec.2010.12.020](https://doi.org/10.1016/j.elspec.2010.12.020) (cit. on pp. 1, 24, 25, 94).
- [5] V. Averbukh, Ph.V. Demekhin, P. Kolorenc, S. Scheit, S.D. Stoychev, A.I. Kuleff, Y.-C. Chiang, K. Gokhberg, S. Kopelke, N. Sisourat, and L.S. Cederbaum. “Interatomic electronic decay processes in singly and multiply ionized clusters”. In: *J. Electron Spectrosc. Relat. Phenom.* 183.1 (2011), pp. 36–47. DOI: [10.1016/j.elspec.2010.03.003](https://doi.org/10.1016/j.elspec.2010.03.003) (cit. on p. 1).
- [6] M. Pernpointner, N. V. Kryzhevoi, and S. Urbaczek. “Possible electronic decay channels in the ionization spectra of small clusters composed of Ar and Kr: A four-component relativistic treatment”. In: *J. Chem. Phys.* 129.2, 024304 (2008), p. 024304. DOI: [10.1063/1.2952272](https://doi.org/10.1063/1.2952272) (cit. on pp. 1, 2, 19, 27, 28, 67, 78).
- [7] M. Lundwall, W. Pokapanich, H. Bergersen, A. Lindblad, T. Rander, G. Öhrwall, M. Tchapyguine, S. Barth, U. Hergenhahn, S. Svensson, and O. Björneholm. “Self-assembled heterogeneous argon/neon core-shell clusters studied by photoelectron spectroscopy”. In: *J. Chem. Phys.* 126.21, 214706 (2007), p. 214706. DOI: [10.1063/1.2735607](https://doi.org/10.1063/1.2735607) (cit. on p. 1).
- [8] M. Mucke, M. Braune, S. Barth, M. Förstel, T. Lischke, V. Ulrich, T. Arion, U. Becker, A. M. Bradshaw, and U. Hergenhahn. “A hitherto unrecognized source of low-energy electrons in water”. In: *Nature Phys.* 6 (2010), pp. 143–146. DOI: [doi:10.1038/nphys1500](https://doi.org/10.1038/nphys1500) (cit. on pp. 1, 3, 25, 51).

- [9] I. B. Müller and L. S. Cederbaum. “Electronic decay following ionization of aqueous Li^+ microsolvation clusters”. In: *J. Chem. Phys.* 112 (2005), p. 094305. DOI: [10.1063/1.1854118](https://doi.org/10.1063/1.1854118) (cit. on pp. 2, 28).
- [10] E. Fasshauer, N. V. Kryzhevoi, and M. Pernpointner. “Possible electronic decay channels in the ionization spectra of small clusters composed of Ar and Xe: A four-component relativistic treatment”. In: *J. Chem. Phys.* 133.1 (2010), p. 014303. DOI: [10.1063/1.3462246](https://doi.org/10.1063/1.3462246) (cit. on pp. 2, 83).
- [11] M. Mucke. “Employing electron-electron coincidence techniques to investigate the autoionisation of clusters”. PhD thesis. TU Berlin, 2011 (cit. on pp. 3, 39, 44, 83).
- [12] C. Domesle, B. Jordon-Thaden, L. Lammich, M. Förstel, U. Hergenhahn, A. Wolf, and H.-B. Pedersen. “Photoelectron spectroscopy of O^- at 266 nm: Ratio of ground- and excited-state atomic oxygen production and channel-resolved photoelectron anisotropy parameters”. In: *Phys. Rev. A* 82.3 (2010), p. 033402. DOI: [10.1103/PhysRevA.82.033402](https://doi.org/10.1103/PhysRevA.82.033402) (cit. on pp. 3, 45).
- [13] C. Domesle. “Momentum imaging of photofragments and photoelectrons using fast ion beams”. PhD thesis. Universität Heidelberg, 2012 (cit. on pp. 3, 45).
- [14] URL: http://hasylab.desy.de/annual_report/files/2009/2009771.pdf (visited on 05/23/2012) (cit. on p. 3).
- [15] URL: http://www.helmholtz-berlin.de/media/media/oea/web/pr_webseite/druckschriften/berichte/bessy/annual_report_2008.pdf (visited on 05/23/2012) (cit. on p. 3).
- [16] L. Lammich, C. Domesle, B. Jordon-Thaden, M. Förstel, T. Arion, T. Lischke, O. Heber, S. Klumpp, M. Martins, N. Guerassimova, R. Treusch, J. Ullrich, U. Hergenhahn, H. B. Pedersen, and A. Wolf. “Fragmentation Pathways of $\text{H}^+(\text{H}_2\text{O})_2$ after Extreme Ultraviolet Photoionization”. In: *Phys. Rev. Lett.* 105.25 (2010), p. 253003. DOI: [10.1103/PhysRevLett.105.253003](https://doi.org/10.1103/PhysRevLett.105.253003) (cit. on p. 3).
- [17] M. Mucke, M. Förstel, T. Lischke, T. Arion, A. M. Bradshaw, and U. Hergenhahn. “Performance of a short “magnetic bottle” electron spectrometer”. In: *Rev. Sci. Instrum.* 83.6, 063106 (2012), p. 063106. DOI: [10.1063/1.4729256](https://doi.org/10.1063/1.4729256) (cit. on pp. 3, 40–43).
- [18] A. Wolf, H.-B. Pedersen, L. Lammich, B. Jordon-Thaden, S. Altevogt, C. Domesle, U. Hergenhahn, M. Förstel, and O. Heber. “Soft-x-ray fragmentation studies of molecular ions”. In: *J. Phys. B* 43.19 (2010), p. 194007 (cit. on p. 3).

- [19] T. Arion, M. Mucke, M. Förstel, A. M. Bradshaw, and U. Hergenhahn. “Inter-atomic Coulombic decay in mixed NeKr clusters”. In: *J. Chem. Phys.* 134.7, 074306 (2011), p. 074306. DOI: [10.1063/1.3552082](https://doi.org/10.1063/1.3552082) (cit. on pp. 3, 25).
- [20] R. Püttner, T. Arion, M. Förstel, T. Lischke, M. Mucke, V. Sekushin, G. Kaindl, A. M. Bradshaw, and U. Hergenhahn. “Probing dissociative molecular dications by mapping vibrational wave functions”. In: *Phys. Rev. A* 83 (4 2011), p. 043404. DOI: [10.1103/PhysRevA.83.043404](https://doi.org/10.1103/PhysRevA.83.043404) (cit. on p. 3).
- [21] V. Ulrich, S. Barth, T. Lischke, S. Joshi, T. Arion, M. Mucke, M. Förstel, A. M. Bradshaw, and U. Hergenhahn. “Photoelectron-Auger electron coincidence spectroscopy of free molecules: New experiments”. In: *J. Electron Spectrosc. Relat. Phenom.* 183 (2010), pp. 70 –79. DOI: [DOI:10.1016/j.elspec.2010.03.001](https://doi.org/10.1016/j.elspec.2010.03.001) (cit. on p. 3).
- [22] H. Haberland, L. Bergmann, and C. Schaefer. *Lehrbuch der Experimentalphysik: Lehrbuch der Experimentalphysik 5. Gase, Nanosysteme, Flüssigkeiten*. Ed. by K. Kleinermanns. Gruyter, 2005 (cit. on p. 5).
- [23] L. Bergmann, C., and R. Kassing. *Lehrbuch der Experimentalphysik 5: Gase, Nanosysteme, Flüssigkeiten. 2. Auflage*. Ed. by L. Bergmann and R. Kassing. 2nd ed. Walter de Gruyter, 2005 (cit. on p. 6).
- [24] D. Funk. “The Spectroscopy and Theoretical Aspects of Metal/Rare-Gas van der Waals Molecules”. PhD thesis. University of Utah, 1989 (cit. on p. 6).
- [25] S. Barth. “Untersuchung des ICD-Prozesses in schwach gebundenen Systemen”. PhD thesis. TU Berlin, 2007 (cit. on p. 6).
- [26] D. R. Miller. “Free Jet Sources”. In: *Atomic and Molecular Beam Methods* 1 (1988), 17ff (cit. on p. 6).
- [27] J. H. Moore, C. C. Davis, and M. A. Coplan. *Building Scientific Apparatus*. Addison-Wesley Publishing Company, 1983 (cit. on p. 7).
- [28] R. von Pietrowski, K. von Haeften, T. Laarmann, T. Möller, L. Museur, and A. V. Kanaev. “Electronic and geometric structure of doped rare-gas clusters: surface, site and size effects studied with luminescence spectroscopy”. In: *Eur. Phys. J. D* 38.2 (2006), pp. 323 –336 (cit. on pp. 8, 9, 12).
- [29] H. Vach. “Solvation effects in large binary van der Waals clusters with high doping rates”. In: *J. Chem. Phys.* 113.3 (2000), pp. 1097 –1103. DOI: [10.1063/1.481888](https://doi.org/10.1063/1.481888) (cit. on pp. 8, 12, 69).

- [30] A. Lindblad, H. Bergersen, T. Rander, M. Lundwall, G. Öhrwall, M. Tchapyguine, S. Svensson, and O. Björneholm. “The far from equilibrium structure of argon clusters doped with krypton or xenon”. In: *Phys. Chem. Chem. Phys.* 8.16 (2006), pp. 1899–1905. DOI: [10.1039/B517083D](https://doi.org/10.1039/B517083D) (cit. on pp. 8, 14).
- [31] T. Laarmann, K. von Haeften, H. Wabnitz, and T. Möller. “Electronic energy dissipation processes in doped rare gas clusters with a shell-like structure”. In: *Surf. Rev. Lett.* 9 (2009), pp. 111–116 (cit. on p. 8).
- [32] H. Vach. “Impurity dynamics in binary van der Waals clusters created by pick-up”. In: *J. Chem. Phys.* 111.8 (1999), pp. 3536–3547. DOI: [10.1063/1.479636](https://doi.org/10.1063/1.479636) (cit. on pp. 8, 12).
- [33] M. Lundwall, A. Lindblad, H. Bergersen, T. Rander, G. Öhrwall, M. Tchapyguine, S. Svensson, and O. Björneholm. “Preferential site occupancy of krypton atoms on free argon-cluster surfaces”. In: *J. Chem. Phys.* 125.1, 014305 (2006), p. 014305. DOI: [10.1063/1.2209677](https://doi.org/10.1063/1.2209677) (cit. on p. 8).
- [34] A. Vostrikov and D. Dubov. “Clustering in molecular gases freely expanding into vacuum”. In: *J. Exp. Theor. Phys.* 98.2 (2004). DOI: [10.1134/1.1675887](https://doi.org/10.1134/1.1675887), pp. 197–206 (cit. on p. 8).
- [35] M. Lundwall. “Rare-gas Clusters Studied by Electron Spectroscopy”. PhD thesis. Uppsala Universitet, 2007 (cit. on pp. 8, 10).
- [36] C.-R. Wang, R.-B. Huang, Z.-Y. Liu, and L.-S. Zheng. “Lognormal size distributions of elemental clusters”. In: *Chem. Phys. Lett.* 227.1 (1994), pp. 103–108. DOI: [10.1016/0009-2614\(94\)00790-X](https://doi.org/10.1016/0009-2614(94)00790-X) (cit. on p. 8).
- [37] R. Karnbach, M. Joppien, J. Stapelfeldt, J. Wormer, and T. Moller. “CLULU: An experimental setup for luminescence measurements on van der Waals clusters with synchrotron radiation”. In: *Rev. Sci. Instrum.* 64.10 (1993), pp. 2838–2849. DOI: [10.1063/1.1144371](https://doi.org/10.1063/1.1144371) (cit. on pp. 8, 9).
- [38] U. Buck and R. Krohne. “Cluster size determination from diffractive He atom scattering”. In: *J. Chem. Phys.* 105.13 (1996), pp. 5408–5415. DOI: [10.1063/1.472406](https://doi.org/10.1063/1.472406) (cit. on pp. 8, 9).
- [39] O. F. Hagen. “Cluster ion sources”. In: *Rev. Sci. Instrum.* 63.4 (1992), pp. 2374–2379. DOI: [10.1063/1.1142933](https://doi.org/10.1063/1.1142933) (cit. on p. 8).
- [40] O. F. Hagen. “Nucleation and growth of clusters in expanding nozzle flows”. In: *Surf. Sci.* 106.1 (1981), pp. 101–116. DOI: [10.1016/0039-6028\(81\)90187-4](https://doi.org/10.1016/0039-6028(81)90187-4) (cit. on pp. 8, 9).
- [41] O. F. Hagen. “Condensation in free jets: Comparison of rare gases and metals”. In: *Z. Phys. D* 4.3 (1987), pp. 291–299 (cit. on pp. 8, 9).

- [42] F. London. “Zur Theorie und Systematik der Molekularkräfte”. In: *Z. Phys. A* 63.3 (1930). 10.1007/BF01421741, pp. 245 –279 (cit. on p. 10).
- [43] J. E. Lennard-Jones. “On the Determination of Molecular Fields. - II. From Equation of State of a Gas”. In: *Proc. R. Soc. Lond. A* 106 (1924), pp. 463 –477 (cit. on p. 10).
- [44] J. E. Lennard-Jones. “Cohesion”. In: *Proc. Phys. Soc.* 43 (1931), pp. 461 –482. DOI: [doi:10.1088/0959-5309/43/5/301](https://doi.org/10.1088/0959-5309/43/5/301) (cit. on pp. 10, 11).
- [45] C. Kittel. *Introduction to Solid State Physics, seventh ed.* Wiley, New York, 1996 (cit. on p. 10).
- [46] J. Farges, M. F. de Feraudy, B. Raoult, and G. Torchet. “Noncrystalline structure of argon clusters. I. Polyicosahedral structure of Ar_N clusters, $20 < N < 50$ ”. In: *J. Chem. Phys.* 78.8 (1983), pp. 5067 –5080. DOI: [10.1063/1.445375](https://doi.org/10.1063/1.445375) (cit. on pp. 11, 21).
- [47] J. Farges, M. F. de Feraudy, B. Raoult, and G. Torchet. “Noncrystalline structure of argon clusters. II. Multilayer icosahedral structure of Ar_N clusters, $50 < N < 750$ ”. In: *J. Chem. Phys.* 84.6 (1986), pp. 3491 –3501. DOI: [10.1063/1.450235](https://doi.org/10.1063/1.450235) (cit. on pp. 11, 21).
- [48] T. Ikeshoji, G. Torchet, M.-F. de Feraudy, and K. Koga. “Icosahedron-fcc transition size by molecular dynamics simulation of Lennard-Jones clusters at a finite temperature”. In: *Phys. Rev. E* 63.3 (2001), p. 031101. DOI: [10.1103/PhysRevE.63.031101](https://doi.org/10.1103/PhysRevE.63.031101) (cit. on p. 11).
- [49] S. Kakar, O. Björneholm, J. Weigelt, A. R. B. de Castro, L. Tröger, R. Frahm, T. Möller, A. Knop, and E. Rühl. “Size-dependent K-edge EXAFS study of the structure of free Ar clusters”. In: *Phys. Rev. Lett.* 78.9 (1997), pp. 1675 –1678. DOI: [10.1103/PhysRevLett.78.1675](https://doi.org/10.1103/PhysRevLett.78.1675) (cit. on pp. 11, 21).
- [50] H. Haberland, T. Hippler, J. Donges, O. Kostko, M. Schmidt, and B. von Issendorff. “Melting of Sodium Clusters: Where Do the Magic Numbers Come from?” In: *Phys. Rev. Lett.* 94 (3 2005), p. 035701. DOI: [10.1103/PhysRevLett.94.035701](https://doi.org/10.1103/PhysRevLett.94.035701) (cit. on p. 12).
- [51] A. S. Clarke, R. Kapral, and G. N. Patey. “Structure of two-component clusters”. In: *J. Chem. Phys.* 101.3 (1994), pp. 2432 –2445. DOI: [10.1063/1.467683](https://doi.org/10.1063/1.467683) (cit. on pp. 12, 13).
- [52] A. Lindblad, T. Rander, I. Bradeanu, G. Öhrwall, O. Björneholm, M. Mucke, V. Ulrich, T. Lischke, and U. Hergenhausen. “Chemical shifts of small heterogeneous Ar Xe clusters”. In: *Phys. Rev. B* 83 (2011), p. 125414. DOI: [10.1103/PhysRevB.83.125414](https://doi.org/10.1103/PhysRevB.83.125414) (cit. on pp. 12–14, 18).

- [53] M. Tchapyguine, M. Lundwall, M. Gisselbrecht, G. Öhrwall, R. Feifel, S. Sorensen, S. Svensson, N. Maartensson, and O. Björneholm. “Variable surface composition and radial interface formation in self-assembled free, mixed ArXe clusters”. In: *Phys. Rev. A* 69 (3 2004), p. 031201. DOI: [10.1103/PhysRevA.69.031201](https://doi.org/10.1103/PhysRevA.69.031201) (cit. on pp. 12–14, 85).
- [54] M. Lundwall, M. Tchapyguine, G. Öhrwall, R. Feifel, A. Lindblad, A. Lindgren, S. Sörensen, S. Svensson, and O. Björneholm. “Radial surface segregation in free heterogeneous argon/krypton clusters”. In: *Chem. Phys. Lett.* 392.4 (2004), pp. 433–438. DOI: [10.1016/j.cplett.2004.05.111](https://doi.org/10.1016/j.cplett.2004.05.111) (cit. on pp. 12–14, 69, 72, 81, 95).
- [55] M. Lundwall, H. Bergersen, A. Lindblad, G. Öhrwall, M. Tchapyguine, S. Svensson, and O. Björneholm. “Preferential site occupancy observed in co-expanded argon-krypton clusters”. In: *Phys. Rev. A* 74.4 (2006), p. 043206. DOI: [10.1103/PhysRevA.74.043206](https://doi.org/10.1103/PhysRevA.74.043206) (cit. on pp. 12–14, 69, 72, 95).
- [56] K. T. Tang and J. P. Toennies. “The van der Waals potentials between all the rare gas atoms from He to Rn”. In: *J. Chem. Phys.* 118.11 (2003), pp. 4976–4983. DOI: [10.1063/1.1543944](https://doi.org/10.1063/1.1543944) (cit. on pp. 12, 24).
- [57] M. Lengen, M. Joppien, R. von Pietrowski, and T. Möller. “Assignment of impurity states in xenon-doped argon clusters: Perturbed atomic Rydberg states versus impurity Wannier excitons and the implications for doped rare gas solids”. In: *Chem. Phys. Lett.* 229.4 (1994), pp. 362–369. DOI: [10.1016/0009-2614\(94\)01072-2](https://doi.org/10.1016/0009-2614(94)01072-2) (cit. on pp. 13, 14, 85).
- [58] H. Hertz. “Ueber einen Einfluss des ultravioletten Lichtes auf die electrische Entladung”. In: *Ann. Physik* 267.8 (1887), pp. 983–1000. DOI: [10.1002/andp.18872670827](https://doi.org/10.1002/andp.18872670827) (cit. on p. 14).
- [59] P. Lenard. “Ueber die lichtelektrische Wirkung”. In: *Ann. Physik* 313.5 (1902), pp. 149–198. DOI: [10.1002/andp.19023130510](https://doi.org/10.1002/andp.19023130510) (cit. on p. 14).
- [60] A. Einstein. “Über einen die Erzeugung und Verwandlung des Lichtes betreffenden heuristischen Gesichtspunkt”. In: *Ann. Physik* 322.6 (1905), pp. 132–148. DOI: [10.1002/andp.19053220607](https://doi.org/10.1002/andp.19053220607) (cit. on p. 14).
- [61] T. Koopmans. “Über die Zuordnung von Wellenfunktionen und Eigenwerten zu den Einzelnen Elektronen Eines Atoms”. In: *Physica* 1.1 (1934), pp. 104–113. DOI: [10.1016/S0031-8914\(34\)90011-2](https://doi.org/10.1016/S0031-8914(34)90011-2) (cit. on p. 14).
- [62] E. Fermi. *Nuclear Physics*. Univ. of Chicago Press, 1950, p. 142 (cit. on p. 14).
- [63] V. Schmidt. *Electron Spectrometry of Atoms using Synchrotron Radiation*. Cambridge University Press, 1997 (cit. on p. 15).

- [64] J. W. Cooper. “Photoionization from Outer Atomic Subshells. A Model Study”. In: *Phys. Rev.* 128 (2 1962), pp. 681 –693. DOI: [10.1103/PhysRev.128.681](https://doi.org/10.1103/PhysRev.128.681) (cit. on p. 15).
- [65] K. Maier. “Ein- und Mehrelektroneneffekte bei der O 1s Photoionisation an kleinen Molekülen”. PhD thesis. Technische Universität Berlin, 1999 (cit. on p. 16).
- [66] R. Wehlitz, F. Heiser, O. Hemmers, B. Langer, A. Menzel, and U. Becker. “Electron-energy and -angular distributions in the double photoionization of helium”. In: *Phys. Rev. Lett.* 67 (27 1991), pp. 3764 –3767. DOI: [10.1103/PhysRevLett.67.3764](https://doi.org/10.1103/PhysRevLett.67.3764) (cit. on p. 17).
- [67] T. A. Carlson. “Double Electron Ejection Resulting from Photo-Ionisation in the Outermost Shell of He, Ne, and Ar, and Its Relationship to Electron Correlation”. In: *Phys. Rev.* 156.1 (1967), pp. 142 –149 (cit. on p. 17).
- [68] O. Björneholm, F. Federmann, F. Fössing, T. Möller, and P. Stampfli. “Core level binding energy shifts and polarization screening: A combined experimental and theoretical study of argon clusters”. In: *J. Chem. Phys.* 104.5 (1996), pp. 1846 –1854. DOI: [10.1063/1.470981](https://doi.org/10.1063/1.470981) (cit. on p. 17).
- [69] N. Schwentner, F.-J. Himpsel, V. Saile, M. Skibowski, W. Steinmann, and E. E. Koch. “Photoemission from Rare-Gas Solids: Electron Energy Distributions from the Valence Bands”. In: *Phys. Rev. Lett.* 34 (9 1975), pp. 528 –531. DOI: [10.1103/PhysRevLett.34.528](https://doi.org/10.1103/PhysRevLett.34.528) (cit. on pp. 18–20, 53–56, 60, 61, 96).
- [70] U. Hergenhahn, S. Barth, V. Ulrich, M. Mucke, S. Joshi, T. Lischke, A. Lindblad, T. Rander, G. Öhrwall, and O. Björneholm. “3p valence photoelectron spectrum of Ar clusters”. In: *Phys. Rev. B* 79.15 (2009), p. 155448. DOI: [10.1103/PhysRevB.79.155448](https://doi.org/10.1103/PhysRevB.79.155448) (cit. on pp. 18, 54).
- [71] F. Carnovale, J. B. Peel, R. G. Rothwell, J. Valldorf, and P. J. Kuntz. “Photoelectron spectroscopy of argon clusters: Evidence for an Ar₁₃ ionization chromophore”. In: *J. Chem. Phys.* 90.3 (1989), pp. 1452 –1459. DOI: [10.1063/1.456087](https://doi.org/10.1063/1.456087) (cit. on p. 19).
- [72] D. M. P. Holland, K. Codling, G. V. Marr, and J. B. West. “Multiple photoionisation in the rare gases from threshold to 280 eV”. In: *J. Phys. B* 12.15 (1979), p. 2465 (cit. on pp. 19, 20).
- [73] D. Rolles, H. Zhang, Z. D. Pesic, R. C. Bilodeau, A. Wills, E. Kukk, B. S. Rude, G. D. Ackerman, J. D. Bozek, R. Diez Muino, F. J. Garcia de Abajo, and N. Berrah. “Size effects in angle-resolved photoelectron spectroscopy of free rare-gas clusters”.

- In: *Phys. Rev. A* 75 (3 2007), p. 031201. DOI: [10.1103/PhysRevA.75.031201](https://doi.org/10.1103/PhysRevA.75.031201) (cit. on pp. 19, 54).
- [74] U. Hergenhahn, A. Kolmakov, M. Riedler, A. R. B. de Castro, O. Löfken, and T. Möller. “Observation of excitonic satellites in the photoelectron spectra of Ne and Ar clusters”. In: *Chem. Phys. Lett.* 351 (2002), pp. 235 –241. DOI: [10.1016/S0009-2614\(01\)01394-X](https://doi.org/10.1016/S0009-2614(01)01394-X) (cit. on p. 20).
- [75] J. Stapelfeldt, J. Wörmer, and T. Möller. “Evolution of Electronic Energy Levels in Krypton Clusters from the Atom to the Solid”. In: *Phys. Rev. Lett.* 62 (1 1989), pp. 98 –101. DOI: [10.1103/PhysRevLett.62.98](https://doi.org/10.1103/PhysRevLett.62.98) (cit. on p. 20).
- [76] N. Schwentner. “Mean-free path of electrons in rare-gas solids derived from vacuum-uv photoemission data”. In: *Phys. Rev. B* 14 (12 1976), pp. 5490 –5497. DOI: [10.1103/PhysRevB.14.5490](https://doi.org/10.1103/PhysRevB.14.5490) (cit. on pp. 20, 64).
- [77] M. Tchapyguine, R. R. Marinho, M. Gisselbrecht, J. Schulz, N. Martensson, S. L. Sorensen, A. Naves de Brito, R. Feifel, G. Öhrwall, M. Lundwall, S. Svensson, and O. Björneholm. “The size of neutral free clusters as manifested in the relative bulk-to-surface intensity in core level photoelectron spectroscopy”. In: *J. Chem. Phys.* 120.1 (2004), pp. 345 –356. DOI: [10.1063/1.1630027](https://doi.org/10.1063/1.1630027) (cit. on p. 20).
- [78] H. W. Biester, M. J. Besnard, G. Dujardin, L. Hellner, and E. E. Koch. “Photoemission of pairs of electrons from rare-gas solids”. In: *Phys. Rev. Lett.* 59 (12 1987), pp. 1277–1280. DOI: [10.1103/PhysRevLett.59.1277](https://doi.org/10.1103/PhysRevLett.59.1277) (cit. on p. 20).
- [79] URL: <http://www.chemglobe.org/ptoe/> (visited on 02/24/2012) (cit. on pp. 20, 51).
- [80] R. Santra, J. Zobeley, L. S. Cederbaum, and N. Moiseyev. “Interatomic Coulombic Decay in van der Waals Clusters and Impact of Nuclear Motion”. In: *Phys. Rev. Lett.* 85 (21 2000), pp. 4490 –4493. DOI: [10.1103/PhysRevLett.85.4490](https://doi.org/10.1103/PhysRevLett.85.4490) (cit. on p. 20).
- [81] I. Velchev, W. Hogervorst, and W. Ubachs. “Precision VUV spectroscopy of Ar I at 105 nm”. In: *J. Phys. B* 32.17 (1999), p. L511 (cit. on p. 20).
- [82] P. Lablanquie, T. Aoto, Y. Hikosaka, Y. Morioka, F. Penent, and K. Ito. “Appearance of interatomic Coulombic decay in Ar, Kr, and Xe homonuclear dimers”. In: *J. Chem. Phys.* 127.15 (2007), p. 154323. DOI: [10.1063/1.2778430](https://doi.org/10.1063/1.2778430) (cit. on pp. 20, 25, 80).
- [83] P. Lablanquie and P. Morin. “Double ionization following the 3d 5/2 to 5p excitation in Kr”. In: *J. Phys. B* 24.20 (1991), p. 4349 (cit. on p. 20).

- [84] R. B. Cairns, H. Harrison, and R. I. Schoen. “Multiple Photo-Ionization of Xenon”. In: *Phys. Rev.* 183 (1 1969), pp. 52–56. DOI: [10.1103/PhysRev.183.52](https://doi.org/10.1103/PhysRev.183.52) (cit. on p. 20).
- [85] B. W. van de Waal, G. Torchet, and M.-F. de Feraudy. “Structure of large argon clusters Ar_N , $10^3 < N < 10^5$: experiments and simulations”. In: *Chem. Phys. Lett.* 331.1 (2000), pp. 57–63. DOI: [10.1016/S0009-2614\(00\)01050-2](https://doi.org/10.1016/S0009-2614(00)01050-2) (cit. on p. 21).
- [86] D. A. Young. *Phase Diagrams of the Elements*. University of California Press, Berkeley, CA (USA), 1991 (cit. on p. 21).
- [87] W. Demtröder. *Experimentalphysik 3, Atome, Moleküle und Festkörper*. 2nd. Springer-Verlag Berlin Heidelberg New York, 2000 (cit. on pp. 21, 22).
- [88] H. Ibach and H. Lüth. *Festkörperphysik*. Springer-Verlag Berlin Heidelberg New York, 1981 (cit. on p. 22).
- [89] S. Hüfner. *Photoelectron Spectroscopy: Principles and Applications*. Springer series in solid-state sciences. Springer, 2003 (cit. on p. 22).
- [90] Ph. Hofmann, Ch. Sondergaard, S. Agergaard, S. V. Hoffmann, J. E. Gayone, G. Zampieri, S. Lizzit, and A. Baraldi. “Unexpected surface sensitivity at high energies in angle-resolved photoemission”. In: *Phys. Rev. B* 66 (24 2002), p. 245422. DOI: [10.1103/PhysRevB.66.245422](https://doi.org/10.1103/PhysRevB.66.245422) (cit. on p. 22).
- [91] R. Santra and L. S. Cederbaum. “Non-Hermitian electronic theory and applications to clusters”. In: *Phys. Rep.* 368.1 (2002), pp. 1–117. DOI: [10.1016/S0370-1573\(02\)00143-6](https://doi.org/10.1016/S0370-1573(02)00143-6) (cit. on p. 24).
- [92] R. Santra, J. Zobeley, and L. S. Cederbaum. “Electronic decay of valence holes in clusters and condensed matter”. In: *Phys. Rev. B* 64 (24 2001), p. 245104. DOI: [10.1103/PhysRevB.64.245104](https://doi.org/10.1103/PhysRevB.64.245104) (cit. on pp. 24, 26).
- [93] V. Averbukh, I. B. Müller, and L. S. Cederbaum. “Mechanism of Interatomic Coulombic Decay in Clusters”. In: *Phys. Rev. Lett.* 93 (26 2004), p. 263002. DOI: [10.1103/PhysRevLett.93.263002](https://doi.org/10.1103/PhysRevLett.93.263002) (cit. on pp. 24, 25).
- [94] V. Averbukh and L. S. Cederbaum. “Interatomic (Intermolecular) Decay Processes in Clusters: Current Status and Outlook”. In: *AIP Conference Proceedings* 963.1 (2007). Ed. by George Maroulis and Theodore E. Simos, pp. 39–46. DOI: [10.1063/1.2827022](https://doi.org/10.1063/1.2827022) (cit. on p. 24).

- [95] T. Jahnke, A. Czasch, M. Schöffler, S. Schössler, M. Kász, J. Titze, K. Kreidi, R. E. Grisenti, A. Staudte, O. Jagutzki, L. H. Schmidt, Th. Weber, H. Schmidt-Böcking, K. Ueda, and R. Dörner. “Experimental Separation of Virtual Photon Exchange and Electron Transfer in Interatomic Coulombic Decay of Neon Dimers”. In: *Phys. Rev. Lett.* 99 (15 2007), p. 153401. DOI: [10.1103/PhysRevLett.99.153401](https://doi.org/10.1103/PhysRevLett.99.153401) (cit. on pp. 24–26, 29).
- [96] A. Bondi. “van der Waals Volumes and Radii”. In: *J. Phys. Chem.* 68.3 (1964), pp. 441–451. DOI: [10.1021/j100785a001](https://doi.org/10.1021/j100785a001). eprint: <http://pubs.acs.org/doi/pdf/10.1021/j100785a001> (cit. on p. 24).
- [97] T. D. Thomas, C. Miron, K. Wiesner, P. Morin, T. X. Carroll, and L. J. Saethre. “Anomalous Natural Linewidth in the $2p$ Photoelectron Spectrum of SiF_4 ”. In: *Phys. Rev. Lett.* 89 (22 2002), p. 223001. DOI: [10.1103/PhysRevLett.89.223001](https://doi.org/10.1103/PhysRevLett.89.223001) (cit. on p. 24).
- [98] J. A. D. Matthew and Y. Komninos. “Transition rates for interatomic Auger processes”. In: *Surf. Sci.* 53.1 (1975), pp. 716–725. DOI: [10.1016/0039-6028\(75\)90166-1](https://doi.org/10.1016/0039-6028(75)90166-1) (cit. on p. 25).
- [99] Th. Förster. “Zwischenmolekulare Energiewanderung und Fluoreszenz”. In: *Ann. Physik* 437.1 (1948), pp. 55–75. DOI: [10.1002/andp.19484370105](https://doi.org/10.1002/andp.19484370105) (cit. on p. 25).
- [100] S. Marburger, O. Kugeler, U. Hergenhahn, and T. Möller. “Experimental Evidence for Interatomic Coulombic Decay in Ne Clusters”. In: *Phys. Rev. Lett.* 90.20 (2003), p. 203401. DOI: [10.1103/PhysRevLett.90.203401](https://doi.org/10.1103/PhysRevLett.90.203401) (cit. on p. 25).
- [101] T. Jahnke, A. Czasch, M. S. Schöffler, S. Schössler, A. Knapp, M. Kász, J. Titze, C. Wimmer, K. Kreidi, R. E. Grisenti, A. Staudte, O. Jagutzki, U. Hergenhahn, H. Schmidt-Böcking, and R. Dörner. “Experimental Observation of Interatomic Coulombic Decay in Neon Dimers”. In: *Phys. Rev. Lett.* 93.16 (2004), p. 163401. DOI: [10.1103/PhysRevLett.93.163401](https://doi.org/10.1103/PhysRevLett.93.163401) (cit. on p. 25).
- [102] T. Jahnke, H. Sann, T. Havermeier, K. Kreidi, C. Stuck, M. Meckel, M. Schöffler, N. Neumann, R. Wallauer, S. Voss, A. Czasch, O. Jagutzki, A. Malakzadeh, F. Afaneh, Th. Weber, H. Schmidt-Böcking, and R. Dörner. “Ultrafast energy transfer between water molecules”. In: *Nature Phys.* 6 (2010), pp. 139–142. DOI: [10.1038/nphys1498](https://doi.org/10.1038/nphys1498) (cit. on p. 25).
- [103] S. Barth, S. Marburger, S. Joshi, V. Ulrich, O. Kugeler, and U. Hergenhahn. “Interface identification by non-local autoionization transitions”. In: *Phys. Chem. Chem. Phys.* 8 (27 2006), pp. 3218–3222. DOI: [10.1039/B602019D](https://doi.org/10.1039/B602019D) (cit. on p. 25).

- [104] T. Havermeier, T. Jahnke, K. Kreidi, R. Wallauer, S. Voss, M. Schöffler, S. Schössler, L. Foucar, N. Neumann, J. Titze, H. Sann, M. Kühnel, J. Voigtsberger, J. H. Morilla, W. Schöllkopf, H. Schmidt-Böcking, R. E. Grisenti, and R. Dörner. “Interatomic Coulombic Decay following Photoionization of the Helium Dimer: Observation of Vibrational Structure”. In: *Phys. Rev. Lett.* 104 (13 2010), p. 133401. DOI: [10.1103/PhysRevLett.104.133401](https://doi.org/10.1103/PhysRevLett.104.133401) (cit. on p. 25).
- [105] Y. Morishita, X.-J. Liu, N. Saito, T. Lischke, M. Kato, G. Prümper, M. Oura, H. Yamaoka, Y. Tamenori, I. H. Suzuki, and K. Ueda. “Experimental Evidence of Interatomic Coulombic Decay from the Auger Final States in Argon Dimers”. In: *Phys. Rev. Lett.* 96 (24 2006), p. 243402. DOI: [10.1103/PhysRevLett.96.243402](https://doi.org/10.1103/PhysRevLett.96.243402) (cit. on p. 25).
- [106] K. Ueda, X. J. Liu, G. Prümper, H. Fukuzawa, Y. Morishita, and N. Saito. “Electron - ion coincidence momentum spectroscopy: Its application to Ar dimer interatomic decay”. In: *J. Electron Spectrosc. Relat. Phenom.* 155.1 (2007), pp. 113 –118. DOI: [10.1016/j.elspec.2006.10.007](https://doi.org/10.1016/j.elspec.2006.10.007) (cit. on p. 25).
- [107] T. Aoto, K. Ito, Y. Hikosaka, E. Shigemasa, F. Penent, and P. Lablanquie. “Properties of Resonant Interatomic Coulombic Decay in Ne Dimers”. In: *Phys. Rev. Lett.* 97 (24 2006), p. 243401. DOI: [10.1103/PhysRevLett.97.243401](https://doi.org/10.1103/PhysRevLett.97.243401) (cit. on p. 25).
- [108] S. Barth, S. Joshi, S. Marburger, V. Ulrich, A. Lindblad, G. Öhrwall, O. Björneholm, and U. Hergenhahn. “Observation of resonant Interatomic Coulombic Decay in Ne clusters”. In: *J. Chem. Phys.* 122.24 (2005), p. 241102. DOI: [10.1063/1.1937395](https://doi.org/10.1063/1.1937395) (cit. on p. 25).
- [109] V. Averbukh and L. S. Cederbaum. “Interatomic Electronic Decay in Endohedral Fullerenes”. In: *Phys. Rev. Lett.* 96 (5 2006), p. 053401. DOI: [10.1103/PhysRevLett.96.053401](https://doi.org/10.1103/PhysRevLett.96.053401) (cit. on p. 25).
- [110] C. Buth, R. Santra, and L. S. Cederbaum. “Impact of interatomic electronic decay processes on Xe 4d hole decay in the xenon fluorides”. In: *J. Chem. Phys.* 119.20 (2003), pp. 10575 –10584. DOI: [10.1063/1.1620502](https://doi.org/10.1063/1.1620502) (cit. on p. 25).
- [111] S. D. Stoychev, A. I. Kuleff, and L. S. Cederbaum. “Intermolecular Coulombic Decay in Small Biochemically Relevant Hydrogen-Bonded Systems”. In: *J. Am. Chem. Soc.* 133.17 (2011), pp. 6817 –6824. DOI: [10.1021/ja200963y](https://doi.org/10.1021/ja200963y). eprint: <http://pubs.acs.org/doi/pdf/10.1021/ja200963y> (cit. on p. 28).
- [112] F. R. Elder, A. M. Gurewitsch, R. V. Langmuir, and H. C. Pollock. “Radiation from Electrons in a Synchrotron”. In: *Phys. Rev.* 71 (1947), pp. 829 –830. DOI: [10.1103/PhysRev.71.829.5](https://doi.org/10.1103/PhysRev.71.829.5) (cit. on p. 31).

- [113] URL: http://en.wikipedia.org/wiki/Synchrotron_radiation (visited on 02/08/2012) (cit. on p. 31).
- [114] H. Winick and S. Doniach. *Synchrotron Radiation Research*. Plenum Press, New York and London, 1982 (cit. on p. 32).
- [115] J. D. Jackson. *Classical Electrodynamics*. 1999 (cit. on p. 33).
- [116] URL: http://www.bessy.de/bit/bit_show_object.html.php?i_bit_id_object=32 (visited on 02/09/2012) (cit. on p. 34).
- [117] URL: http://www.bessy.de/bit/upload/D_15_1A.pdf (visited on 02/09/2012) (cit. on p. 34).
- [118] S. P. Marburger. “Experimentelle Untersuchungen zum Interatomaren Coulomb Zerfall an Neon Clustern: Nachweis eines ultraschnellen nichtlokalen Zerfallskanals”. PhD thesis. TU Berlin, 2004 (cit. on p. 37).
- [119] C. Bostedt, H. N. Chapman, J. T. Costello, J. R. Crespo Lopez-Urrutia, S. Düsterer, S. W. Epp, J. Feldhaus, A. Föhlisch, M. Meyer, T. Möller, R. Moshhammer, M. Richter, K. Sokolowski-Tinten, A. Sorokin, K. Tiedtke, J. Ullrich, and W. Wurth. “Experiments at FLASH”. In: *Nucl. Instr. Meth. Phys. Res. A* 601.1 (2009), pp. 108–122. DOI: [10.1016/j.nima.2008.12.202](https://doi.org/10.1016/j.nima.2008.12.202) (cit. on p. 38).
- [120] P. Kruit and F. H. Read. “Magnetic field paralleliser for 2π electron-spectrometer and electron-image magnifier”. In: *J. Phys. E* 16.4 (1983), p. 313 (cit. on pp. 38, 39, 44).
- [121] T. Tsuboi, E. Y. Xu, Y. K. Bae, and K. T. Gillen. “Magnetic bottle electron spectrometer using permanent magnets”. In: *Rev. Sci. Instrum.* 59.8 (1988), pp. 1357–1362. DOI: [10.1063/1.1139722](https://doi.org/10.1063/1.1139722) (cit. on pp. 38, 39).
- [122] L. J. Wiza. “Microchannel plate detectors”. In: *Nucl. Instrum. Methods* 162 (1979), pp. 587–601. DOI: [10.1016/0029-554X\(79\)90734-1](https://doi.org/10.1016/0029-554X(79)90734-1) (cit. on p. 39).
- [123] G. W. Fraser. “The electron detection efficiency of microchannel plates”. In: *Nucl. Instr. Meth.* 206 (1982), pp. 445–449 (cit. on p. 41).
- [124] D. A. Dahl. “SIMION for the personal computer in reflection”. In: *Int. J. Mass Spectrom.* 200 (2000), pp. 3–25. DOI: [10.1016/S1387-3806\(00\)00305-5](https://doi.org/10.1016/S1387-3806(00)00305-5) (cit. on p. 41).
- [125] URL: <http://en.wikipedia.org/wiki/SIMION> (visited on 02/20/2012) (cit. on p. 41).
- [126] R. Fitzpatrick. *The Physics of Plasmas*. Lulu, 2008 (cit. on p. 44).

- [127] T. X. Carroll, J. D. Bozek, E. Kukk, V. Myrseth, L. J. Saethre, T. D. Thomas, and K. Wiesner. “Xenon N_{4,500} Auger spectrum - a useful calibration source”. In: *J. Electron Spectrosc. Relat. Phenom.* 125.2 (2002), pp. 127–132. DOI: [10.1016/S0368-2048\(02\)00134-2](https://doi.org/10.1016/S0368-2048(02)00134-2) (cit. on p. 51).
- [128] B. Kassühlke. “Elektronische Struktur von Adsorbaten und Kondensaten untersucht mit zweidimensionaler Elektronen-Flugzeitspektroskopie”. PhD thesis. Herbert Utz Verlag - Wissenschaft, 1998 (cit. on pp. 53–56, 96).
- [129] S. Galamic-Mulaomerovic and C. H. Patterson. “Band structures of rare-gas solids within the GW approximation”. In: *Phys. Rev. B* 71 (19 2005), p. 195103. DOI: [10.1103/PhysRevB.71.195103](https://doi.org/10.1103/PhysRevB.71.195103) (cit. on pp. 53, 65).
- [130] M. Förstel, M. Mucke, T. Arion, T. Lischke, S. Barth, V. Ulrich, G. Öhrwall, O. Björneholm, U. Hergenhahn, and A. M. Bradshaw. “Observation of electronic energy bands in argon clusters”. In: *Phys. Rev. B* 82.12 (2010), p. 125450. DOI: [10.1103/PhysRevB.82.125450](https://doi.org/10.1103/PhysRevB.82.125450) (cit. on pp. 53, 54).
- [131] M. Förstel, M. Mucke, T. Arion, T. Lischke, S. Barth, V. Ulrich, G. Öhrwall, O. Björneholm, U. Hergenhahn, and A. M. Bradshaw. “Energy band dispersion in photoemission spectra of argon clusters”. In: *J. Electron Spectrosc. Relat. Phenom.* 184.3-6 (2011). Advances in Vacuum Ultraviolet and X-ray Physics, The 37th International Conference on Vacuum Ultraviolet and X-ray Physics (VUVX2010), pp. 107–112. DOI: [DOI:10.1016/j.elspec.2010.09.001](https://doi.org/10.1016/j.elspec.2010.09.001) (cit. on p. 53).
- [132] R. Feifel, M. Tchapyguine, G. Öhrwall, M. Salonen, M. Lundwall, R. R. T. Marinho, M. Gisselbrecht, S. L. Sorensen, A. Naves de Brito, L. Karlsson, N. Martensson, S. Svensson, and O. Björneholm. “From localised to delocalised electronic states in free Ar, Kr and Xe clusters”. In: *Eur. Phys. J. D* 30 (3 2004), pp. 343–351. DOI: [10.1140/epjd/e2004-00103-6](https://doi.org/10.1140/epjd/e2004-00103-6) (cit. on pp. 54, 64, 71, 84, 85, 87).
- [133] D. Rolles, H. Zhang, Z. D. Pesic, J. D. Bozek, and N. Berrah. “Emergence of valence band structure in rare-gas clusters”. In: *Chem. Phys. Lett.* 468.4 (2009), pp. 148–152. DOI: [10.1016/j.cplett.2008.12.015](https://doi.org/10.1016/j.cplett.2008.12.015) (cit. on pp. 54, 60, 84).
- [134] K. Horn, M. Scheffler, and A. M. Bradshaw. “Photoemission from Physisorbed Xenon: Evidence for Lateral Interactions”. In: *Phys. Rev. Lett.* 41.12 (1978), pp. 822–824 (cit. on p. 54).
- [135] N. C. Bacalis, D. A. Papaconstantopoulos, and W. E. Pickett. “Systematic calculations of the band structures of the rare-gas crystals neon, argon, krypton, and xenon”. In: *Phys. Rev. B* 38 (9 1988), pp. 6218–6226. DOI: [10.1103/PhysRevB.38.6218](https://doi.org/10.1103/PhysRevB.38.6218) (cit. on p. 56).

- [136] P. Feulner. “private communication” (cit. on p. 56).
- [137] B. Kassühlke. “private communication” (cit. on pp. 60, 61).
- [138] K. Rademann, T. Rech, B. Kaiser, U. Even, and F. Hensel. “A new coincidence technique for vacuum ultraviolet photoelectron spectroscopy of neutral clusters in a molecular beam”. In: *Rev. Sci. Instrum.* 62.8 (1991), pp. 1932–1941. DOI: [10.1063/1.1142395](https://doi.org/10.1063/1.1142395) (cit. on p. 65).
- [139] M. Förstel, M. Mucke, T. Arion, A. M. Bradshaw, and U. Hergenhahn. “Autoionization Mediated by Electron Transfer”. In: *Phys. Rev. Lett.* 106.3 (2011), p. 033402. DOI: [10.1103/PhysRevLett.106.033402](https://doi.org/10.1103/PhysRevLett.106.033402) (cit. on pp. 67, 82).
- [140] G. V. Marr and J. B. West. “Absolute Photoionization Cross-Section Tables For Helium, Neon, Argon, and Krypton in the VUV Spectral Regions”. In: *Atomic Data and Nuclear Data Tables* 18 (1976), pp. 497–508 (cit. on p. 69).
- [141] G. M. Lawrence. “The radiative lifetime of the sp^6 2S state of Ar II”. In: *Proc. 20th Conf. on Gaseous Electronics* 56 (1967), p. 1 (cit. on p. 77).
- [142] E. W. Becker, K. Bier, and W. Henkes. “Strahlen aus kondensierten Atomen und Molekeln im Hochvakuum”. In: *Z. Phys. A* 146 (3 1956). DOI: [10.1007/BF01330428](https://doi.org/10.1007/BF01330428), pp. 333–338 (cit. on p. 81).
- [143] K. Sakai, S. Stoychev, T. Ouchi, I. Higuchi, M. Schöffler, T. Mazza, H. Fukuzawa, K. Nagaya, M. Yao, Y. Tamenori, A. I. Kuleff, N. Saito, and K. Ueda. “Electron-Transfer-Mediated Decay and Interatomic Coulombic Decay from the Triply Ionized States in Argon Dimers”. In: *Phys. Rev. Lett.* 106.3 (2011), p. 033401. DOI: [10.1103/PhysRevLett.106.033401](https://doi.org/10.1103/PhysRevLett.106.033401) (cit. on p. 82).
- [144] M. Hoener, D. Rolles, A. Aguilar, R. C. Bilodeau, D. Esteves, P. Olalde Velasco, Z. D. Pesic, E. Red, and N. Berrah. “Site-selective ionization and relaxation dynamics in heterogeneous nanosystems”. In: *Phys. Rev. A* 81 (2 2010), p. 021201. DOI: [10.1103/PhysRevA.81.021201](https://doi.org/10.1103/PhysRevA.81.021201) (cit. on p. 82).
- [145] E. Fasshauer. “to be published” (cit. on p. 83).
- [146] J. A. R. Samson and W. C. Stolte. “Precision measurements of the total photoionization cross-sections of He, Ne, Ar, Kr, and Xe”. In: *J. Electron Spectrosc. Relat. Phenom.* 123.2 (2002), pp. 265–276. DOI: [10.1016/S0368-2048\(02\)00026-9](https://doi.org/10.1016/S0368-2048(02)00026-9) (cit. on p. 85).
- [147] W. R. Johnson and K. T. Cheng. “Photoionization of the outer shells of neon, argon, krypton, and xenon using the relativistic random-phase approximation”. In: *Phys. Rev. A* 20 (3 1979), pp. 978–988. DOI: [10.1103/PhysRevA.20.978](https://doi.org/10.1103/PhysRevA.20.978) (cit. on p. 86).

-
- [148] URL: http://www.dfg.de/en/service/press/press_releases/2012/press_release_no_18/index.html (visited on 05/09/2012) (cit. on p. 96).
- [149] R. Dörner, S. Denifl, A. Dreuw, U. Fröhling, K. Gokhberg, L. Cederbaum, U. Hergenhahn, T. Jahnke, and B. Winter. *Funding Proposal, DFG Research Unit FOR 1789 Intermolecular and Interatomic Coulombic Decay*. 2012 (cit. on p. 96).

Acknowledgments

I would like to thank all those who contributed to the success of this work.

First and foremost my advisor PD Dr. U. Hergenbahn.

Prof. Dr. T. Möller made it possible for me to submit my dissertation at the TU-Berlin.

Discussions with Prof. A. Bradshaw led to significant contributions to the band structure chapter. Prof. Feulner was so kind to provide some of the presented data relevant for discussion.

Discussions with Dr. N. Sisourat, Dr. E. Faßhauer and Prof. L. Cederbaum regarding ICD and ETMD are acknowledged.

My colleagues contributing to instrumentation, discussion and experiments were Dr. T. Lischke, Dr. M. Mucke, Dr. T. Arion, Dr. H.-P. Rust, Dr. B. Jordan-Thaden, Ch. Domesle, Dr. L. Lammich, Prof. H. P. Pedersen, Prof. A. Wolf, Dr. M. Stier, A. Knie, A. Meißner, Dr. M. Braune, Dr. Ch. Günther, Dr. S. Klumpp, Dr. R. Püttner, Dr. V. Ullrich and Dr. S. Barth.

The experiments would not have been possible without the kind support from the staff of BESSY II. Especially the workshop was very helpful.

My wife L. Kuo patiently copy-edited the text.

Financial support is acknowledged from the Advanced Study Group of the Max-Planck-Society, the Deutsche Forschungsgemeinschaft and the Fonds der chemischen Industrie.